INL/EXT-13-29930 Rev. 1

October 2014

BISON Theory Manual
The Equations Behind Nuclear Fuel Analysis
BISON Release 1.1

J. D. Hales
R. L. Williamson
S. R. Novascone
G. Pastore
B. W. Spencer
D. S. Stafford
K. A. Gamble
D. M. Perez
W. Liu

NOTICE

This information was prepared as an account of work sponsored by an agency of the U.S. Government. Neither the U.S. Government nor any agency thereof, nor any of their employees, makes any warranty, express or implied, or assumes any legal liability or responsibility for any third party's use, or the results of such use, of any information, apparatus, product, or process disclosed herein, or represents that its use by such third party would not infringe privately owned rights. The views expressed herein are not necessarily those of the U.S. Nuclear Regulatory Commission.

INL/EXT-13-29930 Rev. 1

BISON Theory Manual
The Equations Behind Nuclear Fuel Analysis

J. D. Hales
R. L. Williamson
S. R. Novascone
G. Pastore
B. W. Spencer
D. S. Stafford
K. A. Gamble
D. M. Perez
W. Liu

October 2014

Idaho National Laboratory
Fuel Modeling and Simulation Department
Idaho Falls, Idaho 83415

Prepared for the
U.S. Department of Energy
Office of Nuclear Energy
Under U.S. Department of Energy-Idaho Operations Office
Contract DE-AC07-99ID13727

BISON Theory Manual

The Equations behind Nuclear Fuel Analysis

[1]J. D. Hales
[1]R. L. Williamson
[1]S. R. Novascone
[1]G. Pastore
[1]B. W. Spencer
[1]D. S. Stafford
[1]K. A. Gamble
[1]D. M. Perez
[2]W. Liu

[1]Idaho National Laboratory
[2]ANATECH, Inc.

Fuels Modeling & Simulation Department
Idaho National Laboratory
P.O. Box 1625
Idaho Falls, ID 83415-3840

October 2014

Contents

1 Introduction **5**

2 Governing Equations **6**

3 Element Kinematics **7**

4 Axisymmetric Equations **8**

5 Spherically Symmetric Equations **9**

6 Elasticity **10**

7 Nonlinear Materials **11**

8 Material and Behavioral Models **13**

8.1 FeCrAl 13
  8.1.1 Thermal Properties - Kanthal APMT alloy `[ThermalKanthal]` 13
  8.1.2 Mechanical Properties - Kanthal APMT alloy `[MechKanthal]` 13
8.2 HT9 Martensitic Steel 14
  8.2.1 Thermal Properties `[ThermalHT9]` 14
  8.2.2 Mechanical Properties `[MechHT9]` 14
  8.2.3 Thermal and Irradiation Creep `[ThermalIrradiationCreepHT9]` . . . 14
8.3 Molybdenum 15
  8.3.1 Thermal Properties `[ThermalMo]` 15
  8.3.2 Mechanical Properties `[MechMo]` 15
8.4 Nickel-base Alloy PK33 16
  8.4.1 Thermal Properties `[ThermalAlloy33]` 16
  8.4.2 Mechanical Properties `[MechAlloy33]` 16
8.5 Pyrolitic Carbon 16
  8.5.1 Irradiation-induced Strain `[PyCIrradiationStrain]` 16
  8.5.2 Irradiation Creep `[CreepPyC]` 17
8.6 Silicon Carbide 17
  8.6.1 Irradiation Creep `[CreepSiC]` 17
8.7 Stainless Steel 316 17
  8.7.1 Thermal Properties `[Thermal316]` 17
  8.7.2 Mechanical Properties `[MechSS316]` 18

8.8 UO_2 and MOX 18
  8.8.1 Thermal Properties - UO_2 `[ThermalFuel]` 18
  8.8.2 Thermal Properties - MOX `[ThermalFuel]` 24
  8.8.3 Densification `[VSwellingUO2]` 27
  8.8.4 Fission Product Swelling `[VSwellingUO2]` 28
  8.8.5 Relocation `[RelocationUO2]` 28
  8.8.6 Thermal and Irradiation Creep - UO_2 `[CreepUO2]` 30
  8.8.7 Stress-induced Densification - UO_2 `[HotPressingUO2]` 31
  8.8.8 Thermal and Irradiation Creep - MOX `[CreepMOX]` 34
  8.8.9 Smeared Cracking 36
  8.8.10 Grain Growth 37
8.9 Uranium Metal 38
  8.9.1 Thermal Properties `[ThermalU]` 38
8.10 U-10Mo 38
  8.10.1 Thermal Properties `[ThermalU10Mo]` 38
8.11 U_3Si_2 38
  8.11.1 Thermal Properties `[ThermalU3Si2]` 38
  8.11.2 Volumetric Swelling `[VSwellingU3Si2]` 39
8.12 Zircaloy 39
  8.12.1 Irradiation Creep `[ThermalIrradiationCreepZr4]` 39
  8.12.2 Thermal Creep 40
  8.12.3 Combined Creep and Instantaneous Plasticity `[ThermalIrradiationCreepPlasZr4]` `[MechZryModel]` 42
  8.12.4 Irradiation Growth `[IrradiationGrowthZr4]` 42
  8.12.5 Damage `[CumulativeDamageIndex]` 42
  8.12.6 Phase transformation `[ZrPhase]` 43
  8.12.7 Hydride formation `[HydridePrecipitationRate]` 44

9 General Material Models **47**
9.1 Thermal Conductivity Porosity Model 47
9.2 Mass Diffusion Coefficients `[ArrheniusMaterialProperty]` `[ArrheniusDiffusionCoef]` 47

10 Fission Gas Behavior **48**
10.1 Simple Physics-Based Model `[Sifgrs]` 48
  10.1.1 Intra-granular gas behavior 48
  10.1.2 Grain-face gas behavior 49
  10.1.3 Transient gas behavior 51
  10.1.4 Athermal gas release 54
  10.1.5 Grain growth and grain boundary sweeping 54
10.2 Modified Forsberg-Massih Model `[ForMas]` 55

11 Power, Burnup, and Related Models **58**
11.1 Power 58
  11.1.1 Radial Power Profile 58

11.2 Decay Heat 60
11.3 Burnup Calculation 62
11.4 Fission Rate 62
11.5 Fast Neutron Flux 62
11.6 Fast Neutron Fluence 63

12 Evolving Density 64

13 Gap/Plenum Models 65
13.1 Gap Heat Transfer 65
13.2 Mechanical Contact 67
13.3 Gap/plenum pressure 67
13.4 Gap/plenum temperature 67

14 Coolant Channel Model 69
14.1 Coolant Enthalpy Model 69
14.2 Pre-CHF Heat Transfer Correlations 70
14.3 Critical Heat Flux Correlations 72
14.4 Post-CHF Heat Transfer Correlation 74
  14.4.1 Transition Boiling 75
  14.4.2 Film Boiling 76
14.5 Logic to Determine Heat Transfer Regime 78
14.6 FLECHT Reflood Heat Transfer Correlation 79
  14.6.1 Period of Radiation Only 80
  14.6.2 Period I 81
  14.6.3 Period II 82
  14.6.4 Period III 83
  14.6.5 Modification for Low Flooding Rates 84
14.7 Properties for Water and Steam 84

15 Cladding Corrosion Model 86
15.1 Zirconium Alloy at Normal Operating Temperatures 86
  15.1.1 Introduction 86
  15.1.2 EPRI SLI Model 88
  15.1.3 Zirconium Oxide Thermal Conductivity 90
  15.1.4 Numerical Method 90
15.2 Zirconium Alloy at High Temperature 91
15.3 Aluminum 93

Bibliography 94

1 Introduction

BISON [1] is a finite element-based nuclear fuel performance code applicable to a variety of fuel forms including light water reactor fuel rods, TRISO particle fuel [2], and metallic rod [3] and plate fuel. It solves the fully-coupled equations of thermomechanics and species diffusion, for either 1D spherical, 2D axisymmetric or 3D geometries. Fuel models are included to describe temperature and burnup dependent thermal properties, fission product swelling, densification, thermal and irradiation creep, fracture, and fission gas production and release. Plasticity, irradiation growth, and thermal and irradiation creep models are implemented for clad materials. Models are also available to simulate gap heat transfer, mechanical contact, and the evolution of the gap/plenum pressure with plenum volume, gas temperature, and fission gas addition. BISON is based on the MOOSE framework [4] and can therefore efficiently solve problems using standard workstations or very large high-performance computers.

This document describes the theoretical and numerical foundations of BISON.

2 Governing Equations

The BISON governing relations consist of fully-coupled partial differential equations for energy, species, and momentum conservation. The energy balance is given in terms of the heat conduction equation

$$\rho C_p \frac{\partial T}{\partial t} + \nabla \cdot \mathbf{q} - e_f \dot{F} = 0, \tag{2.1}$$

where T, ρ and C_p are the temperature, density and specific heat, respectively, e_f is the energy released in a single fission event, and $\dot{F}$ is the volumetric fission rate. $\dot{F}$ can be prescribed as a function of time and space, or input from a separate neutronics calculation. The heat flux is given as

$$\mathbf{q} = -k \nabla T, \tag{2.2}$$

where k denotes the thermal conductivity of the material.

Species conservation is given by

$$\frac{\partial C}{\partial t} + \nabla \cdot \mathbf{J} + \lambda C - S = 0, \tag{2.3}$$

where C, λ, and S are the concentration, radioactive decay constant, and source rate of a given species, respectively. The mass flux $\mathbf{J}$ is specified as

$$\mathbf{J} = -D \nabla C, \tag{2.4}$$

where D is the diffusion coefficient; this definition has been used to simulate fission product transport within the fuel. Also implemented in BISON is a hyperstoichiometric model for oxygen diffusion in UO_2 fuel as described in [5]. In this case $\mathbf{J}$ denotes the oxygen flux in the hyperstoichiometric regime with,

$$\mathbf{J} = -D \left(\nabla C - \frac{C Q^*}{F R T^2} \nabla T \right), \tag{2.5}$$

where D is diffusivity, F is the thermodynamic factor of oxygen, Q^* is the heat of transport of oxygen, and R is the universal gas constant.

Momentum conservation is prescribed assuming static equilibrium at each time increment using Cauchy's equation,

$$\nabla \cdot \sigma + \rho \mathbf{f} = 0, \tag{2.6}$$

where σ is the Cauchy stress tensor and $\mathbf{f}$ is the body force per unit mass (e.g. gravity). The displacement field u, which is the primary solution variable, is connected to the stress field via the strain, through a constitutive relation.

3 Element Kinematics

For geometrically linear analysis, the strain ε is defined as $1/2[\nabla \mathbf{u} + \nabla \mathbf{u}^T]$. Furthermore, with a linear elastic constitutive model, the stress is simply $C\,\varepsilon$. We now outline our approach for nonlinear analysis. We follow the approach in [6] and the software package [7].

We begin with a complete set of data for step n and seek the displacements and stresses at step $n+1$. We first compute an incremental deformation gradient,

$$\hat{\mathbf{F}} = \frac{\partial x^{n+1}}{\partial x^n}. \tag{3.1}$$

With $\hat{\mathbf{F}}$, we next compute a strain increment that represents the rotation-free deformation from the configuration at n to the configuration at $n+1$. Following [6], we seek the stretching rate $\mathbf{D}$:

$$\begin{aligned} \mathbf{D} =& \frac{1}{\Delta t}\log(\hat{\mathbf{U}}) && (3.2) \\ =& \frac{1}{\Delta t}\log\left(\mathrm{sqrt}\left(\hat{\mathbf{F}}^T\hat{\mathbf{F}}\right)\right) && (3.3) \\ =& \frac{1}{\Delta t}\log\left(\mathrm{sqrt}\left(\hat{\mathbf{C}}\right)\right). && (3.4) \end{aligned}$$

Here, $\hat{\mathbf{U}}$ is the incremental stretch tensor, and $\hat{\mathbf{C}}$ is the incremental Green deformation tensor. Through a Taylor series expansion, this can be determined in a straightforward, efficient manner. $\mathbf{D}$ is passed to the constitutive model as an input for computing σ at $n+1$.

The next step is computing the incremental rotation, $\hat{\mathbf{R}}$ where $\hat{\mathbf{F}} = \hat{\mathbf{R}}\hat{\mathbf{U}}$. Like for $\mathbf{D}$, an efficient algorithm exists for computing $\hat{\mathbf{R}}$. It is also possible to compute these quantities using an eigenvalue/eigenvector routine.

With σ and $\hat{\mathbf{R}}$, we rotate the stress to the current configuration.

4 Axisymmetric Equations

For the axisymmetric case (RZ), the nonlinear strains are derived starting from the Green-Lagrange strain:

$$E = \frac{1}{2}\left(F^T F - I\right) = \frac{1}{2}\left(\left(I + \frac{\partial u}{\partial X}\right)^T \left(I + \frac{\partial u}{\partial X}\right) - I\right) = \frac{1}{2}\left(\frac{\partial u}{\partial X} + \frac{\partial u}{\partial X}^T + \frac{\partial u}{\partial X}^T \frac{\partial u}{\partial X}\right) \tag{4.1}$$

This leads to:

$$\varepsilon_{rr} = \frac{\partial u_r}{\partial r} + \frac{1}{2}\left(\frac{\partial u_r}{\partial r}^2 + \frac{\partial u_z}{\partial r}^2\right) \tag{4.2}$$

$$\varepsilon_{zz} = \frac{\partial u_z}{\partial z} + \frac{1}{2}\left(\frac{\partial u_r}{\partial z}^2 + \frac{\partial u_z}{\partial z}^2\right) \tag{4.3}$$

$$\varepsilon_{\theta\theta} = \frac{u_r}{r} + \frac{1}{2}\left(\frac{u_r}{r}\right)^2 \tag{4.4}$$

$$\varepsilon_{rz} = \frac{1}{2}\left(\frac{\partial u_r}{\partial z} + \frac{\partial u_z}{\partial r} + \frac{\partial u_r}{\partial r}\frac{\partial u_r}{\partial z} + \frac{\partial u_z}{\partial r}\frac{\partial u_z}{\partial z}\right) \tag{4.5}$$

We can recover the linear strain by ignoring the higher-order terms.

5 Spherically Symmetric Equations

For the spherically symmetric case, the nonlinear strains are derived starting from the Green-Lagrange strain:

$$E = \frac{1}{2}\left(F^T F - I\right) = \frac{1}{2}\left(\left(I + \frac{\partial u}{\partial X}\right)^T \left(I + \frac{\partial u}{\partial X}\right) - I\right) = \frac{1}{2}\left(\frac{\partial u}{\partial X} + \frac{\partial u}{\partial X}^T + \frac{\partial u}{\partial X}^T \frac{\partial u}{\partial X}\right) \tag{5.1}$$

This leads to:

$$\varepsilon_{rr} = \frac{\partial u_r}{\partial r} + \frac{1}{2}\left(\frac{\partial u_r}{\partial r}^2\right) \tag{5.2}$$

$$\varepsilon_{\theta\theta} = \frac{u_r}{r} + \frac{1}{2}\left(\frac{u_r}{r}\right)^2 \tag{5.3}$$

$$\varepsilon_{\phi\phi} = \frac{u_r}{r} + \frac{1}{2}\left(\frac{u_r}{r}\right)^2 \tag{5.4}$$

We can recover the linear strain by ignoring the higher-order terms.

6 Elasticity

For elastic behavior, a hypoelastic formulation is used, specifically,

$$\sigma_{ij}^{n+1} = \sigma_{ij}^{n} + \Delta t \mathbf{C}_{ijkl} \mathbf{D}_{kl} \tag{6.1}$$

where **C** is the elasticity tensor. For isotropic elasticity, this becomes

$$\sigma_{ij}^{n+1} = \sigma_{ij}^{n} + \Delta t \left(\delta_{ij} \lambda \mathbf{D}_{kk} + 2\mu \mathbf{D}_{ij} \right) \tag{6.2}$$

with λ as Lame's first parameter and μ as the shear modulus. This stress update occurs in the configuration at n. Thus as a final step, the stress must be rotated to the configuration at $n+1$.

7 Nonlinear Materials

Fuel materials often exhibit nonlinear mechanical behavior. As a first step to modeling this behavior, von Mises linear isotropic strain hardening via an implicit radial return method was implemented in BISON. A summary of this implementation is described in the following steps.

1. An elastic trial stress is calculated using the previous stress state and a total strain increment

$$\sigma^{trial} = \sigma_{old} + \mathbf{C}\Delta\varepsilon \tag{7.1}$$

where **C** is the linear isotropic elasticity tensor, $\Delta\varepsilon$ is the total strain increment tensor, and $\boldsymbol{\sigma}_{\mathbf{old}}$ is the stress from the previous time step.

2. A yield function is evaluated

$$f = \sigma^{trial}_{eff} - r - \sigma_{yield} \tag{7.2}$$

where f is the yield function, σ^{trial}_{eff} is the effective trial stress based on the deviatoric trial stress, r is the hardening variable, and σ_{yield} is the yield stress. If the yield function is greater than zero, then permanent deformation has occurred and a the plastic strain increment must be calculated. Otherwise, the trial stress is the new stress.

3. The hardening variable, r, and the plastic strain increment are solved via Newton iteration.

$$r = r_{old} + h\Delta p \tag{7.3}$$

$$residual = \frac{\sigma^{trial}_{effective} - 3G\Delta p - r - \sigma_{yield}}{3G + h} \tag{7.4}$$

$$\Delta p = \Delta p_{old} + residual \tag{7.5}$$

In step 3. r_{old} is the hardening variable from the previous time step, h is the hardening constant, which defines the slope of the linear strain hardening section of the stress vs. strain plot, Δp and Δp_{old} are the plastic strain increment for the current and previous time steps respectively, and G is the shear modulus. In this Newton iteration, the residual is driven to some predefined small number as the hardening variable r and the plastic strain increment Δp are updated to achieve such a small residual.

4. When the residual is sufficiently small, the new plastic strain increment is used to update a plastic strain increment tensor ($\Delta\varepsilon_p$) that is used to calculate an elastic strain ($\Delta\varepsilon_e$) from the total strain ($\Delta\varepsilon$) and a new stress increment is calculated using this new elastic strain.

$$\Delta\varepsilon^p = \frac{3}{2}\Delta p \frac{\sigma^{trial}_{dev}}{\sigma^{trial}_{eff}}, \tag{7.6}$$

$$\Delta\varepsilon^e = \Delta\varepsilon - \Delta\varepsilon^p, \tag{7.7}$$

$$\Delta\sigma = \mathbf{C}\Delta\varepsilon^e \tag{7.8}$$

5. Now, the stress and the plastic strain are updated

$$\sigma = \sigma_{old} + \Delta\sigma \tag{7.9}$$

$$p = p_{old} + \Delta p \tag{7.10}$$

6. In conventional nonlinear solvers, the material Jacobian is calculated and used to solve the nonlinear problem. Note however, that the material Jacobian is NOT required using the JFNK method. It can be used as a preconditioner and it is therefore presented here.

$$\frac{\partial\delta\sigma}{\partial\delta\varepsilon} = 2GQ\frac{\sigma_{dev}^{trial}}{\sigma_{eff}^{trial}}\frac{\sigma_{dev}^{trial}}{\sigma_{eff}^{trial}} + 2GRI + \left(K - \frac{2}{3}GR\right)II \tag{7.11}$$

where

$$R = \frac{\sigma_{eff}^{trial} - 3G\Delta p}{\sigma_{eff}^{trial}} \tag{7.12}$$

and

$$Q = \frac{3}{2}\left(\frac{h}{h+3G}\right) - R \tag{7.13}$$

The source used for guidance in implementing this plasticity model into BISON was “Introduction to Computational Plasticity” [8].

8 Material and Behavioral Models

8.1 FeCrAl

8.1.1 Thermal Properties - Kanthal APMT alloy `[ThermalKanthal]`

The temperature dependent thermal conductivity and specific heat of Kanthal APMT alloy from [9] are given in Table 8.1:

Table 8.1: Temperature dependent thermal conductivity and specific heat of Kanthal APMT alloy

Temperature [K]	Thermal Conductivity [W/m-K]	Specific Heat Capacity [J/kg-k]
293.15		480
323.15	11	
473.15		560
673.15		640
873.15	21	710
1073.15	23	670
1273.15	27	690
1473.15	29	700

Fitting these data to low order polynomials gives the following relationships for thermal conductivity (W/m-K):

$$k = -2.9216 \times 10^{-6} T^2 + 2.0972 \times 10^{-2} T + 4.5554 \tag{8.1}$$

and specific heat (J/kg-K):

$$C_p = 480, \qquad T \leq 293.15 \text{ K} \tag{8.2}$$

$$C_p = 0.3964T + 368.3, \qquad T \leq 873.15 \text{ K} \tag{8.3}$$

$$C_p = -1.25 \times 10^{-4} T^2 + 3.933 \times 10^{-1} T + 391.9, \qquad T \leq 1473.15 \text{ K} \tag{8.4}$$

$$C_p = 700, \qquad T > 1473.15 \text{ K} \tag{8.5}$$

where T is in degrees Kelvin.

8.1.2 Mechanical Properties - Kanthal APMT alloy `[MechKanthal]`

Young's modulus (Pa) and Poisson's ratio for Kanthal APMT.

$$E = 2.3778 \times 10^{11} - 6.0413 \times 10^{7} T - 1.9282 \times 10^{4} T^2 \tag{8.6}$$

$$v = 0.3 \tag{8.7}$$

Linear thermal expansion coefficient ($\frac{m}{m}$) is:

$$\Delta L/L = (1.064 \times 10^{-5} + 3.1577 \times 10^{-9} T)(T - 273.15) \tag{8.8}$$

T is temperature in K.

8.2 HT9 Martensitic Steel

8.2.1 Thermal Properties `[ThermalHT9]`

Thermal conductivity k (W/m-K) of HT9 is from [10]:

$$k = 17.622 + 2.42 \times 10^{-2} T - 1.696 \times 10^{-5} T^2, \qquad T < 1030 \text{ K} \tag{8.9}$$

$$k = 12.027 + 1.218 \times 10^{-2} T, \qquad T \geq 1030 \text{ K} \tag{8.10}$$

Specific heat C_p (J/kg-K) of HT9 is from [11]:

$$C_p = (T - 500)/6 + 500, \qquad T < 800 \text{ K} \tag{8.11}$$

$$C_p = 3(T - 800)/5 + 550, \qquad T \geq 800 \text{ K} \tag{8.12}$$

8.2.2 Mechanical Properties `[MechHT9]`

Young's modulus (MPa) and Poisson's ratio for HT9 are reported by [12].

$$E = 234468.6944 - 79.65914T - 0.0131706T^2 \tag{8.13}$$

$$v = 0.221956 + 2.643235 \times 10^{-4} T - 2.028888 \times 10^{-7} T^2 \tag{8.14}$$

Linear thermal expansion coefficient (%) [10] is:

$$\Delta L/L = -0.2191 + 5.678 \times 10^{-4} T + 8.111 \times 10^{-7} T^2 - 2.576 \times 10^{-10} T^3 \tag{8.15}$$

T is temperature in K.

8.2.3 Thermal and Irradiation Creep `[ThermalIrradiationCreepHT9]`

Thermal and irradiation creep models and material properties from [13] are used for the HT9 model. The following equation is for secondary creep.

$$\dot{\varepsilon}_{cr} = C_5 \exp(-\frac{Q_4}{RT})\bar{\sigma}^2 + C_6 \exp(-\frac{Q_5}{RT})\bar{\sigma}^5 + [B_o + A\exp(-\frac{Q}{RT})]\phi\bar{\sigma}^{1.3} \tag{8.16}$$

where:

$C_5 = 1.17 \times 10^9$
$C_6 = 8.33 \times 10^9$
$Q_4 = 83142$ (Cal/g-mol)
$Q_5 = 108276$ (Cal/g-mol)
$B_o = 1.83 \times 10^{-4}$
$A = 2.59 \times 10^{14}$
$Q = 73000$ (Cal/g-mol)
$R = 1.987$ (Cal/g-mol)
$T =$ Temperature (K)
$\phi =$ Neutron Flux$(10^{22}$ n/cm^2/s)
$\bar{\sigma} =$ Effective stress (MPa)
$\dot{\varepsilon}_{cr} =$ Effective Thermal and Irradiation Creep Strain Rate (%/s)

8.3 Molybdenum

8.3.1 Thermal Properties `[ThermalMo]`

Thermal conductivity k (W/m-K) of pure Mo metal is from [14]:

$$k = 9.128 \times 10^{-6} T^2 - 4.945 \times 10^{-2} T + 152.0 \tag{8.17}$$

Specific heat C_p (J/kg-K) of pure Mo metal is from [15]:

$$C_p = 9.74 \times 10^{-6} T^2 + 5.37 \times 10^{-2} T + 235 \tag{8.18}$$

8.3.2 Mechanical Properties `[MechMo]`

Young's modulus (Pa) and Poisson's ratio for pure Mo:

$$E = 3.349 \times 10^{11} - 5.101 \times 10^7 T \tag{8.19}$$

$$\nu = 0.31 \tag{8.20}$$

Linear thermal expansion coefficient ($\frac{m}{m}$) is:

$$\Delta L/L = (-4.985 \times 10^{-6} + 6.667 \times 10^{-10} T)(T - 273.15) \tag{8.21}$$

T is temperature in K.

8.4 Nickel-base Alloy PK33

8.4.1 Thermal Properties `[ThermalAlloy33]`

Thermal conductivity k (W/m-K) of Alloy PK33 is from [16]:

$$k = 1.4617 \times 10^{-2} T + 9.1233 \tag{8.22}$$

Specific heat C_p (J/kg-K) of Alloy PK33 is:

$$C_p = 0.177T + 431.0 \tag{8.23}$$

8.4.2 Mechanical Properties `[MechAlloy33]`

Young's modulus (Pa) and Poisson's ratio for Alloy PK33, from [16].

$$E = 2.358 \times 10^{11} - 1.667 \times 10^{8} T + 8.737 \times 10^{4} T^2 \tag{8.24}$$

$$v = 0.31 \tag{8.25}$$

Linear thermal expansion coefficient ($\frac{m}{m}$) is:

$$\Delta L/L = 1.699 \times 10^{-5} T - 5.177 \times 10^{-3} \tag{8.26}$$

T is temperature in K.

8.5 Pyrolitic Carbon

8.5.1 Irradiation-induced Strain `[PyCIrradiationStrain]`

Pyrolitic carbon experiences irradiation-induced strain which is a function of fluence. For low-density pyrolitic carbon, such as that used in the buffer layer of a TRISO fuel particle, the irradiation strain is given by [17] as

$$\dot{\varepsilon}_r = \dot{\varepsilon}_\theta = -0.176\, e^{(-1.75\Phi)} \tag{8.27}$$

where $\dot{\varepsilon}$ is in units of $1/(10^{25}\mathrm{n/m^2})$ and Φ, the fluence, is in units of $10^{25}\mathrm{n/m^2}$.

For dense pyrolitic carbon, the irradiation strain differs in the radial and tangential directions [17] of a TRISO particle:

$$\dot{\varepsilon}_r = -0.077\, e^{(-\Phi)} + 0.031 \tag{8.28}$$

$$\dot{\varepsilon}_\theta = -0.036\, e^{(-2.1\Phi)} - 0.01. \tag{8.29}$$

8.5.2 Irradiation Creep `[CreepPyC]`

The irradiation creep correlation is taken from [17] and [18]. With K as the creep constant, σ_i as one component of the principal stress, ν_c as the Poisson ratio for creep, and $\dot{\Phi}$ as the fast neutron flux, the creep rate is given as

$$\dot{\varepsilon}_1 = K[\sigma_1 + \nu_c(\sigma_2 + \sigma_3)]\dot{\Phi}. \tag{8.30}$$

The value of ν_c is 0.5. K is

$$K = K_0[1 + 2.38(1.9 - \rho)]M_{\text{Irr,Creep}} \tag{8.31}$$

where

$$K_0 = 1.996 \times 10^{-29} - 4.415 \times 10^{-32}T + 3.6544 \times 10^{-35}T^2 \tag{8.32}$$

and with $M_{\text{Irr,Creep}} = 2$, ρ in g/cm^3 and T in C. At the expense of inverting a 3×3 matrix, it is possible to determine the creep strain increment in an implicit fashion, allowing arbitrarily large time steps without unstable creep response.

8.6 Silicon Carbide

8.6.1 Irradiation Creep `[CreepSiC]`

The model for irradiation creep of silicon carbide (SiC) is taken as (see [19]):

$$\dot{\varepsilon}_{cr} = K\sigma\phi \tag{8.33}$$

where $\dot{\varepsilon}_{cr}$ is the irradiation creep rate, K is a temperature-dependent conversion factor (Pa-n/m^2)$^{-1}$, σ is the stress, and ϕ is the flux.

The reference mentioned above gives K as 2×10^{-37} (Pa-n/m^2)$^{-1}$ at 640° C and 4×10^{-37} (Pa-n/m^2)$^{-1}$ at 900° C. However, a figure in that reference seems to indicate that typical values for K are about one-tenth those mentioned in the text. Little creep data for SiC is available at lower temperatures.

8.7 Stainless Steel 316

8.7.1 Thermal Properties `[Thermal316]`

Thermal conductivity k (W/m-K) of SS 316 is fitted from [20]:

$$k = -7.301 \times 10^{-6}T^2 + 2.716 \times 10^{-2}T + 6.308 \tag{8.34}$$

Specific heat C_p (J/kg-K) of SS 316 is from [20]:

$$C_p = 428.46 + 0.1816T \tag{8.35}$$

8.7.2 Mechanical Properties `[MechSS316]`

Young's modulus (Pa) and Poisson's ratio for SS 316.

$$E = 2.15946 \times 10^{11} - 7.07727 \times 10^{7} T \tag{8.36}$$

$$v = 0.31 \tag{8.37}$$

Linear thermal expansion coefficient ($\frac{m}{m}$) is:

$$\Delta L/L = -4.34 \times 10^{-3} + 1.45 \times 10^{-5} T + 3.766 \times 10^{-9} T^2 \tag{8.38}$$

T is temperature in K.

8.8 UO_2 and MOX

8.8.1 Thermal Properties - UO_2 `[ThermalFuel]`

Five empirical models are available in BISON to compute UO_2 thermal conductivity and its dependence on temperature, porosity, burnup, and, for three of the models, Gadolinia content. Choices for UO_2 fuel include models referred to as Fink-Lucuta [21][22], Halden [23], NFIR [24], MATPRO [25], and modified NFI [26] (modifications described in [23]). The Halden, MATPRO, and modified NFI models can account for Gadolinia content.

Empirical fits for the temperature dependent specific heat of UO_2 accompany both the Fink-Lucuta and MATPRO conductivity models.

For the most part, the thermal conductivity of urania is represented as the sum of a lattice vibration (phonon) and an electronic (electron hole pair effect) term or for unirradiated material at 95% theoretical density (TD)

$$\mathrm{k_{95} = k_{phonon} + k_{electronic}} \tag{8.39}$$

The first term in Equation 8.39 is typically inversely proportional to the sum of temperature and burnup dependent functions, while the second term, usually an exponential function of inverse temperature, is inversely proportional to temperature or temperature squared. For example,

$$\mathrm{k_{phonon} = 1.0/(A + B * T + f(Bu) + g(Bu) * h(T))} \tag{8.40}$$

$$\mathrm{k_{electronic} = i(T) * exp(-F/T)} \tag{8.41}$$

where A, B, and F are constants, Bu is burnup, T is temperature, and f, g, h, and i are functions of burnup or temperature. While each of the thermal conductivity models has the basic form given by Equations 8.40 and 8.41, each has their own specific set of constants and perhaps additional corrections that account for effects of dissolved fission products, precipitated fission products, porosity, deviation from stoichiometry, and radiation damage. In general, the final conductivity corrected for these effects is given as

$$\mathrm{k = k_{95} * f_d * f_p * f_{por} * f_x * f_r} \tag{8.42}$$

where:

f_d – dissolved fission products correction
f_p – preipitated fission products correction
f_{por} – porosity correction
f_x – deviation from stoichiometry (1.0 for urania fuel but $\neq 1$ if Gadolinia present)
f_r – radiation damage correction

8.8.1.1 Fink-Lucuta

In the Fink-Lucuta model, the temperature-dependence of unirradiated material is defined using the equation suggested by Fink [21]. This relationship is then modified to account for the effects of irradiation, porosity and burnup using a series of multipliers, as outlined in detail by Lucuta et al. [22]. The Fink equation is

$$\mathrm{k_{95}} = \left(\frac{1}{7.5408 + 17.692 \cdot \mathrm{T_n} + 3.6142 \cdot \mathrm{T_n^2}} + \frac{6400}{\mathrm{T_n^{5/2}}} \exp\left(-\frac{16.35}{\mathrm{T_n}}\right)\right) \tag{8.43}$$

where T_n is the temperature in K divided by 1000. Equation 8.43 is multiplied by the following factor to obtain 100% TD thermal conductivity

$$\mathrm{k} = \mathrm{k_{95}} \cdot \left(\frac{1}{1 - (2.6 - 0.5 \cdot \mathrm{T_n}) \cdot 0.05}\right) \tag{8.44}$$

Equation 8.44 is then corrected per Equation 8.42 as perscribed by Lucuta where

$$\mathrm{f_d} = \left(\frac{1.09}{\mathrm{bu}^{3.265}} + 0.0643 \cdot \sqrt{\frac{\mathrm{T}}{\mathrm{bu}}}\right) \cdot \arctan\left(\frac{1.0}{\frac{1.09}{\mathrm{bu}^{3.265}} + 0.0643 \cdot \sqrt{\frac{\mathrm{T}}{\mathrm{bu}}}}\right) \tag{8.45}$$

$$\mathrm{f_p} = 1.0 + \left(\frac{0.019 \cdot \mathrm{bu}}{3.0 - 0.019 \cdot \mathrm{bu}}\right) \cdot \left(\frac{1.0}{1.0 + \exp\left(\frac{-(\mathrm{T} - 1200)}{100}\right)}\right) \tag{8.46}$$

$$\mathrm{f_{por}} = \left(\frac{1.0 - \mathrm{p}}{1.0 + 0.5 \cdot \mathrm{p}}\right) \tag{8.47}$$

$$\mathrm{f_r} = 1.0 - \frac{0.2}{1.0 + \exp\left(\frac{(\mathrm{T} - 900)}{80}\right)} \tag{8.48}$$

where T is the temperature in K, p is the porosity, and bu is the burnup in at.%.

The Fink-Lucuta model is valid from 298 to 3120 K [27].

8.8.1.2 MATPRO

The MATPRO model [25] is based on an equation proposed by Ohira and Itagakia [26]. The thermal conductivity for 95% theroetical density is given as

$$\mathrm{k}_{95} = 1/(\mathrm{term0} + \mathrm{term1} + \mathrm{term2} + \mathrm{term3} + \mathrm{term4} \cdot \mathrm{term5}) + \mathrm{term6} \tag{8.49}$$

where the recriprocal expression and term6 correspond to $\mathrm{k}_{\mathrm{phonon}}$ and $\mathrm{k}_{\mathrm{electronic}}$, respectively. The terms are defined as

$$\begin{aligned}
\mathrm{term0} &= 0.0452 \\
\mathrm{term1} &= 0.000246 \cdot \mathrm{T} \\
\mathrm{term2} &= 0.00187 \cdot \mathrm{Bu} \\
\mathrm{term3} &= 1.1599 \cdot \mathrm{Gdcon} \\
\mathrm{term4} &= (1 - 0.9 \cdot \exp(-0.04 \cdot \mathrm{Bu})) \cdot 0.038 \cdot \mathrm{Bu}^{0.28} \\
\mathrm{term5} &= 1/(1 + 396 \cdot \mathrm{exp(\text{-}6380/T)}) \\
\mathrm{term6} &= 3.5\mathrm{e}9/\mathrm{T}^2 \cdot \mathrm{exp(\text{-}16360/T)}
\end{aligned}$$

and T is temperature in K, Bu is burnup in MWd/kgU, and Gdcon is the Gadolinia concentration in wt.%. Equation 8.49 is multiplied by the appropriate factor to return the thermal conductivity to 100% TD and then multiplied by a density correction factor (similar to Equation 8.47 but written in terms of %TD) to provide a thermal conductivity representative of the material of interest

$$\mathrm{k} = \mathrm{k}_{95} \cdot 1.0789 \cdot \frac{\mathrm{D}}{(1 + 0.5 \cdot (1 - \mathrm{D}))} \tag{8.50}$$

where D is the fractional TD. The multiplier 1.0789 is the inverse of the density correction factor evaluated at 0.95 TD.

The MATPRO correlation is valid over the following ranges [23]

$$\begin{aligned}
&300 \leq \mathrm{T\ (K)} \leq 3000 \\
&0 \leq \mathrm{Bu} \leq 62\ \mathrm{MWd/kgU} \\
&0.92 \leq \mathrm{D} \leq 0.97 \\
&0 \leq \mathrm{Gdcon} \leq 10\ \mathrm{wt.\%}
\end{aligned}$$

Figure 8.1 compares the two models as a function of temperature and burnup for fully dense UO_2.

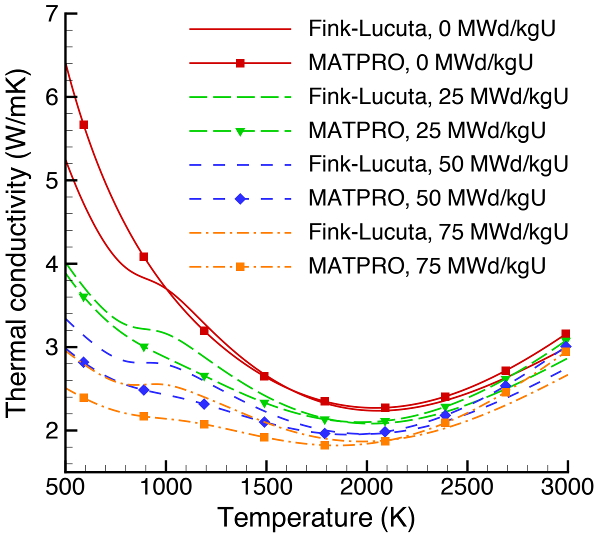

Figure 8.1: A comparison of the Fink-Lucuta and MATPRO empirical models for the thermal conductivity of full density UO_2, as a function of temperature and burnup.

8.8.1.3 Halden

The Halden model has the same form as Equation 8.49. However, the terms are different, and different temperature and burnup units are used. For 95% TD fuel, the terms are

$$\begin{aligned}
\text{term0} &= 0.1148 \\
\text{term1} &= 1.1599 \cdot \text{Gdcon} \\
\text{term2} &= 1.1599 \cdot \text{f}_x \\
\text{term3} &= \text{4e-3} \cdot \text{BuUO2} \\
\text{term4} &= \text{2.475e-4} \cdot (1 \text{ - } \text{3.33e-3} \cdot \text{BuUO2}) \cdot \min(1650,\text{Tc}) \\
\text{term5} &= 1 \\
\text{term6} &= \text{1.32e-2} \cdot \exp(0.00188 \cdot \text{Tc})
\end{aligned}$$

where Gdcon is the Gadolinia concentration in wt.%, f_x is the deviation from stoichiometry, i.e. (2 - oxygen/metal ratio), BuUO2 is the burnup in MWd/kgUO2, and Tc is the temperature in C. Equation 8.50 is used to compute the thermal conductivity at the TD of interest.

The Halden UO_2 correlation is valid over the following ranges [23]

$$300 \leq \text{T (K)} \leq 3000$$
$$0 \leq \text{Bu} \leq 62 \text{ MWd/kgU}$$
$$0.92 \leq \text{D} \leq 0.97$$
$$0 \leq \text{Gadolinia content} \leq 10 \text{ wt.\%}$$

Figure 8.2 compares the the Fink-Lucuta and Halden models as a function of temperature and burnup for 95% theoretical density UO_2.

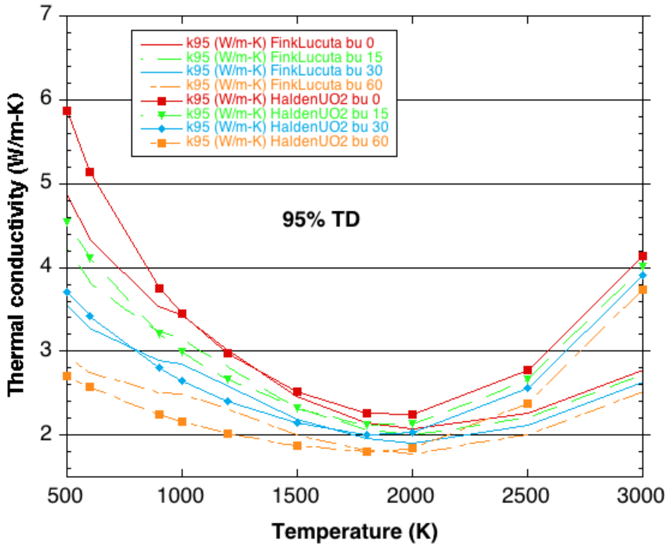

Figure 8.2: A comparison of the Fink-Lucuta and Halden empirical models for the thermal conductivity of 95% theoretical density UO_2, as a function of temperature and burnup.

8.8.1.4 NFIR

The NFIR correlation also has the general form of Equation 8.39. However, the NFIR model contains a temperature dependent thermal recovery function that accounts for self-annealing of defects in the fuel as it heats up. The ultimate effect of the self-annealing is a slight increase of the thermal conductivity over a range of temperatures up to ~1200 K. As a result of this formulation, two components of k_{phonon} are used, one at the start of thermal recovery and one at the end of thermal recovery. The thermal recovery function is used to interpolate between these two values to compute k_{phonon}. Thus

$$k_{95} = (1 - RF(Tc)) \cdot k_{phonon,start} + RF(Tc) \cdot k_{phonon,end} + k_{electronic} \tag{8.51}$$

where RF(Tc) is the thermal recovery function, Tc is temperature in C, $k_{phonon,start}$ is the phonon contribution at the start of thermal recovery, and $k_{phonon,end}$ is the phonon contribution at the end of thermal recovery. The individual terms are

$$\mathrm{k}_{\mathrm{phonon,start}} = 1/(9.592\text{e-}2 + 6.14\text{e-}3 \cdot \mathrm{Bu} - 1.4\text{e-}5 \cdot \mathrm{Bu}^2 + (2.5\text{e-}4 - 1.81\text{e-}6 \cdot \mathrm{Bu}) \cdot \mathrm{Tc}) \quad (8.52)$$

$$\mathrm{k}_{\mathrm{phonon,end}} = 1/(9.592\text{e-}2 + 2.6\text{e-}3 \cdot \mathrm{Bu} + (2.5\text{e-}4 - 2.7\text{e-}7 \cdot \mathrm{Bu}) \cdot \mathrm{Tc}) \quad (8.53)$$

$$\mathrm{RF(Tc)} = 0.5 \cdot (1+\tanh((\mathrm{Tc}-900)/150)) \quad (8.54)$$

$$\mathrm{k}_{\mathrm{electronic}} = 1.32\text{e-}2 \cdot \exp(1.88\text{e-}3 \cdot \mathrm{Tc}) \quad (8.55)$$

where Bu is burnup in MWd/kgU. Equation 8.51 is then multiplied by a temperature dependent density correction factor to get

$$k = k_{95} \frac{[1 - (2.58 - 5.8\text{e-}4 \cdot \mathrm{Tc}) \cdot (1 \text{ - } \mathrm{D})]}{[1 - 0.05 \cdot (2.58 - 5.8\text{e-}4 \cdot \mathrm{Tc})]} \quad (8.56)$$

where D is the fractional density. Figure 8.3 compares the the Fink-Lucuta and NFIR models as a function of temperature and burnup for 95% theoretical density UO_2.

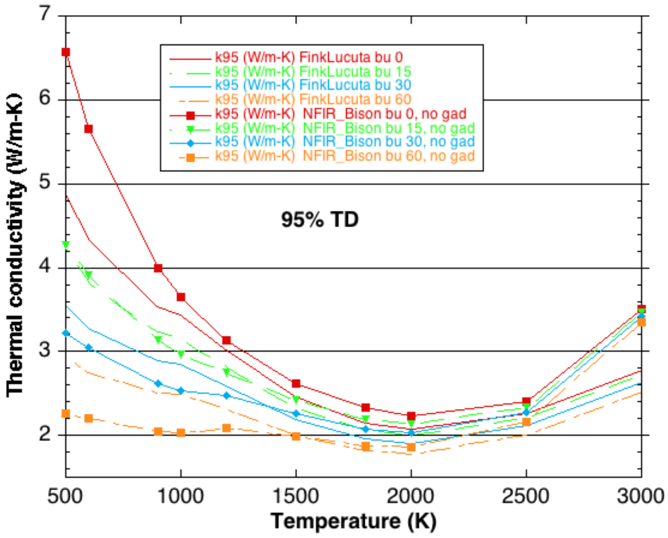

Figure 8.3: A comparison of the Fink-Lucuta and NFIR empirical models for the thermal conductivity of 95% theoretical density UO_2, as a function of temperature and burnup.

8.8.1.5 Modified NFI

The modified NFI model is also of the form of Equation 8.49. Terms are defined as

$$
\begin{aligned}
&\text{term0} = 0.0452 \\
&\text{term1} = 1.1599 \cdot \text{Gdcon} \\
&\text{term2} = 2.46e-4 \cdot \text{T} \\
&\text{term3} = 1.87\text{e-}3 \cdot \text{Bu} \\
&\text{term4} = (1-0.9 \cdot \exp(-0.04 \cdot \text{Bu})) \cdot 0.038 \cdot \text{Bu}^{0.28} \\
&\text{term5} = 1/(1+396 \cdot \exp(\text{-}6380/\text{T})) \\
&\text{term6} = 3.5\text{e}9/\text{T}^2 \cdot \exp(\text{-}16360/\text{T})
\end{aligned}
$$

where Gdcon is the Gd concentration in wt.%, T is the temperature in K, Bu is the burnup in MWd/kgU. Again, Equation 8.50 is used to convert to the TD of interest.

The modified NFI model is valid over the following ranges [23]

$$
\begin{aligned}
&300 \leq \text{T (K)} \leq 3000 \\
&0 \leq \text{Bu} \leq 62 \text{ MWd/kgU} \\
&0.92 \leq \text{D} \leq 0.97 \\
&0 \leq \text{Gdcon} \leq 10 \text{ wt.\%}
\end{aligned}
$$

Figure 8.4 compares the Fink-Lucuta and NFI modified models as a function of temperature and burnup for 95% theoretical density UO_2.

8.8.2 Thermal Properties - MOX `[ThermalFuel]`

Three models are available to compute MOX thermal properties. For these models, thermal conductivity of unirradiated material is first defined. In general, these relationships are then multiplied by correction factors, which account for effects of irradiation, burnup, MOX content, and porosity. The corrections factors used in BISON have been developed by Lucuta et al. [22] and are recommended by Carbajo et al. [27].

8.8.2.1 Duriez-Ronchi

The first model is recommended by Carbajo et al. in [27] and is a combination of Duriez [28] and Ronchi [29] models. In this first model, thermal conductivity of unirradiated MOX is given by:

$$\lambda_0(T,x) = 1.158 \cdot \left(\frac{1}{A+CT_n} + \frac{6400}{T_n^{5/2}} \exp\left(-\frac{16.35}{T_n} \right) \right) \tag{8.57}$$

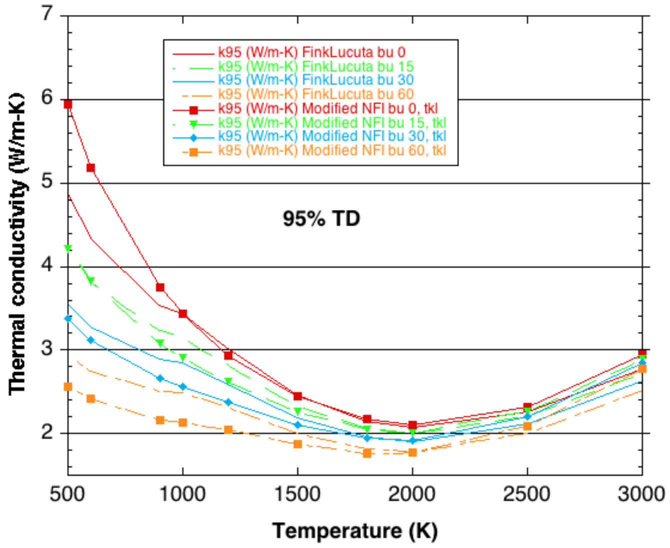

Figure 8.4: A comparison of the Fink-Lucuta and modified NFI empirical models for the thermal conductivity of 95% theoretical density UO_2, as a function of temperature and burnup.

where:

$\lambda_0 =$ thermal conductivity in $\mathrm{W \cdot m^{-1} \cdot K^{-1}}$
$T_n = T\ (\mathrm{K})/1000$ reduced temperature
$x =$ deviation from stoichiometry (unitless)
$A(x) = 2.85x + 0.035$
$C(x) = -0.715x + 0.286$

This model provides temperature and deviation from stoechiometry. It is valid from 700 to 3100 K, x less than 0.05, and plutonium concentration between 3 wt.% and 15 wt. %. According to [27], thermal conductivity does not depend on Pu concentration in this range. Thus this model is valid essentially for thermal reactor MOX.

8.8.2.2 Amaya

The second model available in BISON has been proposed by Amaya et al. [30]. Unlike the previous model, Amaya provides a plutonium concentration dependence. It starts from pure UO_2 thermal conductivity and applies corrections to account for Pu content. Unirradiated MOX thermal conducitivity is given by:

$$\lambda_{MOX,0} = \sqrt{\frac{\lambda_0}{D_{0,Pu}\exp(D_{1,Pu} \cdot T) \cdot y}} \cdot \arctan\left(\sqrt{D_{0,Pu}\exp(D_{1,Pu} \cdot T) \cdot y \cdot \lambda_0}\right) \tag{8.58}$$

where:

$\lambda_{MOX,0} =$ MOX unirradiated thermal conductivity in $\mathrm{W} \cdot \mathrm{m}^{-1} \cdot \mathrm{K}^{-1}$

$\lambda_0 =$ UO_2 unirradiated thermal conductivity in $\mathrm{W} \cdot \mathrm{m}^{-1} \cdot \mathrm{K}^{-1}$

$T =$ temperature (K)

$y =$ plutonium concentration (wt.%)

$D_{0,Pu} = 0.209 \ \mathrm{m} \cdot \mathrm{W} \cdot \mathrm{K}^{-1}$

$D_{1,Pu} = 1.09 \cdot 10^{-3} \ \mathrm{K}^{-1}$

BISON uses Fink model to compute unirradiated UO_2 thermal conductivity. Amaya model's coefficients have been fitted in the temperature range from 400 K to 1500 K and the plutonium concentration up to 30 wt.% ([30]). Figure 8.5 shows a comparison of the computed thermal conductivities for the Fink-Lucuta (for reference), Fink-Amaya, and Duriez-Ronchi models for unirradiated MOX at 95% theoretical density.

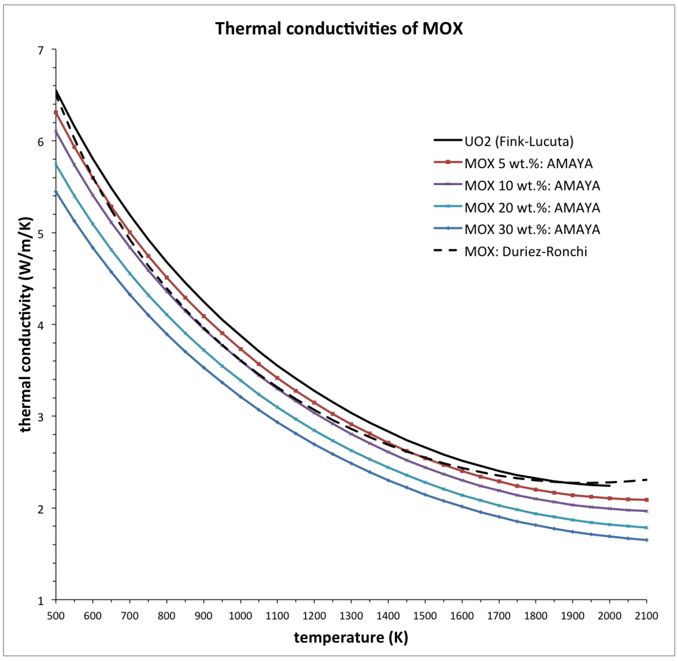

Figure 8.5: Unirradiated thermal conductivities for UO_2 and MOX from different models implemented in BISON.

8.8.2.3 Halden

The Halden correlation discussed in the previous section for urania fuel is also applicable, with one change, to MOX fuel. Reduction in thermal conductivity due to the presence of mixed oxides is accounted for by multiplying the k_{phonon} term in Equation 8.39 by 0.92. This is consistent with the statement above regarding the lack of dependence of MOX thermal conductivity on

Pu concentration. The $k_{\text{electronic}}$ part of the equation is unchanged and Equation 8.50 is used to account for the TD of interest.

The Halden MOX correlation is valid over the following ranges [23]

$$
\begin{aligned}
&300 \leq \mathrm{T\ (K)} \leq 3000\\
&0 \leq \mathrm{Bu} \leq 62\ \mathrm{MWd/kgU}\\
&0.92 \leq \mathrm{D} \leq 0.97\\
&0 \leq \text{plutonia content} \leq 7\ \text{wt.\%}\\
&\text{plutonia particle size} < \text{20e-6 m}
\end{aligned}
$$

Figure 8.6 is a comparison of the Fink-Lucuta (for reference) urania correlation and the Fink-Amaya, Duriez-Ronchi, and Halden correlations for MOX for unirradiated 95% theoretical density MOX fuel with 0.07% Pu concentration.

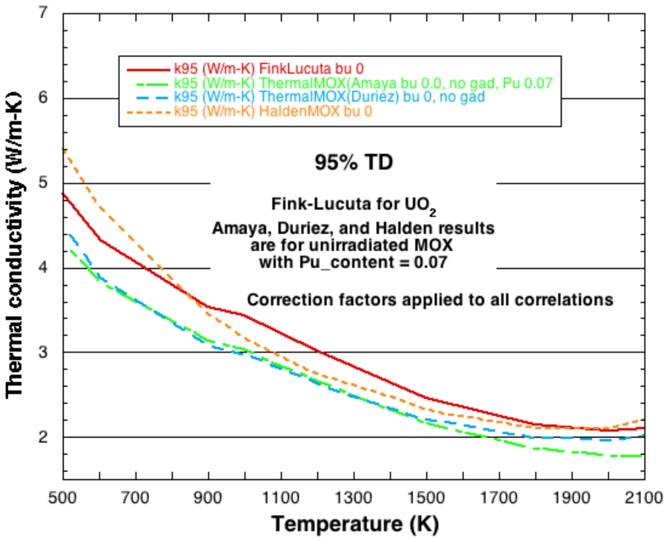

Figure 8.6: Unirradiated thermal conductivities for UO_2 (for reference) and MOX from different models implemented in BISON. Results are for 95% theoretical density and Pu concentraton of 7 wt.%. Correction factors appropriate for each correlation have been applied.

8.8.3 Densification `[VSwellingUO2]`

Fuel densification is computed using the ESCORE empirical model [31] given by:

$$\varepsilon_D = \Delta\rho_0 \left(e^{\left(\frac{Bu\, ln(0.01)}{C_D Bu_D}\right)} - 1 \right) \tag{8.59}$$

where ε_D is the densification strain, $\Delta\rho_0$ is the total densification that can occur (given as a fraction of theoretical density), Bu is the burnup, and Bu_D is the burnup at which densification is complete. For temperatures below 750 °C the parameter C_D is given by $7.2-0.0086(T-25)$; above 750 °C it is 1.0 (T in °C). To eliminate the discontinuity in C_D, BISON uses $7.235-0.0086(T-25)$ below 750 °C.

In MATPRO ([25]), the same model is provided for UO_2 and MOX. As this correlation relies on a wide database, this model is also used in BISON for MOX densification.

8.8.4 Fission Product Swelling `[VSwellingUO2]`

Empirical relations from MATPRO [25] are available in BISON for calculating the swelling due to both solid and gaseous fission products. The same model is provided for both UO_2 and MOX. Solid fission product swelling is expressed as a simple linear function of burnup:

$$\Delta\varepsilon_{sw-s} = 5.577 \times 10^{-5} \rho \Delta Bu \tag{8.60}$$

where $\Delta\varepsilon_{sw-s}$ is the volumetric solid swelling increment, ΔBu the burnup increment (fissions/atoms-U), and ρ is the density (kg/m^3). Swelling due to gaseous fission products is approximated by a semi-empirical model:

$$\begin{aligned}\Delta\varepsilon_{sw-g} = {} & 1.96 \times 10^{-31} \rho \Delta Bu (2800-T)^{11.73} \\ & * e^{-0.0162(2800-T)} e^{-0.0178 \rho Bu}\end{aligned} \tag{8.61}$$

where $\Delta\varepsilon_{sw-g}$ is the volumetric gas swelling increment, Bu and ΔBu are the burnup and burnup increment (fissions/atoms-U), respectively, ρ is the density (kg/m^3) and T is the temperature (K). Figure 8.7 shows a plot of the gaseous and total fission product swelling as a function of temperature and burnup. The MATPRO [25] correlations indicate that gaseous swelling does not become significant until above 1500 K and is saturated at a burnup of 20 MWd/kgU.

Alternatively, the gaseous fission product swelling can be calculated using a physics-based model that takes into account the coupling with the fission gas release (see Subsection 10.1).

8.8.5 Relocation `[RelocationUO2]`

One way to model the effect of UO_2 cracking on gap width is fuel relocation. Thermal gradients in a LWR fuel pellet result in corresponding stress gradients that exceed the fuel fracture stress, causing radial cracks. The free surfaces of the crack result in a overall increase of fuel pellet diameter. This effect can be modeled by applying a radial strain to the fuel pellet. This strain is similar to a volumetric strain, but only in the radial direction. A method for calculating this strain is the ESCORE relocation model [32] which is given as

$$\left(\frac{\Delta D}{D_o}\right)_{REL} = 0.80 Q \left(\frac{G_o}{D_o}\right) \left(0.005 Bu^{0.3} - 0.20 D_o + 0.3\right) \tag{8.62}$$

This relocation model is a function of power, as-fabricated pellet diameter, as-fabricated gap thickness, and burnup. The model is applicable between 8 and 22 kW/ft and to burnup levels between 0 and 11,500 MWd/MTU, and mean-diameter measurements were used in the correlation

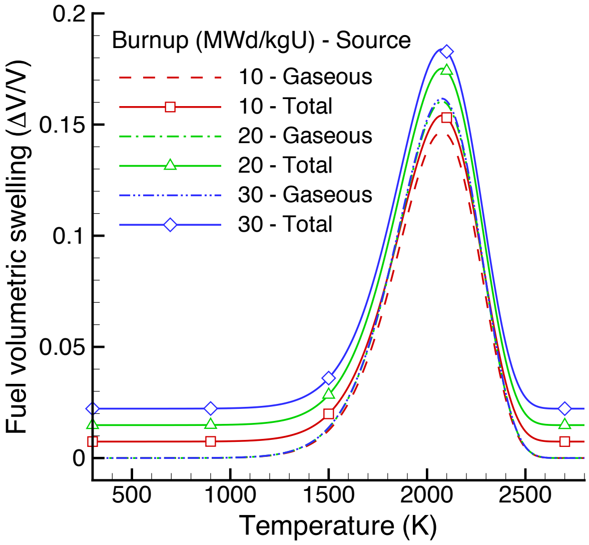

Figure 8.7: UO_2 gaseous and total swelling, as a function of temperature and burnup, based on the MATPRO [25] correlations.

development. The following is a list of variables definitions.

$\left(\frac{\Delta D}{D_o}\right)_{REL}$: Diametral strain due to relocation,

D_o : As-fabricated cold diameter of the pellet (in),

q' : Pellet average linear heating rate (kW/ft),

Bu : Pellet average fuel burnup (MWd/MTU), and

G_o : As-fabricated cold diametral gap (in)

$$Q : \begin{cases} 0 & \text{for } q' \leq q_1 \\ (q' - 6)^{1/3} & \text{for } q_1 < q' \leq q_2 \\ (q' - 10)/2 & \text{for } q' > q_2 \end{cases}$$

q_1 : 6 kW/ft

q_2 : 14 kW/ft

The fuel relocation strain is applied incrementally by calculating the relocation strain at the burnup for the current step and subtracting the relocation strain at the previous burnup. In other applications of this model, the addition of relocation strain is stopped when the gap is closed. In BISON, the relocation strain is stopped at a specified burnup.

Note that the pellet average linear heating rate q' has units of kW/ft in the empirical model. However, this quantity is passed into the model as a function with units of W/m. The conversion is handled inside the model.

It has been observed that the 6 kW/ft threshold for the initiation of relocation is well beyond the level expected to cause cracking in the fuel. For this reason, a modified ESCORE model is available. For this model,

$$\left(\frac{\Delta D}{D_o}\right)_{REL} = q(0.8)(2)\left(\frac{G_o}{D_o}\right)\left(0.005Bu^{0.3} - 0.20D_o + 0.3\right)/q_2 \tag{8.63}$$

when q_1 is less than $q^{'}$ and q_1 is less than 6 kW/ft.

It is also possible to use the GAPCON model for relocation [33]. This model is given as

$$u^{rel} = (42b/(1+b) + 0.274q^{'} + 3)G_o/100 \tag{8.64}$$

where u^{rel} is the displacement due to relocation, $b = e^{(-4+Bu^{0.25})}$, $q^{'}$ is the linear heating rate (kW/m), Bu is burnup (MWd/MTU), and G_o is the as-fabricated cold gap.

8.8.6 Thermal and Irradiation Creep - UO$_2$ `[CreepUO2]`

A model for combined secondary thermal creep and irradiation creep of UO$_2$ fuel is available, with the creep rate modeled as a function of time, temperature, effective stress, density, grain size, fission rate, and oxygen to metal ratio (O/M). The constitutive relation is taken from the MATPRO FCREEP material model [25] and given as

$$\dot{\varepsilon} = \frac{A_1 + A_2\dot{F}}{(A_3+D)G^2}\sigma e^{\left(\frac{-Q_1}{RT}\right)} + \frac{A_4}{(A_6+D)}\sigma^{4.5}e^{\left(\frac{-Q_2}{RT}\right)} + A_7\dot{F}\sigma e^{\left(\frac{-Q_3}{RT}\right)} \tag{8.65}$$

where $\dot{\varepsilon}$ is the creep rate (1/s), σ is the effective (Mises) stress (Pa), T is the temperature (K), D is the fuel density (percent of theoretical), G is the grain size (μm), $\dot{F}$ is the volumetric fission rate (fissions/m^3-s), Q_i are the activation energies (J/mol), R is the universal gas constant (8.3143 J/mol-K) and A_{1-7} are material constants given as $A_1 = 0.3919$, $A_2 = 1.3100x10^{-19}$, $A_3 = -87.7$, $A_4 = 2.0391x10^{-25}$, $A_6 = -90.5$, and $A_7 = 3.7226x10^{-35}$. The first term represents diffusional thermal creep and is applicable to low stress and low temperature conditions. The second term represents thermal dislocation or power-law creep and is applicable to high stress and high temperature conditions. Note that irradiation effects are included in both the first and third terms.

The activation energies for the thermal creep terms (Q_1 and Q_2) are strongly dependent upon the fuel oxygen to metal ratio x and, in MATPRO, are defined using the Arrhenius type relations

$$Q_1 = 74,829f(x) + 301,762 \tag{8.66}$$

$$Q_2 = 83,143f(x) + 469,191 \tag{8.67}$$

where the energies are given in J/mole and

$$f(x) = \frac{1}{e^{\left(\frac{-20}{log(x-2)}-8\right)}+1} \tag{8.68}$$

This function is plotted in Figure 8.8. The activation energy for the irradiation term (Q_3) is given in MATPRO as 21,759 J/mole.

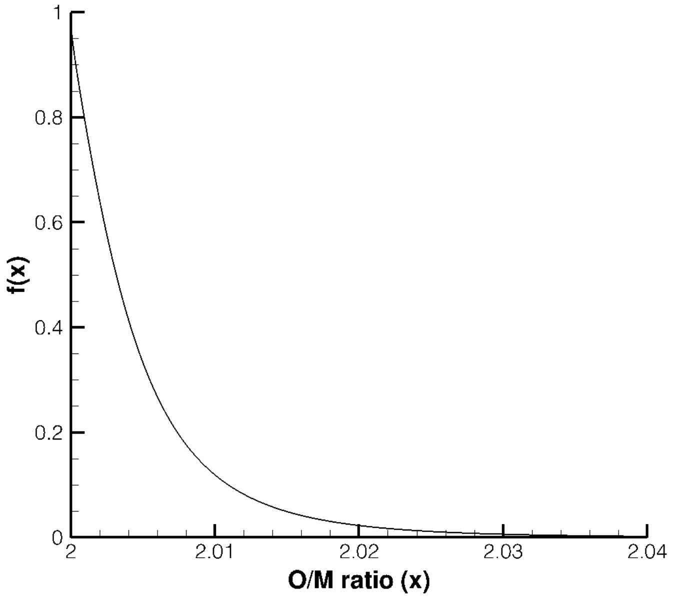

Figure 8.8: The function defining the dependence of the activation energies for thermal creep on the UO_2 oxygen to metal ratio.

In MATPRO, a transition stress is defined to govern the transition between the first (low stress) and second (high stress) regions. When the applied stress is larger than the transition stress, the applied stress is used in the power-law relation and the transition stress is used in the linear creep relation. When the applied stress is lower than the transition stress, the applied stress is used in the linear relation and the power-law contribution is zero. Mai et al. [34] investigated the MATPRO transition approach in comparison to experimental data and concluded that a better fit to the data could be achieved by simply ignoring the transition stress and applying both the low and high stress terms in all cases. This approach, termed here the Modified MATPRO model, has been adopted in BISON. The procedure outlined above for time-independent plasticity was used here to implement time-dependent plasticity (creep).

Young's modulus, Poisson's ratio and the coefficient of thermal expansion can each be specified in two ways. The values can be given directly, or the values can be computed using MATPRO correlations.

8.8.7 Stress-induced Densification - UO_2 `[HotPressingUO2]`

Creep or instantaneous plastic flow surrounding pores in ceramic UO2 fuel pellet under pressure can reduce pore volume, and as a consequence, reduce fuel porosity and increase fuel density. This is a densification mechanism of UO_2 fuel under compressive stresses, which contributes to fuel densification in addition to the irradiation induced densification. Such mechanical densification process is more pronounced at high temperatures with high creep rate or plastic deformations, and it is also referred to as hot-pressing.

The mathematical model of hot-pressing of ceramic UO_2 was described in a classical paper by Rashid [35]. By using an analogy of close-packed spherical shells in infinite media under hydrostatic compression, model on the stress-induced densification based on the mechanism of instantaneous plasticity and creep was derivied. This section describes the implementation of the hot-pressing model based on the mechanisms of creep and plasticity as follows. The new material class `[HotPressingUO2]` in the BISON code is inheritated from `[CreepUO2]` described in previous section.

- Creep

  For creep that follows power-law

  $$\dot{\varepsilon} = A\sigma^n \tag{8.69}$$

  The tangential creep rate of porous media, with density ρ, at the pore surface is given as in Ref. [35].

  $$\dot{\varepsilon}_t = \frac{A}{2}\left(\frac{3}{2n}\right)^n \left(\frac{1}{(0.74(1-\rho))^{1/n}-1}\right)^n P^n \tag{8.70}$$

  And, the volumetric creep rate is

  $$\dot{\varepsilon}_V = 6\nu_0 A P^n \tag{8.71}$$

  Hot-pressing parameter ν_0 is defined as

  $$\nu_0 = \frac{1}{4}\left(\frac{3}{2n}\right)^n \left(\frac{1}{(0.74(1-\rho))^{1/n}-1}\right)^n P^n \tag{8.72}$$

  Where
  P the hydrostatic pressure (Pa)
  n is the exponent in the power law creep equation
  A is the leading coefficient in the power law creep equation
  ρ is the fractional density (dimensionless)
  $\dot{\varepsilon}$ is the creep rate
  Subscript t and V represent tangential and volumetric components respectively.

  This material parameter ν_0 is used in the hot-pressing model for the volumetric creep of UO_2. The creep of UO_2 involves several mechanisms, and in their mathematical descriptions, different exponent n could be used for the different mechanisms. The volumetric creep strain implemented in BISON code is assumed to be the combination of all the creep strains together. From Eq. 8.72, the hot-pressing parameter depends on the fuel density. With the increase of fuel density, the parameter ν_0 would be reduced; when fractional density approaches 1.0, the parameter ν_0 approaches zero, and the densification would essentially be terminated, i.e., the volumetric creep strain rate in Eq. 8.71 becomes zero. A plot of the hot-pressing parameter versus initial density at different n is shown in Figure 8.9.

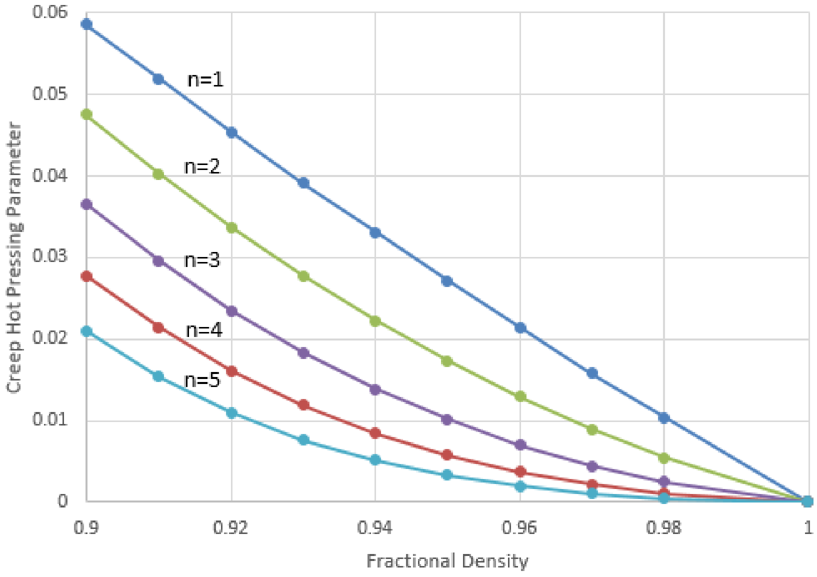

Figure 8.9: Hot-pressing parameter ν_0 versus fractional density

- Instantaneous Plasticity

  In Ref. [35], yield criterion of UO_2 is described in a modified Mohr-coulomb criterion. Eq. 8.73 through Eq. 8.76 summarize what have been described in Ref. [35].

$$f = J_2 + \alpha J_1^2 - K = 0 \tag{8.73}$$

The incremental plastic strain is given as:

$$\Delta\varepsilon_{ij}^P = \lambda(S_{ij} + 2\alpha J_1 \delta_{ij}) \tag{8.74}$$

where
$J_1 = \sigma_{ii}$
$J_2 = \frac{1}{2} S_{ij} S_{ij}$
$S_{ij} = \sigma_{ij} - \frac{1}{3} J_1 \delta_{ij}, i \neq j$
δ_{ij} is the Kcronecker delta, zero for $i \neq j$ and unity for $i = j$

The volumetric strain increment is

$$\Delta\varepsilon_{ii}^P = 6\lambda\alpha J_1 \tag{8.75}$$

α defines a material parameter that relates to the yield stress of 100% UO_2 density.

$$\alpha = \left(\frac{Y(\rho_0)/Y_s}{2/\sqrt{3}\ln(0.74/(1-\rho))} \right)^2 \tag{8.76}$$

Where $Y(\rho_0)$ is the yield stress of UO_2 at initial density ρ_0, and Y_s is the yield stress at 100% UO_2 density. The determination of α needs experimental data on the yield stress of UO_2 with different porosities, which is scarce in the literatures. Instead, an approximation is made in the code by using a constant ratio of $Y(\rho_0)/Y_s$=0.95. The resultant equation of α in the BISON code is

$$\alpha = \frac{0.0752}{(\ln(0.74/(1-\rho))^2} \tag{8.77}$$

λ however is not defined in Ref. [35]. To implement the model in BISON, a new flow rule is used. The yield criterion is formulated as:

$$f = \sqrt{J_2 + \alpha J_1^2} = K \tag{8.78}$$

The effective stress is derived as:

$$\sigma_{eff} = \sqrt{3(J_2 + \alpha J_1^2)} \tag{8.79}$$

The new flow rule used in BISON is provided in following equations.

$$\Delta\varepsilon_{ij}^P = \frac{3}{2}\frac{S_{ij}}{\sigma_{eff}}\Delta\varepsilon^P, i \neq j \tag{8.80}$$

$$\Delta\varepsilon_V^P = 3\sqrt{\frac{3\alpha}{2}}\frac{J_1}{\sigma_{eff}}\Delta\varepsilon^P \tag{8.81}$$

- Yield Stress Model
  The hot-pressing or mechanical densification under instantaneous plastic flow depends on the yield strength of UO_2, which is currently not available in BISON code. A linear hardening material model is used for modeling the yield stress of UO_2. The yield stress for the linear hardening material is

  $$\sigma_{eff} = \sigma_y + H\Delta\varepsilon^P \tag{8.82}$$

  Where
  σ_y is the initial yield stress
  σ_{eff} is the new yield stress (effective stress)
  $\Delta\varepsilon^P$ is the effective incremental plastic strain
  H is the hardening modulus
  The incremental effective plastic strain and new yield stress are computed in BISON using radial return method.

8.8.8 Thermal and Irradiation Creep - MOX `[CreepMOX]`

The creep model for MOX is a combined model from MATPRO [25] and Guerin [36]. Experimental data used by MATPRO for MOX cover indeed a range of temperature above 1500 K, so that the proposed model accounts essentially for thermal creep. In [36], Guerin provides an semi-empirical law for MOX irradiation creep, hired from Milet's experiments, whose results have been published in [37]. MATPRO provides a time-dependant multiplier which allows to account for primary and secondary creep. Thus the creep model for MOX implemented in BISON is given by:

$$\dot{\varepsilon}_{cr} = (1 + a\exp(-b \cdot t)) \cdot \dot{\varepsilon}_s \tag{8.83}$$

with

$$\begin{aligned}
\dot{\varepsilon}_s =& \frac{B_1 + B_2\dot{F}}{G^2}\sigma\exp\left(-\frac{Q_3}{T} + B_7(1-D) + B_4 C\right) && (8.84)\\
&+ B_5\sigma^{4.5}\exp\left(-\frac{-Q_4}{T} + B_7(1-D) + B_4 C\right) && (8.85)\\
&+ A\sigma\dot{F} && (8.86)
\end{aligned}$$

where

$T =$ Temperature (K)
$\sigma =$ Effective stress (Pa)
$\dot{F} =$ Fission rate $\mathrm{m}^{-3} \cdot \mathrm{s}^{-1}$
$G =$ grain size (μm)
$C = \mathrm{PuO_2}$ concentration (wt.%)

and in SI

$a = 2.5$
$b = 1.40 \cdot 10^{-6}$
$A = 4.8\dot{1}0^{-36}$
$B_1 = 0.1007$
$B_2 = 7.57 \cdot 10^{-20}$
$B_3 = 33.3$
$B_4 = 0.014$
$B_5 = 6.4691 \cdot 10^{-25}$
$B_7 = 10.3$
$Q_3 = 55354.0$
$Q_4 = 70451.0$

Figure 8.10 shows a comparison between creep models implemented in BISON for UO_2 and MOX.

The time origin for primary creep is updated in BISON when the stress rate is greater than a value specified by the user. Two successive time origins cannot be closer than 5 times the characteristic time of transient creep.

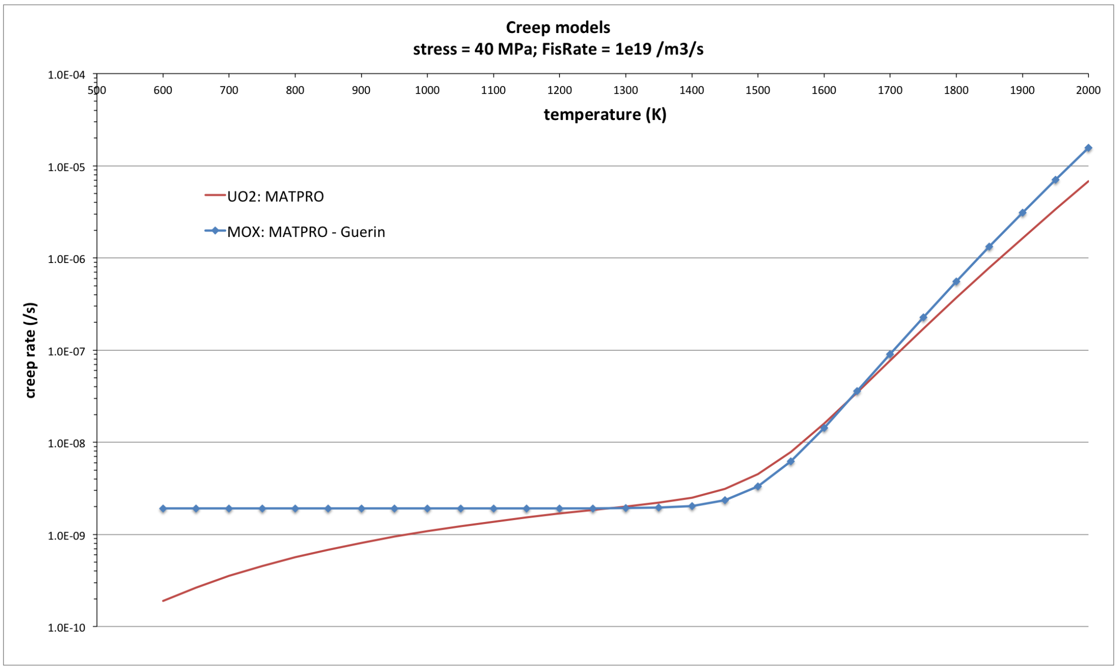

Figure 8.10: Comparison of creep rates for MOX and UO_2. The creep rate for MOX is higher than that of UO_2.

8.8.9 Smeared Cracking

In ceramic fuel such as UO_2, a significant temperature gradient develops from the fuel center to the radial edge. This gradient appears early and is strong enough to induce cracking in the fuel due to the accompanying stress. The cracks reduce the stress in the fuel and increase the effective fuel volume (decrease the gap size).

A smeared cracking model in BISON may be invoked to account for this cracking. A smeared cracking model adjusts the elastic constants at material points as opposed to introducing topographic changes to the mesh, as would be the case with a discrete cracking model.

When the smeared cracking model is active, principal stresses are compared to a critical stress. If the material stress exceeds the critical stress, the material point is considered cracked in that direction, and the stress is reduced to zero. From that point on, the material point will have no strength unless the strain becomes compressive.

The orientation of the principal coordinate system is determined from the eigenvectors of the elastic strain tensor. However, once a crack direction is determined, that direction remains fixed and further cracks are considered in directions perpendicular to the original crack direction. Note that for axisymmetric problems, one crack direction is known *a priori*. The theta or out-of-plane direction is not coupled to the r and z directions (i.e., no $r\theta$ or $z\theta$ shear strain/stress exists) and is therefore a known or principal direction.

If we store a scalar value, c_i, for each of the three possible crack directions at a material point, these in combination with the principal directions (eigenvectors or rotation tensor) provide a convenient way to eliminate stress in cracked directions. A value of 1 for c_i indicates that the material point has not cracked in that direction. A value very close to zero (not zero for numerical reasons) indicates that cracking has occurred.

We define a cracking tensor in the cracked orientation as **c**:

$$\mathbf{c} = \begin{bmatrix} c_1 & & \\ & c_2 & \\ & & c_3 \end{bmatrix}. \tag{8.87}$$

The rotation tensor **R** is defined in terms of the eigenvectors e_i:

$$\mathbf{R} = \begin{bmatrix} e_1 & e_2 & e_3 \end{bmatrix}. \tag{8.88}$$

This leads to a transformation operator **T**:

$$\mathbf{T} = \mathbf{R}\mathbf{c}\mathbf{R}^T. \tag{8.89}$$

T is useful for transforming uncracked tensors in the global frame to cracked tensors in the same frame. For example, the cracked stress σ_{cg} in terms of the stress σ_g is (subscript c indicates cracked, l local frame, and g global frame):

$$\begin{aligned} \sigma_{cg} &= \mathbf{T}\sigma_g\mathbf{T}^T && (8.90) \\ &= \mathbf{R}\mathbf{c}\mathbf{R}^T\sigma_g\mathbf{R}\mathbf{c}\mathbf{R}^T && (8.91) \\ &= \mathbf{R}\mathbf{c}\sigma_l\mathbf{c}\mathbf{R}^T && (8.92) \\ &= \mathbf{R}\sigma_{cl}\mathbf{R}^T. && (8.93) \end{aligned}$$

When many material points have multiple cracks, the solution becomes difficult to obtain numerically. For this reason, controls are available to limit the number and direction of cracks that are allowed.

8.8.10 Grain Growth

When a polycrystalline material is subject to high temperatures, larger grains tend to grow at the expense of the smaller ones. As a consequence, the latter gradually disappear, thus reducing the total number of grains per unit volume and increasing the average grain size. This phenomenon is known as grain growth. The granular structure of the fuel affects physical processes such as fission gas behavior (see Section 10).

A simple empirical model [38] is implemented in BISON for calculating grain growth in UO_2 fuel. According to this model, the kinetics of grain growth is described by the equation:

$$\frac{dD}{dt} = k\left(\frac{1}{D} - \frac{1}{D_m}\right) \tag{8.94}$$

where D (μm) is the 2-dimensional (linear intercept) average grain diameter, t (h) the time, k (μm^2/h) the rate constant, which is $5.24 \cdot 10^7\, exp(-2.67 \cdot 10^5/(RT))$ for R = 8.314 J/(mol·K), and D_m (μm) is the limiting grain size. The latter is a function of the temperature such that

$$D_m = 2.23 \cdot 10^3\, exp(-7620/T) \tag{8.95}$$

To obtain the 3-dimensional grain diameter, D is multiplied by a factor of 1.56 [39].

8.9 Uranium Metal

8.9.1 Thermal Properties `[ThermalU]`

Thermal conductivity k (W/m-K) of uranium metal is from [40], with F_P as a porosity correction given in 9.1, where it is assumed that $\beta = 2.5$:

$$k = 16.170 \times F_P, \qquad T \leq 255.4 \text{ K} \tag{8.96}$$

$$k = (5.907 \times 10^{-6}T^2 + 1.591 \times 10^{-2}T + 11.712) \times F_P, \qquad T \leq 1173.2 \text{ K} \tag{8.97}$$

$$k = 38.508 \times F_P, \qquad T > 1173.2 \text{ K} \tag{8.98}$$

Specific heat C_p (J/mol-K) of U metal is from [40]:

$$C_p = 27.699, \qquad T \leq 298 \text{ K} \tag{8.99}$$

$$C_p = (2.370 \times 10^{-5}T^2 + 2.132 \times 10^{-3}T + 24.959), \qquad T \leq 942 \text{ K} \tag{8.100}$$

$$C_p = 42.928, \qquad T \leq 1049 \text{ K} \tag{8.101}$$

$$C_p = 38.284, \qquad T \leq 1408 \text{ K} \tag{8.102}$$

$$C_p = 48.668, \qquad T > 1408 \text{ K} \tag{8.103}$$

The specific heat is converted to J/kg-K by dividing by 0.238 kg/mol.

8.10 U-10Mo

8.10.1 Thermal Properties `[ThermalU10Mo]`

Low enriched uranium alloyed with 10 wt% (nominally) molybdenum is herein referred to as U-10Mo. Thermal conductivity k (W/m-K) of U-10Mo is from [41], with F_P as a porosity correction given in 9.1, where it is assumed that $\beta = 2.5$:

$$k = (0.606 + 0.0351T) \times F_p \tag{8.104}$$

Specific heat C_p (J/kg-K) of U-10Mo is from [41]:

$$C_p = 113 + 0.0705T \tag{8.105}$$

8.11 U_3Si_2

8.11.1 Thermal Properties `[ThermalU3Si2]`

Using experimental data from figure 4 of [42], a conservative expression for thermal conductivity k (W/m-K) of arc cast U_3Si_2 pellets is obtained:

$$k = 7.98 + 0.0051 \times (T - 273.15) \tag{8.106}$$

where T is temperature in K. This expression is valid for temperatures from room temperature to 1473.15 K. This expression may underestimate the true thermal conductivity of U_3Si_2.

An alternate thermal conductivity model is available by using the `[ThermalU3Si2_P]` material. Here the thermal conductivity k (W/m-K) is expressed by [43]:

$$k = 2.16 + 0.0183T \tag{8.107}$$

with the temperature range of fitted data from 300K to 900K.

Specific heat C_p (J/kg-K) of U_3Si_2 is taken from [44]:

$$C_p = 199 + 0.104 \times (T - 237.15) \tag{8.108}$$

where T is temperature in K. The reference does not state the validity range of this expression.

8.11.2 Volumetric Swelling `[VSwellingU3Si2]`

Because data for U_3Si_2 is limited, a cumulative burnup swelling model is suggested. An empirical expression for the swelling of U_3Si_2 was determined using data from figure 3 of [45]. The swelling of fuel particles was calculated by Finlay using the results of miniplate irradiation tests. To convert Finlay's data (fission density) to FIMA, a value of 10.735 g/cm^3 was used as the heavy metal density, equivalent to 95% theoretical heavy metal density. Based on Finlay's data the incremental strain can be written as a function of burnup:

$$\frac{dV}{d\mathrm{Bu}} = 7.76016 \times \mathrm{Bu} + 0.79811, \tag{8.109}$$

where dV is the incremental strain for a given burnup step and Bu is the instantaneous burnup in FIMA. The volumetric swelling, is calculated by integrating the incremental strain over burnup.

U_3Si_2 is expected to experience densification similar to UO_2. Thus, the fuel densification can be calculated using the ESCORE empirical model [31] given by:

$$\varepsilon_D = \Delta\rho_0 \left(e^{\left(\frac{Bu\, ln(0.01)}{C_D Bu_D} \right)} - 1 \right) \tag{8.110}$$

where ε_D is the densification strain, $\Delta\rho_0$ is the total densification that can occur (given as a fraction of theoretical density), Bu is the burnup, and Bu_D is the burnup at which densification is complete. For temperatures below 750 °C the parameter C_D is given by $7.2 - 0.0086(T - 25)$; above 750 °C it is 1.0 (T in °C).

8.12 Zircaloy

8.12.1 Irradiation Creep `[ThermalIrradiationCreepZr4]`

Irradiation-induced creep of cladding materials is based on an empirical model developed by Hoppe [46] that relates the creep rate to the current fast neutron flux and stress. The specific relation implemented is:

$$\dot{\varepsilon}_{ir} = C_0 \Phi^{C_1} {\sigma_m}^{C_2} \tag{8.111}$$

where $\dot{\varepsilon}_{ir}$ is the effective irradiation creep rate (1/s), Φ is the fast neutron flux (n/m^2-s), σ_m is the effective (Mises) stress (MPa), and C_0, C_1, and C_2 are material constants. Note that the original Hoppe formulation is given in terms of circumferential stress, whereas the relation implemented in BISON assumes an effective (Mises) stress.

8.12.2 Thermal Creep

Two thermal creep models are available. The Hayes model describes only secondary creep while the Limback model includes both primary and secondary creep.

8.12.2.1 Hayes Secondary Creep `[ThermalIrradiationCreepZr4]`

Secondary thermal creep of zirconium alloys was thoroughly investigated by Hayes and Kassner [47] and found to be well-described by a traditional power-law creep formulation. The specific equation recommended there and implemented in BISON is

$$\dot{\varepsilon}_{ss} = A_0 \left(\frac{\sigma_m}{G} \right)^n e^{\left(\frac{-Q}{RT} \right)} \tag{8.112}$$

where $\dot{\varepsilon}_{ss}$ is the effective thermal creep rate (1/s), σ_m is the effective (Mises) stress (Pa), Q is the activation energy (J/mol), R is the universal gas constant (J/mol-K), T is the temperature (K), G is the shear modulus (Pa), and A_0 and n are material constants. For Zr-4, Moon et al. [48] recommend a temperature dependent shear modulus given by $G = 4.2519 \times 10^{10} - 2.2185 \times 10^7 T$ and Hayes and Kassner [47] specify a creep law power (n) of 5. A value for A_0 is not reported in [47]; however, based on experimental data presented there, an approximate value of $A_0 = 3.14 \times 10^{24}$ (1/s) was computed.

8.12.2.2 Limbäck Primary and Secondary Creep `[MechZry]` `[MechZryModel]`

The creep model proposed by Limbäck [49] includes an expression for primary creep. This can be important as part of power changes when the load on the cladding changes relatively suddenly.

Thermal creep in the Limbäck model is given as the Matsuo model [50] where the creep rate (hr^{-1}) is

$$\dot{\varepsilon}_{th} = A \frac{E}{T} \left(\sinh \frac{a_i \sigma_{eff}}{E} \right)^n e^{-Q/RT} \tag{8.113}$$

$$a_i = a \left[1 - A_1 \left(1 - e^{\left(-A_2 \Phi^{A_3} \right)} \right) \right] \tag{8.114}$$

$$E = 1.148 \times 10^5 - 59.9T \tag{8.115}$$

with $A = 1.08 \times 10^9$ (K/MPa/hr), T as temperature (K), $Q = 201$ (kJ/mol), $a = 650$ (dimensionless), $R = 8.314$ (J/mol/K), $N = 2$ (dimensionless), $a = 650$ (dimensionless), $A_1 = 0.56$ (dimensionless), $A_2 = 1.4 \times 10^{-27}$ ((n/cm^2)$^{-A_3}$), and $A_3 = 1.3$ (dimensionless).

Irradiation-induced creep in the Limbäck model is of the form given in Eq. 8.111. The secondary creep rate is then

$$\dot{\varepsilon}_s = \dot{\varepsilon}_{th} + \dot{\varepsilon}_{ir}. \tag{8.116}$$

Primary creep is defined as

$$\varepsilon_p = \varepsilon_p^s \left(1 - e^{\left(-C\sqrt{\dot{\varepsilon}_s t} \right)} \right) \tag{8.117}$$

$$\varepsilon_p^s = B \dot{\varepsilon}_s^b \left[2 - \tanh(D\dot{\varepsilon}_s) \right]^d \tag{8.118}$$

where $C = 52$ (dimensionless), $B = 0.0216$ (hr^b), $b = 0.109$ (dimensionless), $D = 35500$ (hr), and $d = -2.05$ (dimensionless).

Total creep strain is the combination of the primary and secondary creep:

$$\varepsilon_c = \varepsilon_p^s \left(1 - e^{(-C\sqrt{\dot{\varepsilon}_s t})}\right) + \dot{\varepsilon}_s t. \tag{8.119}$$

8.12.2.3 High Temperature Creep (LOCA) `[MechZryModel]`

For simulating a loss of coolant accident, or LOCA, another effective creep strain rate is available for the cladding. An article written by Van Uffelen [51] was used as the primary reference for this LOCA creep model and contains many more articles regarding creep. The equation used is known as the Norton power equation:

$$\dot{\varepsilon} = A \cdot e^{(\frac{-Q}{R \cdot T} + B(x))} \cdot \bar{\sigma}^n, \tag{8.120}$$

where $\dot{\varepsilon}$ is the effective creep strain rate, A is the strength coefficient, Q is the activation energy for plasticity, R is the universal gas constant, T is the temperature, $B(x)$ is a function that represents the oxygen weight concentration of the cladding, $\bar{\sigma}$ is the effective stress, and n is the stress component. The function $B(x)$ is currently assumed to be zero. As the temperature of the clad increases, the Zr alloy undergoes a crystal phase transformation from hexagonal to cubic, referred to as α and β phases respectively. When the phase transition occurs, the coefficients change in value as a function of the fraction of β phase. The range of these values is shown in Table 8.2.

Table 8.2: LOCA Creep Coefficients as a Function of Phase

Phase	Temperature(K)	$A(\mathrm{MPa}^{-n}\mathrm{s}^{-1})$	Q(J/mol)	n
α	900-1085	1.94×10^5	320,000	5.89
β	1248-1873	7.9	142,000	3.79

The fraction of β phase calculation is documented in Section 8.12.6. The coefficient equations are:

$$\ln(A_{\alpha\beta}) = (1-\phi)\cdot\ln(A_\alpha) + \phi\cdot\ln(A_\beta) \tag{8.121}$$

$$Q_{\alpha\beta} = (1-\phi)\cdot Q_\alpha + \phi\cdot Q_\beta \tag{8.122}$$

$$n_{\alpha\beta} = (1-\phi)\cdot n_\alpha + \phi\cdot n_\beta \tag{8.123}$$

Where ϕ is the fraction of β phase and varies from 0 to 1. So, given the fraction of β phase, which is a function of time and temperature, one can calculate the effective creep rate during LOCA conditions.

When running a simulation where the temperature in the cladding increases from normal operating conditions (˜600K) up to LOCA temperatures (˜900K), the effective creep strain rate is linearly interpolated between the Matsuo model [50] and the LOCA model. There are a number of regression tests that demonstrate the LOCA behavior and the transition between normal operation secondary thermal creep and LOCA creep.

8.12.3 Combined Creep and Instantaneous Plasticity `[ThermalIrradiationCreepPlasZr4]` `[MechZryModel]`

Material models are also available for combined instantaneous plasticity and time-dependent creep. Creep is modeled using the irradiation and thermal creep constitutive equations described above. Time-independent plasticity is modeled assuming J2 plasticity based on a simple linear strain hardening curve. For each stress update, the model first consideres only the creep contribution to compute a new stress, which is then compared to the yield strength. If above yield, instantaneous plasticity is applied to reduce the stress onto the yield curve. Iteration is employed to insure stress convergence.

8.12.4 Irradiation Growth `[IrradiationGrowthZr4]`

A model for irradiation growth of Zr4 cladding is available. It is taken from the ESCORE model (see [31], Volume 1: Theoretical and Numerical Bases, section 5.3.4). The axial strain is given as

$$\varepsilon = A(\phi t)^n \tag{8.124}$$

where A and n are constants and ϕt is fast neutron fluence. The value for A is 3×10^{-20} N/cm^2. The value for n is 0.794. We generate a strain increment for the irradiation growth as

$$\Delta\varepsilon = A\left((\phi t_i)^n - (\phi t_{i-1})^n\right) \tag{8.125}$$

with i representing the current step number.

Since irradiation growth should occur in the axial direction only while being volume conserving, it is necessary to specify a strain increment for the other two directions. This is given by

$$\Delta\varepsilon_{lateral} = -(1-(1+\Delta\varepsilon)^{-0.5}) \tag{8.126}$$

8.12.5 Damage `[CumulativeDamageIndex]`

Intergranular stress corrosion cracking, typically caused by pellet-clad interaction (PCI), can lead to clad failure during normal operation. A cumulative damage model by Rashid [52] is used in BISON to estimate clading damage for low temperature steady-state conditions. The model is based on the notion of a cumulative damage index, which has the following form.

$$D = \int_0^{t_n} \frac{dt}{t_f(\sigma_{\mathrm{hoop}}, B, T)} \tag{8.127}$$

In Eq.8.127, D is the amount of damage at time t_n (all time in seconds), t_f is the failure time at stress σ_{hoop} (all stress in units of MPa), T is temperature (K), and B is burnup (MWd/MTU). The variable t_f has the form:

$$t_f = \bar{t}\; exp[(1.015\sigma_y + 1.74\sigma_{\mathrm{ref}} - 2.755\sigma_{\mathrm{hoop}})0.01] \tag{8.128}$$

where σ_y is the clad yield stress, and

$$\bar{t} = 5 \times 10^5(1.13 \times 10^{-4}B - 0.13)^{-0.75} exp[-30(1-611/T)] \tag{8.129}$$

where the stress σ_{ref} is a threshold stress, which has the form:

$$\sigma_{\text{ref}} = \begin{cases} 336.476(B-5000)^{-0.07262} & \text{for Zr2} \\ 310.275(B-5000)^{-0.0440} & \text{for Zr4.} \end{cases} \tag{8.130}$$

The model for cumulative damage index (Eq.8.127) activates only when $\sigma_{\text{hoop}} > \sigma_{\text{ref}}$ and $B > 5000$ MWd/MTU.

8.12.6 Phase transformation `[ZrPhase]`

Under extreme in-service conditions, e.g., during a postulated loss-of-coolant accident (LOCA), fuel cladding will be subjected to a rapid increase in temperature (up to 1000-1500K), which involves time-dependent phase transformation of Zr alloy from hexagonal (α-phase) to cubic (β-phase) crystal structure. Modeling the kinetics of crystallographic phase transformation is pivotal for the assessment of the mechanical properties essential for fuel rod integrity (deformation and burst) during a postulated LOCA.

The crucial parameter for the transformation kinetics is the evolution of the volume fraction of the new phase as a function of time and temperature. A model is available in BISON for calculation of the volume fraction of the favoured phase in Zircaloy-4 as a function of time and temperature during phase transformation in non-isothermal conditions. The model is based on [53, 54, 55]. The phase transformation rate is expressed by

$$\frac{dy}{dt} = k(T)\left[y_s(T) - y\right] \tag{8.131}$$

where y is the volume fraction of β-phase, t (s) the time, y_s (/) the steady-state or equilibrium value of y, and k (s^{-1}) the rate parameter. The β-phase equilibrium fraction is represented by a sigmoid function of temperature

$$y_s = \frac{1}{2}\left[1 + tanh\left(\frac{T - T_{cent}}{T_{span}}\right)\right] \tag{8.132}$$

where T_{cent} and T_{span} are material specific parameters related to the center and span of the mixed-phase temperature region, respectively. For Zircaloy-4, $T_{cent} = 1159 - 0.096w$ (K) and $T_{span} = 44 + 0.026w$ (K) [53] are used, with w being the hydrogen concentration in the range $0 \leq w \leq 1000$ wppm (weight parts per million hydrogen). The rate parameter is expressed in the form

$$k = k_0 exp\left[-\frac{E}{k_b T(t)}\right] + k_m \tag{8.133}$$

where k_0 is a kinetic prefactor, E an effective activation energy, k_b the Boltzmann constant, and k_m a constant. For Zircaloy-4, $k_0 = 60457 + 18129|Q|$ (s^{-1}) and $E/k_b = 16650$ (K) [53, 55] are used, where $Q = dT/dt$ (Ks^{-1}) is the heat rate in the range $0.1 \leq |Q| \leq 100$ Ks^{-1}. The $\alpha \to \beta$ transformation is purely diffusion controlled, while the $\beta \to \alpha$ transformation is partly martensitic. This is represented by the constant k_m given in the form [55]

$$\begin{cases} k_m = 0 & \alpha \to \beta \\ k_m = 0.2 & \beta \to \alpha \end{cases} \tag{8.134}$$

The starting temperatures for the onset of $\alpha \rightarrow \alpha + \beta$ and $\beta \rightarrow \alpha + \beta$ phase transformations are calculated as (in kelvin) [53]

$$T_{\alpha\rightarrow\alpha+\beta} = \begin{cases} 1083 - 0.152w & \text{for } 0 \leq Q < 0.1 \text{ Ks}^{-1} \\ (1113 - 0.156w)\,Q^{0.0118} & \text{for } 0.1 \leq Q \leq 100 \text{ Ks}^{-1} \end{cases} \tag{8.135}$$

$$T_{\beta\rightarrow\alpha+\beta} = \begin{cases} 1300 & \text{for } -0.1 < Q \leq 0 \text{ Ks}^{-1} \\ 1302.8 - 8.333\,|Q|^{0.477} & \text{for } -100 \leq Q \leq -0.1 \text{ Ks}^{-1} \end{cases} \tag{8.136}$$

for $0 \leq w \leq 1000$ wppm.

The β-phase volume fraction as a function of time is calculated by numerical integration of Eq. (8.131). As default option, this is accomplished using the second order Adams-Moulton (AM2) method. The backward Euler method is also available.

8.12.7 Hydride formation `[HydridePrecipitationRate]`

In normal service, waterside oxidation of Zircalloy fuel cladding introduces hydrogen into the cladding. Where the dissolved hydrogen concentration is high enough or the temperature is low enough, zirconium hydride precipitates, forming thin platelets. The orientation of these hydrides depends on the local stress state when they are formed. Immediately after fuel rod removal, the platelets typically are oriented in circumferential rings. However, during later drying stages, the cladding material may heat up enough to re-dissolve the hydrides. Subsequent cooling of the rod at atmospheric pressure causes the hydrides to re-precipitate into radially-oriented crystals which form paths for radial crack formation. Predicting the potential for cracking therefore requires accurate modeling of the time evolution of the hydride concentration throughout the life of the fuel rod. Models for the spatial-temporal distribution of the dissolved and precipitated hydrogen are included in BISON and are discussed below; modeling the orientation of the hydride platelets is in progress in MARMOT.

Hydrogen in solid solution in zirconium will precipitate to form zirconium hydrides as the temperature of the sample is decreased. If the sample is then re-heated, dissolution will begin at a higher temperature than was required for precipitation. This hysteresis effect is due to a volumetric strain caused by mismatch of the density of the hydrides and the surrounding zirconium matrix. Thus, there are two solubility curves, denoted TSS_p for precipitation and TSS_d for dissolution. In BISON, we use the following fits from McMinn:

$$TSS_d = 106447 e^{-4329/T} \tag{8.137}$$

$$TSS_p = 138746 e^{-4146/T} \tag{8.138}$$

In addition to the hysteresis effect, precipitation of hydrides is a non-equilibrium phenomenon at the time scales of interest. Attempts to model the hydride precipitation as an equilibrium process fail to predict the ingress of hydrogen into the cladding from the oxide interface. The ingress into the cold side of the cladding can only be predicted if the precipitation rate S is slow enough to allow a flux of hydrogen into the cladding from the oxide. The rate of precipitation is usually modeled as a simple kinetic rate

$$S = K_p(C_{ss} - TSS_p) \tag{8.139}$$

If the rate of growth of the hydrides is diffusion-limited, the rate coefficient K_p should follow an Arrhenius relation with activation energy similar to the diffusivity D of hydrogen in solid solution. Various fits for K_p have been published, but experiments have mostly failed to find a consistent temperature dependence. Nevertheless, an Arrhenius rate has been useful to model the effects of hydride rim formation in BISON because it gives good results near the cold boundary. The rate has an activation energy similar to that for diffusion and has been fitted to match reasonably well with rate measurements around 550-600 K:

$$S \approx 4.4e^{-4\cdot 10^4/RT} \tag{8.140}$$

The Arrhenius rate works well for most of the domain, but additional physics are needed to explain why the hydride concentration in the rim is only about 10-20% by volume. For now, we use a clamping function that sets $K_p = 0$ when the hydride concentration passes a user-specified value C_{clamp}.

Dissolution is also assumed to have a simple kinetic form where the driving force is due to undersaturation of hydrogen in solution:

$$S = K_d(C_{ss} - TSS_d) \tag{8.141}$$

Note that S is negative for dissolution. The dissolution rate coefficient K_d is usually assumed to be much larger than the rate of precipitation and to our knowledge has not been measured. Therefore, we use a phenomenological form in BISON, where K_d is assumed to depend on the undersaturation of C_{ss} and on the available surface area of hydride (using C_p as a very rough proxy for surface area):

$$K_d = K_p C_p \tag{8.142}$$

For a typical hydride concentration around 100 ppm, K_d will be two orders of magnitude larger than K_p. In addition,

$$\lim_{C_p \to 0} K_d = 0 \tag{8.143}$$

leading to much better-behaved numerical integration than if we were to set $K_d = \alpha K_p$ with α some constant value.

Hydrogen in solid solution in zirconium diffuses down both mass and temperature gradients via Fick's Law and the Soret effect. The mass flux J is

$$J = D\left(\nabla C_{ss} + \frac{C_{ss}Q^*}{RT^2}\nabla T\right) \tag{8.144}$$

where C_{ss} is the concentration of hydrogen in solid solution, D is the mass diffusivity, and Q^* is the heat of transport for hydrogen in zirconium. Note that the diffusivity of hydrogen in hydrides has been measured to be at least 3 times smaller than the diffusivity of hydrogen in zirconium so we assume that the hydrogen is immobile once it has precipitated.

Combining the flux with the precipitation rate S, we obtain the evolution equation for hydrogen in solid solution

$$\frac{\partial C_{ss}}{\partial t} = \nabla \cdot D\left(\nabla C_{ss} + \frac{C_{ss}Q^*}{RT^2}\nabla T\right) - S \tag{8.145}$$

$$S = \begin{cases} 4.4e^{-4\cdot 10^4/RT}(C_{ss} - TSS_p) & \text{for } C_{ss} > TSS_p \text{ and } C_p < C_{\text{clamp}} \\ 4.4e^{-4\cdot 10^4/RT}C_p(C_{ss} - TSS_d) & \text{for } C_{ss} < TSS_d \\ 0 & \text{everywhere else} \end{cases} \tag{8.146}$$

9 General Material Models

9.1 Thermal Conductivity Porosity Model

A common approach to correct thermal conductivity for fission gas porosity is given by [56]:

$$F_P = (1-P)/(1+\beta P) \tag{9.1}$$

where β is an empirical factor and P is the fission-gas porosity fraction.

9.2 Mass Diffusion Coefficients `[ArrheniusMaterialProperty]` `[ArrheniusDiffusionCoef]`

Mass diffusion coefficients are defined using an Arrhenius form [57]

$$D(T) = \sum_i D_{0,i} \exp\left(\frac{-Q_i}{RT}\right) \tag{9.2}$$

where $D_{0,i}$ is a pre-exponential factor, Q_i is the activation energy, R is the universal gas constant and T is temperature.

10 Fission Gas Behavior

The processes induced by the generation of the fission gases xenon and krypton in nuclear fuel have a strong impact on the thermo-mechanical performance of the fuel rods. On the one hand, the fission gases tend to precipitate into bubbles resulting in fuel swelling, which promotes pellet-cladding gap closure and the ensuing pellet-cladding mechanical interaction (PCMI). On the other hand, fission gas release (FGR) to the fuel rod free volume causes pressure build-up and thermal conductivity degradation of the rod filling gas.

The fundamental physical processes, which control the kinetics of fission gas swelling and release in irradiated UO_2 fuel, may be summarised as follows. Fission gas atoms generated in the fuel grains diffuse towards the grain boundaries through repeated trapping in and irradiation-induced resolution from nanometre-size intra-granular gas bubbles. Although a part of the gas atoms that reach the grain boundaries is dissolved back to the grain interior by irradiation, the majority of the gas diffuses into grain-face gas bubbles, giving rise to grain-face swelling. Bubble growth brings about bubble coalescence and inter-connection, eventually leading to the formation of a tunnel network through which a fraction of the gas is released to the fuel rod free volume.

In BISON, fission gas behavior is computed for each integration point in the fuel finite element mesh. The gas produced at each integration point is computed by a numerical time integration of the gas production rate, given as the product of the fission rate and fractional yield of gas atoms per fission.

The Sifgrs model is recommended.

10.1 Simple Physics-Based Model `[Sifgrs]`

The Simple Integrated Fission Gas Release and Swelling (Sifgrs) model is intended for consistently evaluating the kinetics of both fission gas swelling and release in UO_2. The model incorporates the fundamental features of fission gas behavior, among which are gas diffusion and precipitation in grains, growth and coalescence of gas bubbles at grain faces, thermal, athermal, steady-state, and transient gas release. Through a direct description of the grain-face gas bubble development, the fission gas swelling and release are calculated as inherently coupled processes, on a physical basis. The level of complexity of the model is consistent with reasonable computational cost and the uncertainties inherent in engineering-scale fuel analysis. The Sifgrs model draws on and extends the approach described in [58].

10.1.1 Intra-granular gas behavior

Fission gas transport from within the fuel grains to the grain faces is computed through numerical solution of the relevant diffusion equation in one-dimensional spherical geometry

$$\frac{\partial C_t}{\partial t} = D_{eff} \frac{1}{r^2} \frac{\partial}{\partial r} \left(r^2 \frac{\partial C_t}{\partial r} \right) + \beta \tag{10.1}$$

where C_t (m^{-3}) is the intra-granular gas concentration, t (s) the time, D_{eff} ($\mathrm{m}^2\mathrm{s}^{-1}$) the effective gas diffusion coefficient, r (m) the radial co-ordinate in the spherical grain, and β ($\mathrm{m}^{-3}\mathrm{s}^{-1}$) the gas generation rate. The effective diffusion coefficient, which accounts for the effects of repeated trapping in and irradiation-induced resolution from intra-granular bubbles, is calculated based on [59, 60].

Moreover, an empirical contribution to gas transport from within the grains to the grain faces is considered during power ramps, aimed at representing the rapid increase of FGR observed under these conditions. In particular, the simple empirical ramp release model of Koo et al. [61] is adopted. According to this model, during a rapid power increase an additional fraction of the intra-granular gas is transferred to the grain faces, which depends on local temperature, linear power and linear power change during the transient.

The contribution of intra-granular bubbles to fission gas swelling (intra-granular swelling), which is generally less important than the swelling due to grain-face bubbles (at least for burnup below about 45 GWd/t [62]), is presently not considered in the model.

10.1.2 Grain-face gas behavior

Numerical solution of Eq. 10.1 allows estimating the arrival rate of gas at the grain faces, thus providing the source term for the grain-face gas behavior module. The latter computes both the fission gas swelling and release through a direct description of the grain-face bubble development, including bubble growth and coalescence (which are reflected in fuel swelling), and eventual inter-connection (leading to thermal FGR). In outline:

- Peculiarities related to the presence of grain edges (where three grains meet) are neglected (e.g., [63, 64]).
- The flux of gas atoms dissolved from the grain faces back to the grain interior by irradiation is neglected [65].
- An initial number density of grain-face bubbles (nucleation centers) is considered, and further nucleation during the irradiation is neglected (one-off nucleation, e.g., [66]).
- The absorption rate of gas at the grain-face bubbles is assumed to equal the arrival rate of gas at the grain faces [66, 67].
- All grain-face bubbles are considered to have, at any instant, equal size and equal lenticular shape of circular projection (e.g., [68]). Hence, the fractional volume grain-face fission gas swelling is given by

$$\left(\frac{\Delta V}{V} \right) = \frac{1}{2} \frac{N_{gf}}{(1/3) r_{gr}} \left(\frac{4}{3} \pi \varphi(\Theta) R_{gf}^3 \right) \tag{10.2}$$

where N_{gf} is the number density of grain-face bubbles per unit surface, r_{gr} the grain radius, Θ the bubble semi-dihedral angle, $\varphi(\Theta)$ the geometric factor relating the volume of a lenticular-shape bubble to that of a sphere, which is $1-1.5\cos(\Theta)+0.5\cos^3(\Theta)$, and R_{gf} the bubble radius of curvature. The factor 1/2 is introduced in Eq. 10.2 because a grain-face bubble is shared by two neighboring grains.

- Bubble growth is treated using the model of Speight and Beere [69], which describes the growth (or shrinkage) of grain-face bubbles as proceeding by absorption (or emission) of vacancies in grain boundaries, induced by the difference between the pressure of the gas in the bubble, p (Pa), and the mechanical equilibrium pressure, p_{eq} (Pa). The vacancy absorption/emission rate at a bubble is given by

$$\frac{dn_v}{dt} = \frac{(2\pi D_v \delta_g)}{kTS}\,(p-p_{eq}) \tag{10.3}$$

where n_v (-) is the number of vacancies in the bubble, D_v ($m^2\cdot s^{-1}$) the vacancy diffusion coefficient in grain boundaries, δ_g (m) the thickness of the diffusion layer in grain boundaries, and the parameter S (-) may be calculated as [66]

$$S = -\frac{1}{4}\left[(3-F_c)\cdot(1-F_c)+2ln\,(F_c)\right] \tag{10.4}$$

with F_c being the fraction of grain faces covered by bubbles (fractional coverage). The mechanical equilibrium pressure, p_{eq}, of the gas in a lenticular bubble of circular projection is given by

$$p_{eq} = \frac{2\gamma}{R_{gf}} - \sigma_h \tag{10.5}$$

where γ ($J\cdot m^-2$) is the UO_2/gas specific surface energy, R_{gf} (m) the bubble radius of curvature, and σ_h (Pa) the hydrostatic stress (considered to be negative if the solid medium is under compression). For describing the bubble thermodynamic state, the Van der Waals' equation of state is adopted in the following form:

$$p\,(V_{gf}-n_g\omega) = n_g kT \tag{10.6}$$

where n_g (-) is the number of fission gas atoms per bubble, k [$J\cdot K^{-1}$] the Boltzmann constant, T (K) the temperature, V_{gf} (m^3) the bubble volume, and ω (m^3) the Van der Waals' volume of a fission gas atom. Given that each bubble consists of vacancies and gas atoms, the volume of a bubble comprising n_g fission gas atoms and n_v vacancies is given by

$$V_{gf} = n_g\omega + n_v\Omega_{gf} \tag{10.7}$$

where Ω_{gf} (m^3) is the atomic (vacancy) volume in the bubble. Combination of Eqs. 10.6 and 10.7 gives for the pressure of the gas in the bubble

$$p = \frac{kT}{\Omega_{gf}} \frac{n_g}{n_v} \tag{10.8}$$

The above approach allows computing the bubble growth rate from the rate of inflow of gas atoms along with the rate of absorption (emission) of vacancies at the bubble. The combined effects of gas atom inflow and vacancy absorption (emission) are interactive, since the addition of fission gas atoms gives rise to a change in the bubble pressure via Eq. 10.8, which affects the propensity of the bubble to absorb (or emit) vacancies through Eq. 10.3. Given the volume, V_{gf}, of a lenticular bubble of circular projection, the bubble radius of curvature is calculated as

$$R_{gf} = \left(\frac{3V_{gf}}{4\pi\varphi(\Theta)} \right)^{\frac{1}{3}} \tag{10.9}$$

- The process of grain-face bubble coalescence, which leads to a progressive decrease of the bubble number density throughout irradiation, is described using an improved model of White [58, 66]. According to this model, the rate of loss of bubbles by coalescence is given by

$$\frac{dN_{gf}}{dt} = -\frac{6N_{gf}^2}{3 + 4N_{gf}A_{gf}} \frac{dA_{gf}}{dt} \tag{10.10}$$

  where N_{gf} and A_{gf} represent the number density and projected area of grain-face bubbles, respectively.

- The release of fission gas to the fuel rod free volume following inter-connection of grain-face bubbles and consequent formation of pathways for gas venting to the fuel exterior (thermal release) is modeled based on a principle of grain face saturation. More specifically, a saturation coverage concept is adopted, namely, it is considered that once the fractional coverage, F, attains a saturation value, F_{sat}, the bubble number density and projected area obey the saturation coverage condition

$$F = N_{gf}A_{gf} = F_{sat} \tag{10.11}$$

  where N_{gf} is the bubble number density and $A_{gf} = \pi(\sin(\Theta))^2 R_{gf}^2$ is the bubble projected area on the grain face. The commonly accepted value for F_{sat} is 0.5. Eq. 10.11 implies that, after attainment of the saturation coverage, a fraction of the gas reaching the grain faces is released to the fuel exterior to compensate for continuing bubble growth.

10.1.3 Transient gas behavior

Experimental observations relative to both in-reactor irradiation and post-irradiation annealing of oxide nuclear fuel indicate that substantial fission gas release can occur on a small time scale during temperature transients (burst release). The rapid kinetics of the process cannot be interpreted as purely diffusion-controlled. From the available experimental evidence (e.g., [70, 71, 72, 73]), the following main aspects of transient fission gas behaviour emerge:

- Burst release occurs through grain-face separation (micro-cracking) which entails gas depletion of a fraction of the grain faces.
- Release bursts are triggered by temperature variations, both heating and cooling.
- The rate of gas release during bursts is a peaked function of temperature with the maximum at a 'central' temperature of approximately 1500 C (1773 K).

An extension (transient model) of the treatment of grain-face gas behavior described in Section 10.1.2 is available in BISON, which introduces the effect of micro-cracking on fission gas behavior [74]. According to the BISON transient model, gas depletion of a fraction of the grain faces is modeled as a reduction of the fractional coverage, F. In particular, F is scaled by a factor, f, corresponding to the fraction of non-cracked (intact) grain faces. The reduction of the fractional coverage effectively leads to a decrease of the amount of gas retained in the fuel – consequently, of fission gas swelling – and to a corresponding increase of FGR. This contribution to thermal FGR supplements the diffusion-interconnection mechanism considered in the basic model (Section 10.1.2). Also, the lost gas storing capacity of cracked grain faces is represented by scaling the saturation coverage, F_{sat}, by the factor f. Moreover, the healing process of cracked grain faces is considered as a progressive restoration of the grain-face gas storing capacity. Therefore, the fractional coverage and saturation coverage obey

$$\frac{dF}{dt} = \left[\frac{dF}{dt}\right]_d + F\left[\frac{df}{dt}\right]_c \tag{10.12}$$

$$\frac{dF_{sat}}{dt} = F_{sat}\left(\left[\frac{df}{dt}\right]_c + \left[\frac{df}{dt}\right]_h\right) \tag{10.13}$$

where d stands for diffusion-controlled processes (basic model, Section 10.1.2), c stands for micro-cracking, and h for micro-crack healing. The value for the maximum (initial) saturation coverage (corresponding to all intact grain faces) is $F_{sat,i} = 0.5$. The calculation of the term representing the effects of micro-cracking is detailed hereinafter.

We simplify the micro-cracking process into a purely temperature-dependent behaviour, characterized by a micro-cracking parameter, m. We also observe that the process can only affect intact grain faces, and write

$$\left[\frac{df}{dt}\right]_c = -\frac{dm}{dt}f \tag{10.14}$$

where $\left[df/dt\right]_c$ is the reduction rate due to micro-cracking of the fraction of intact grain faces, f. The micro-cracking parameter is taken as a function of the sole temperature, hence

$$m(T,t) = m(T(t)) \tag{10.15}$$

Then, Eq. 10.14 can be written as

$$\left[\frac{df}{dt}\right]_c = -\frac{dm}{dT}\frac{dT}{dt}f \tag{10.16}$$

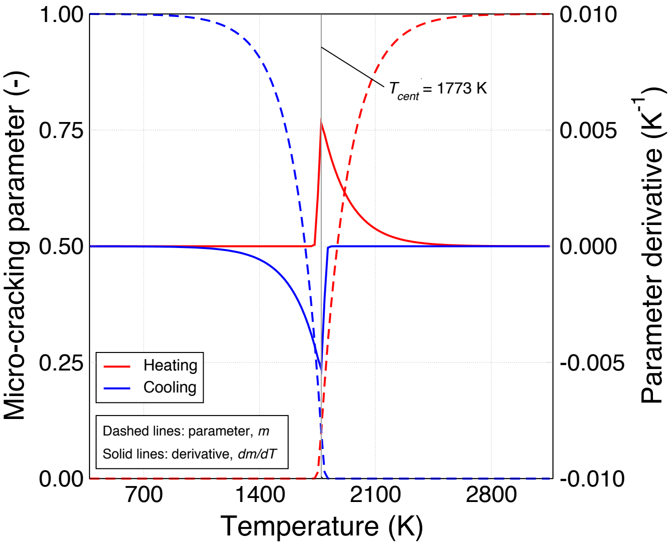

Figure 10.1: Micro-cracking parameter, m, and derivative, dm/dT, as a function of temperature.

implying

$$\left[\frac{df}{dt}\right]_c = 0 \quad if \ \frac{dT}{dt} = 0 \tag{10.17}$$

which conforms to the experimentally observed characteristic of burst release as triggered by temperature variations. Under the condition expressed by Eq. 10.15, the analytic solution of Eq. 10.14 with initial conditions $f(t_0) = f_0$ and $m(T(t_0)) = m_0$ is

$$f(t) = f_0 \, exp\left[-\left(m(T(t)) - m_0\right)\right] \tag{10.18}$$

Based on the available experimental evidence, the functional form of m is chosen as a temperature-dependent sigmoid function

$$m(T) = 1 - \left[1 + Q \, exp\left(s \frac{T - T_{cent}}{T_{span}}\right)\right]^{-\frac{1}{Q}} \tag{10.19}$$

where T_{cent} (K) is the central temperature, T_{span} (K) is a measure of the temperature-domain width of the phenomenon, Q (-) is a parameter, and s is defined as

$$\begin{cases} s = +1 & if \ dT/dt > 0 \ \text{(heating transients)} \\ s = -1 & if \ dT/dt < 0 \ \text{(cooling transients)} \end{cases} \tag{10.20}$$

so that m increases during both heating and cooling transients. The following values are usedfor the parameters: T_{cent}=1773 K, T_{span}=5 K, Q=33. The micro-cracking parameter, m, and the parameter derivative, $dm// dT$, are plotted in Fig. 10.1.

A simple burnup-dependent model is used for micro-crack healing, which is not described here for brevity. Details can be found in [74]. The above treatment of transient fission gas behavior preserves the continuity in both time and space as well as the consistent coupling of the calculated fission gas release and swelling. Early validation has indicated that the model is capable of consistently representing the kinetics of FGR during transient fuel irradiations [74].

10.1.4 Athermal gas release

At low temperature, the fission gas in the matrix of the solid is relatively immobile. Only the gas formed at the external surface of the solid is capable of escape, with an emission rate that is independent of temperature. This athermal contribution to FGR arises from the surface-fission release mechanisms of recoil (direct release of a fission fragment due to its high kinetic energy) and knockout (ejection of a gas atom following elastic interaction with either a primary fragment or energetic particle created in a collision cascade) [75]. These release mechanisms affect only the outer layer of the fuel (within about 10 µm from the surface). The rate of gas atom release per unit fuel volume due to recoil and knock-out, R_a ($\mathrm{m^{-3}s^{-1}}$), may be calculated as [75]

$$R_a = \frac{yF}{4V}\left(S_g\mu_f + 2S_t\mu_U^{ko}\right) \tag{10.21}$$

where y (/) is the fractional yield of fission gas atoms, F the fission rate density ($\mathrm{m^{-3}s^{-1}}$), V ($\mathrm{m^3}$) the volume of fuel, S_g ($\mathrm{m^2}$) the geometrical surface area of fuel, S_t ($\mathrm{m^2}$) the total surface area of fuel (including cracked surface), μ_f (m) the fission fragment range in the fuel, and μ_U^{ko} (m) the range of the higher order uranium knock-on in UO_2.
In line with [76], the number and length of cracks in each fuel pellet is estimated in a simple way. First, radial cracks are considered to cross the outer, brittle region of the fuel pellet with a temperature lower than 1200 C [77]. Second, the number of pellet cracks is considered to increase linearly with fuel linear power [78]. Then, once the linear power and pellet dimensions are given, the total pellet surface area available for athermal gas release can be calculated.

10.1.5 Grain growth and grain boundary sweeping

Being the fission gas behavior physically dependent on the granular structure of the fuel, the Sifgrs model is coupled with the grain growth model (Section 8.8.10). The grain growth phenomenon affects the fission gas release in three ways. First of all, due to the low solubility of the fission gas, the moving grain boundary does not redeposit any gas in the newly-formed crystal behind it, thus acting as a filter and contributing to the collection of gas at the grain faces (*grain boundary sweeping*). This effect is taken into account in Sifgrs by adding a supplementary fractional release term (s) from within the grains to the grain faces that is equal to the volume fraction of the fuel swept by the moving boundaries:

$$s = \frac{r_i^3 - r_{i-1}^3}{r_i^3} \tag{10.22}$$

where the indices $i-1$ and i refer to the previous and current time, respectively. Secondly, the diffusion distance for the fission gas atoms created in the grains increases as the grains grow. Unlike the first consequence this tends to reduce the release rate. Thirdly, grain growth reduces the capacity of the grain boundaries to store fission gas, as it results in a decrease of the total grain surface-to-volume ratio.

10.2 Modified Forsberg-Massih Model `[ForMas]`

As an additional option, fission gas release (FGR) can be computed based on the traditional Forsberg-Massih model (ForMas) [79]. This model considers FGR only, hence the fission gas swelling must be calculated separately by means of an empirical model (see Section 8.8.4).

ForMas incorporates a two-stage approach to predict gas release. The first stage computes diffusion of fission gas atoms from within the fuel grains to the grain boundaries, by solving numerically the relevant diffusion equation in spherical co-ordinates. An effective diffusion coefficient is employed, which accounts for gas atom resolution from and trapping into intra-granular bubbles. A formulation based on Turnbull et al. [80, 81] is used to calculate the single gas atom diffusion coefficient, and correction for the effects of intra-granular bubbles is modeled based on the correlations reported in [59]. The second stage of the model utilizes time-dependent boundary conditions to determine grain boundary gas accumulation as inter-granular lenticular bubbles, resolution, saturation, and release. FGR from the grain boundaries is controlled using a grain boundary saturation criterion that involves a threshold concentration of gas at the grain boundaries.

For the current implementation, the fuel grains are assumed to be constant in diameter, thus grain growth and grain-boundary sweeping effects are not considered. Further, the model describes a smooth continuous release process, and is thus not applicable to sudden releases or bursts. These are significant limitations, which must be alleviated to provide more realistic FGR predictions. Accordingly, a more mechanistic model is currently being implemented in BISON which considers the structure of both the fuel (fuel grains and pores) and grain boundaries, and includes the effects of grain growth and grain boundary sweeping. This model will be directly coupled to the volumetric swelling calculation, thus replacing the empirical model described in Eq. 8.61.

Following [82], the ForMas model implemented in BISON includes some modifications compared to the original Forsberg-Massih [79] model, namely:

- The following three-term formulation, based on Turnbull et al. [80, 81], is used to calculate the single gas atom diffusion coefficient

  $$\begin{aligned} D_{atomic} &= D_1 + D_2 + D_3 \\ D_1 &= 7.6 \cdot 10^{-10} \cdot exp\left(-\frac{35250}{T}\right) \\ D_2 &= 1.41 \cdot 10^{-25} \sqrt{\dot{F}} \cdot exp\left(-\frac{13800}{T}\right) \cdot 4.0 \\ D_3 &= 2.0 \cdot 10^{-40} \cdot \dot{F} \end{aligned} \tag{10.23}$$

  where T (K) is the temperature and $\dot{F}$ ($\mathrm{m}^{-3} \cdot \mathrm{s}^{-1}$) is the fission rate.

- The rate of gas atom resolution from the grain boundaries back into the grains is scaled by fission rate, in line with [59].
- Instead of assuming release of the total gas inventory at the grain boundaries upon saturation [79], only the gas above the saturation level is considered to be released.

The modified Forsberg-Massih model implemented in BISON was tested using a single LWR fuel pellet, assuming uniform constant power. Typical input parameters for UO_2 fuel, as shown in Table 10.1, were assumed. Calculations were compared to the well known Vitanza or Halden threshold [83], which correlates a large set of FGR data in terms of fuel centerline temperature versus burnup at roughly one percent gas release; this threshold is often used to evaluate and calibrate FGR models. A typical comparison is shown in Figure 10.2, which considers the effect of hydrostatic pressure on the computed gas release. Symbols in the figure indicate individual simulations at various axial power levels. As has been reported earlier [84], an increase in hydrostatic pressure significantly shifts the onset of gas release to higher burnups.

Table 10.1: Input parameters for the modified Forsberg-Massih fission gas release model

Fuel grain radius (m)	1.0×10^{-5}
Frac. yield of fission gas atoms per fission	0.3017
Reference resolution rate of intergranular gas (s^{-1})	1.0×10^{-7}
Resolution layer depth (m)	1.0×10^{-8}
Grain boundary bubble radius (m)	0.5×10^{-6}
Nonspherical bubble shape factor [/]	0.287
Bubble surface tension (J/m^2)	0.626
Grain boundary frac. coverage at saturation [/]	0.5

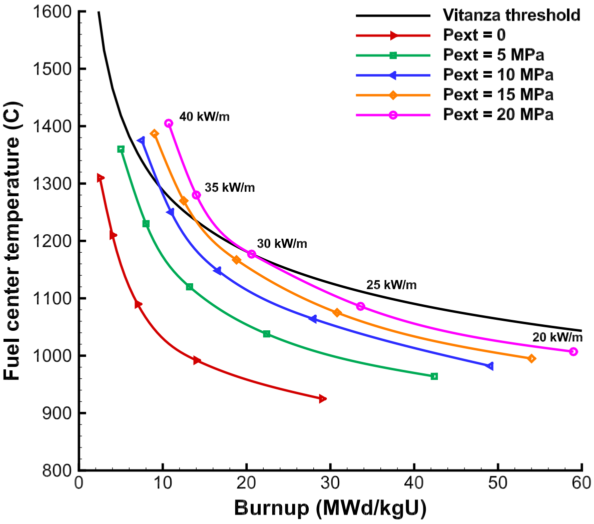

Figure 10.2: Effect of hydrostatic pressure on centerline temperature versus burnup for 1 percent average fission gas release. The Vitanza threshold [83] is included for comparison.

11 Power, Burnup, and Related Models

11.1 Power

The power associated with an LWR fuel rod is typically given as rod averaged linear power (or linear heat rate) in units of W/m. This power varies in time and space. The axial variation in power is given as a scaling factor as a function of distance from the bottom of the rod.

11.1.1 Radial Power Profile

The power density in a fuel pellet varies radially as a function of geometry, initial fuel characteristics, and irradiation history. With increasing burnup, the concentration of Pu toward the outer rim is relatively high, resulting in a local power density that can be 2-3 times that found elsewhere in the pellet. This variation needs to be captured in order to calculate the heat generation and temperature distribution in the pellet accurately.

BISON uses the TUBRNP model of Lassmann ([85]; see also [31]). In this model, the average isotope concentrations are

$$\frac{d\overline{N}_{235}}{dt} = -\sigma_{a,235}\overline{N}_{235}\phi, \tag{11.1a}$$

$$\frac{d\overline{N}_{238}}{dt} = -\sigma_{a,238}\overline{N}_{238}\phi, \tag{11.1b}$$

$$\frac{d\overline{N}_{j}}{dt} = -\sigma_{a,j}\overline{N}_{j}\phi + \sigma_{c,j-1}\overline{N}_{j-1}\phi, \tag{11.1c}$$

where $\overline{N}$ is the number of atoms per unit volume, σ_a is the absorption cross section, σ_c is the capture cross section, ϕ is the neutron flux, and j represents each of the ^{239}Pu, ^{240}Pu, ^{241}Pu, and ^{242}Pu isotopes.

Recognizing the relationship between an increment of fluence ($\phi\Delta t$) and an increment of burnup (Δbu), these equations can be reformed as

$$\frac{d\overline{N}_{235}}{d\mathrm{bu}} = -\sigma_{a,235}\overline{N}_{235}A, \tag{11.2a}$$

$$\frac{d\overline{N}_{238}}{d\mathrm{bu}} = -\sigma_{a,238}\overline{N}_{238}A, \tag{11.2b}$$

$$\frac{d\overline{N}_{j}}{d\mathrm{bu}} = -\sigma_{a,j}\overline{N}_{j}A + \sigma_{c,j-1}\overline{N}_{j-1}A, \tag{11.2c}$$

where

$$A = 0.8815\frac{\rho_{fuel}}{\alpha\sum_k \sigma_{f,k}\overline{N}_k}. \tag{11.3}$$

The leading coefficient (0.8815) is the ratio of the mass of U in UO_2 to the mass of UO_2 (238/270). Burnup here is in units of megawatt days per ton heavy metal. σ_f is the fission cross section, and α is the energy released per fission.

The local isotope concentrations are model using

$$\frac{\mathrm{d}N_{235}}{\mathrm{d}\,\mathrm{bu}} = -\sigma_{a,235}N_{235}(r)A, \tag{11.4a}$$

$$\frac{\mathrm{d}N_{238}}{\mathrm{d}\,\mathrm{bu}} = -\sigma_{a,238}\overline{N}_{238}\overline{f}(r)A, \tag{11.4b}$$

$$\frac{\mathrm{d}N_{239}}{\mathrm{d}\,\mathrm{bu}} = -\sigma_{a,239}N_{239}(r)A + \sigma_{c,238}\overline{N}_{238}\overline{f}(r)A, \tag{11.4c}$$

$$\frac{\mathrm{d}N_{j}}{\mathrm{d}\,\mathrm{bu}} = -\sigma_{a,j}N_{j}(r)A + \sigma_{c,j-1}N_{j-1}(r)A, \tag{11.4d}$$

where j represents each of the ^{240}Pu, ^{241}Pu, and ^{242}Pu isotopes. The function $\overline{f}(r)$ is given as

$$\overline{f}(r) = \frac{f(r)}{\int_{r_{in}}^{r_{out}} f(r)r\,\mathrm{d}r} \tag{11.5}$$

which guarantees that

$$\frac{2\int_{r_{in}}^{r_{out}} \overline{f}(r)r\,\mathrm{d}r}{r_{out}^2 - r_{in}^2} = 1. \tag{11.6}$$

The function $f(r)$ is given as

$$f(r) = 1 + p_1 e^{-p_2(r_{out}-r)^{p_3}} \tag{11.7}$$

where p_1, p_2, and p_3 are constants, r_{out} is the outer radius of the pellet, and r is the radial position.

The neutron flux, $\phi(r)$, is a function of the modified Bessel functions:

$$\phi(r) = C_1 I_0(\kappa r) \tag{11.8a}$$

for a solid cylindrical pellet, or

$$\phi(r) = C_1\left(I_0(\kappa r) + \left[\frac{I_1(\kappa r_{in})}{K_1(\kappa r_{in})}\right]K_0(\kappa r)\right) \tag{11.8b}$$

for a hollow cylindrical pellet

where I and K are the modified Bessel functions, C_1 is a constant, and κ is the inverse diffusion length. κ is given as

$$\kappa = \sqrt{\frac{\Sigma_{a,tot}}{D}} \tag{11.9}$$

where

$$\Sigma_{a,tot} = \sum_k \sigma_{a,k}\overline{N}_k$$

and

$$D = \frac{1}{3\sigma_s\overline{N}_{tot}}.$$

$\overline{N}_k$ is the average concentration for each isotope, $\overline{N}_{tot}$ is the average concentration of all isotopes, and σ_s is a constant.

Standard cross section values are given in Table 11.1. By default, BISON uses these fission and capture cross section values. For the absorption cross section values, BISON follows the approach in FRAPCON and sums the fission and capture cross section values for each isotope to get the absorption cross section. Note also that no support for Gd content is available at this time.

Table 11.1: Spectrum average cross sections for the TUBRNP model (in barns). See [31].

Light Water Reactor (BWR and PWR)

	^{235}U	^{238}U	^{239}Pu	^{240}Pu	^{241}Pu	^{242}Pu	^{155}Gd	^{157}Gd
Fission	41.5	0	105	0.584	120	0.458	-	-
Capture	9.7	0.78	58.6	100	50	80	490	1267
Absorption (Thermal)	359.68	1.56	1207.5	193.5	1095.24	11.11	19800	85000

Heavy Water Reactor

	^{235}U	^{238}U	^{239}Pu	^{240}Pu	^{241}Pu	^{242}Pu	^{155}Gd	^{157}Gd
Fission	107.95	0	239.18	0.304	296.95	0.191	-	-
Capture	22.3	1.16	125.36	127.26	122.41	91.3	1471	3800
Absorption (Thermal)	395.59	1.7	1095.7	202.2	1113.7	11.98	23924	102477

As a benchmark problem, a comparison between BISON and FRAPCON radial power factors has been made for a simple fuel pellet. In this problem, the fuel outer diameter is 8.2 mm, the linear power is 20 kW/m, and the fuel is 5% enriched with 95% theoretical density. Figure 11.1 shows the radial power factor at the beginning of the irradiation. Figure 11.2 shows the radial power factor at 33 MWd/kgU. BISON shows excellent agreement with the FRAPCON results.

11.2 Decay Heat

Heat generation due to the radioactive decay of fission products is computed using the "simplified method" described in the 1979 ANS-5.1 Standard on Decay Heat Power in Light Water Reactors [86]. This method assumes that the decay heat power from fissioning isotopes other than ^{235}U is identical to that of ^{235}U and that the fission rate is constant over the operating history at a maximum level corresponding to P_{max}. This simplified method overestimates decay heat power, especially with respect to LWR cores having an appreciable amount of plutonium. For finite reactor operating time, the decay heat power is approximated as

$$P_d(t,T) = P_{max}\frac{1.02G_n\left(F(t,\infty)-F(t+T,\infty)\right)}{Q_{mev}} \tag{11.10}$$

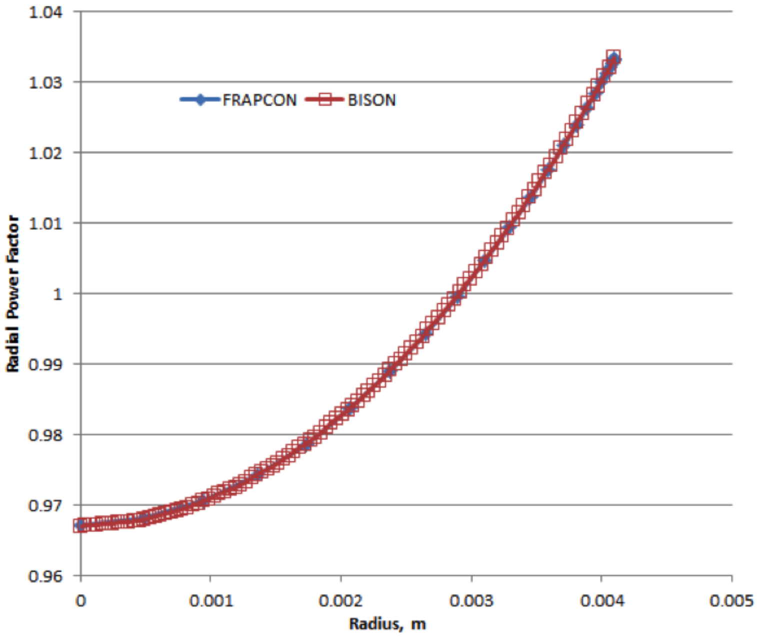

Figure 11.1: BISON and FRAPCON radial power factors for new fuel.

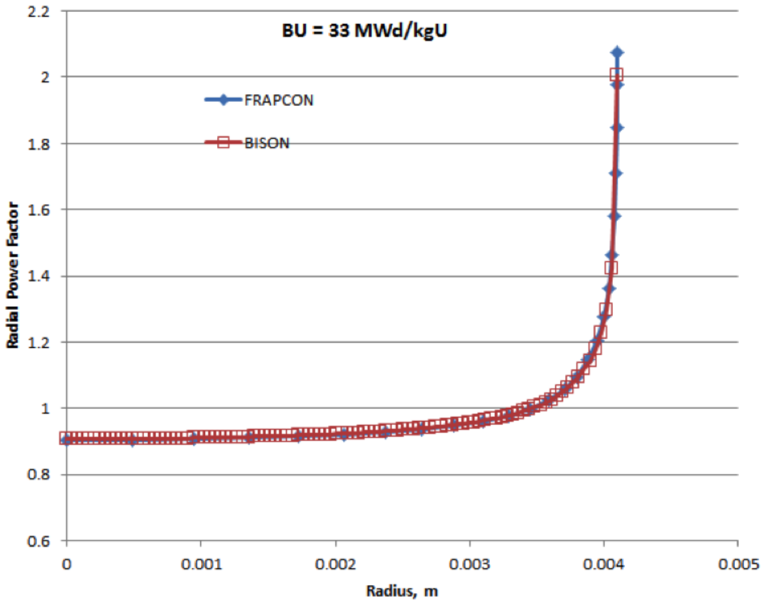

Figure 11.2: BISON and FRAPCON radial power factors at 33 MWd/kgU.

where t is the time following reactor shutdown (s), T is the total operating time including intermediate periods at zero power (s), G_n is the neutron capture factor, Q_{mev} is the energy released per fission (MeV/fission), and $F(t,\infty)$ is the decay heat power (MeV/fission) for thermal fission of ^{235}U for an infinite-time base irradiation (tabulated in Table 4 of [86]).

As implemented in BISON, the decay and peak powers are prescribed as fission power densities at finite element material volumes. Spatial variation of the peak power is dictated by the axial and radial power profiles in the fuel, thus the decay power follows the same profiles.

11.3 Burnup Calculation

Burnup is used to calculate fuel properties and the fuel densification and swelling rates. It is computed at each material or integration point based on the following equation from Olander [77]

$$\beta = \frac{\dot{F}t}{N_f^0} \tag{11.11}$$

where $\dot{F}$ is the volumetric fission rate, t is time, and N_f^0 is the initial density of heavy metal atoms in the fuel, which can be computed as

$$N_f^0 = \frac{\rho N_{av}}{M_w} \tag{11.12}$$

where ρ is the initial fuel density, N_{av} is Avagrado's number, and M_w is the molecular weight.

A burnup increment is computed for each time increment and summed to give the total burnup.

$$\beta_i = \beta_{i-1} + \frac{\dot{F}\Delta t}{N_f^0} \tag{11.13}$$

11.4 Fission Rate

The fission rate is calculated from the local power density.

$$\dot{F} = \frac{P}{\alpha} \tag{11.14}$$

where $\dot{F}$ is the fission rate (fission/m^3/s), P is the power density (W/m^3), and α is the energy released per fission (J/fission). α is commonly taken to be 3.28451e-11 J/fission.

11.5 Fast Neutron Flux

Fast neutron flux may be specified as problem input. However, it may also be estimated given the linear heat rate.

$$\dot{\Phi} = cP \tag{11.15}$$

where $\dot{\Phi}$ is the fast neutron flux, c is a conversion factor, typically 3e13 (n/(m^{2}s)/(W/m)), and P is the linear heat rate (W/m).

11.6 Fast Neutron Fluence

Fast neutron fluence is the time-integrated fast neutron flux. In incremental form,

$$\Phi_{n+1} = \Phi_n + \Delta t \dot{\Phi} \tag{11.16}$$

where Φ_n is the value of the fast neutron fluence at step n, Δt is the timestep size, and $\dot{\Phi}$ is the fast neutron flux.

12 Evolving Density

BISON computes the current density throughout the finite element mesh. Conservation of mass requires

$$\rho = \frac{\rho_0 V_0}{V} \tag{12.1}$$

where ρ and ρ_0 are the current and original mass densities, and V and V_0 are the current and original volumes.

The deformation gradient F is defined as

$$F = I + \nabla u \tag{12.2}$$

where I is the identity tensor and u is the displacement vector. The determinant of the deformation gradient is a measure of volume change:

$$\det(F) = \frac{dV}{dV_0}. \tag{12.3}$$

This allows

$$\rho = \frac{\rho_0}{\det(F)}. \tag{12.4}$$

This calculation is done at each integration point throughout the finite element mesh.

13 Gap/Plenum Models

13.1 Gap Heat Transfer

Gap heat transfer is modeled using the relation,

$$h_{gap} = h_g + h_s + h_r \tag{13.1}$$

where h_{gap} is the total conductance across the gap, h_g is the gas conductance, h_s is the increased conductance due to solid-solid contact, and h_r is the conductance due to radiant heat transfer.

The gas conductance h_g is described using the form proposed by Ross and Stoute [87]:

$$h_g = \frac{k_g}{d_g + C_r(r_1 + r_2) + g_1 + g_2} \tag{13.2}$$

where k_g is the temperature dependent thermal conductivity of the gas in the gap, d_g is the gap width (computed in the mechanics solution), C_r is a roughness coefficient with r_1 and r_2 the roughnesses of the two surfaces, and g_1 and g_2 are jump distances at the two surfaces. The conductivity of the gas mixture (k_g) is computed based on the mixture rule from MATPRO [25], which permits mixtures of ten gases (helium, argon, krypton, xenon, hydrogen, nitrogen, oxygen, carbon monoxide, carbon dioxide, and water vapor). The gas temperature is the average of the local temperatures of the two surfaces.

Temperature jump distance is calculated using Kennard's model based on a review by Lanning [88].

$$g_1 + g_2 = 5756 \left(\frac{2 - a_{mix}}{a_{mix}} \right) \left(\frac{k_g \sqrt{T_g}}{P} \right) \left(\sum_{i=1}^{10} \frac{f_i}{M_i} \right)^{-1/2} \tag{13.3}$$

where the units of $g_1 + g_2$, k_g, and P are cm , $\frac{cal}{cm-K-s}$, and $\frac{dynes}{cm^2}$ respectively, f_i is mole fraction of i-th gas species, M_i is molcular weight of i-th gas species, and a_{mix} is accomodation coefficient for the gas mixture. The accomodation coefficients for helium and xenon are as follows:

$$a_{He} = 0.425 - 2.3 \times 10^{-4} T_g \tag{13.4}$$

$$a_{Xe} = 0.749 - 2.5 \times 10^{-4} T_g \tag{13.5}$$

For a gas mixture,

$$a_{mix} = a_{He} + \frac{(a_{Xe} - a_{He})(M_{mix} - M_{He})}{(M_{Xe} - M_{He})} \tag{13.6}$$

where M_{Xe} is molecular weight of xenon, M_{He} is molecular weight of helium, and M_{mix} is molecular weight of gas mixture.

The increased conductance due to solid-solid contact, h_s, is described using the correlation suggested by Ross and Stoute [87]:

$$h_s = C_s \frac{2k_1k_2}{k_1+k_2} \frac{P_c}{\delta^{1/2}H} \tag{13.7}$$

where C_s is an empirical constant, k_1 and k_2 are the thermal conductivities of the solid materials in contact, P_c is the contact pressure, δ is the average gas film thickness (approximated as 0.8(r_1 + r_2), and H is the Meyer hardness of the softer material. From measurements on steel in contact with aluminum, Ross and Stoute [87] recommend C_s = 10 $m^{-1/2}$, which is the default value in BISON. As an option, the chemical interaction layer at the fuel-cladding interface can be taken into account in the contact term. Based on experimental work [89], the growth of a (U,Zr)O_{2-x} layer is considered during fuel-cladding contact, and is described based on a parabolic law

$$\frac{dS^2}{dt} = G \tag{13.8}$$

where S (m) is the layer thickness, and $G = 4 \times 10^{-18}$ [89] is the parabolic growth rate. Equation 13.8 is solved numerically by

$$S_i = \sqrt{G\Delta t + S_{i-1}^2} \tag{13.9}$$

where

S_i is the layer thickness at the current time step (m)

S_{i-1} is the layer thickness at the previous time step (m)

Δt is the time increment (s)

The chemical interaction layer is assumed to fill the fuel and cladding roughnesses according to its thickness, effectively reducing the r_1 and r_2 terms in Eq. 13.7 and improving the heat transfer.

The conductance due to radiant heat transfer, h_r, is computed using a diffusion approximation. Based on the Stefan-Boltzmann law

$$q_r = \sigma F_e (T_1^4 - T_2^4) \approx h_r (T_1 - T_2) \tag{13.10}$$

where σ is the Stefan-Boltzmann constant, F_e is an emissivity function, and T_1 and T_2 are the temperatures of the radiating surfaces. The radiant conductance is thus approximated

$$h_r \approx \frac{\sigma F_e (T_1^4 - T_2^4)}{T_1 - T_2} \tag{13.11}$$

which can be reduced to

$$h_r = \sigma F_e (T_1^2 + T_2^2)(T_1 + T_2) \tag{13.12}$$

For infinite parallel plates, the emissivity function is defined as

$$F_e = \frac{1}{1/\varepsilon_1 + 1/\varepsilon_2 - 1} \tag{13.13}$$

where ε_1 and ε_2 are the emissivities of the radiating surfaces. This is the specific function implemented in BISON.

13.2 Mechanical Contact

Mechanical contact between fuel pellets and the inside surface of the cladding is based on three requirements:

$$g \leq 0, \tag{13.14}$$

$$t_N \geq 0, \tag{13.15}$$

$$t_N g = 0. \tag{13.16}$$

That is, the penetration distance (typically referred to as the gap g in the contact literature) of one body into another must not be positive; the contact force t_N opposing penetration must be positive in the normal direction; and either the penetration distance or the contact force must be zero at all times.

In BISON, these contact constraints are enforced through the use of node/face constraints. Specifically, the nodes of the fuel pellets are prevented from penetrating cladding faces. This is accomplished in a manner similar to that detailed by Heinstein and Laursen [90]. First, a geometric search determines which fuel pellet nodes have penetrated cladding faces. For those nodes, the internal force computed by the divergence of stress is moved to the appropriate cladding face at the point of contact. Those forces are distributed to cladding nodes by employing the finite element shape functions. Additionally, the pellet nodes are constrained to remain on the pellet faces, preventing penetration. BISON supports frictionless and tied contact. Friction is an important capability, and preliminary support for fricitonal contact is available.

Finite element contact is notoriously difficult to make efficient and robust in three dimensions. That being the case, effort is underway to improve the contact algorithm.

13.3 Gap/plenum pressure

The pressure in the gap and plenum is computed based on the ideal gas law,

$$P = \frac{nRT}{V} \tag{13.17}$$

where P is the gap/plenum pressure, n is the moles of gas, R is the ideal gas constant, T is the temperature, and V is the volume of the cavity. The moles of gas, the temperature, and the cavity volume in this equation are free to change with time. The moles of gas n at any time is the original amount of gas (computed based on original pressure, temperature, and volume) plus the amount in the cavity due to fission gas released. The temperature T is taken as the average temperature of the pellet exterior and cladding interior surfaces, though any other measure of temperature could be used. The cavity volume V is computed as needed based on the evolving pellet and clad geometry.

13.4 Gap/plenum temperature

The gap/plenum pressure (Section 13.3) requires the temperature of the gas inside the cladding. Many choices are possible when supplying this temperature. It may be appropriate to supply the temperature at a node, the average temperature of several nodes, or data from an experiment. In this section, we outline an approach for calculating an average gas temperature that takes into account the entire fuel/cladding system.

We seek a weighted average temperature that accounts for the fact that the majority of the gas is in the plenum region. Using a volume-weighted average, the average gas temperature $\bar{T}$ can be approximated as

$$\bar{T} = \frac{\int T \mathrm{d}V}{\int \mathrm{d}V} \tag{13.18}$$

where T is the temperature at a point in the gap/plenum and V is the volume occupied by the gas.

It is necessary to make some approximations in the calculation of this temperature since the gap and plenum volumes are not meshed. We assume that a differential volume ($\mathrm{d}V$) is equal to a varying distance times a differential area ($\delta \, \mathrm{d}A$). This change is appropriate for replacing the integral over the volume of an enclosed space with the integral of the medial surface of that space times a distance representing the depth of the volume at a particular point on the surface.

With this change, it is necessary to replace T with the temperature associated with $\delta \, \mathrm{d}A$. We take this temperature to be the average temperature of the outer and inner surfaces bounding the volume:

$$T = \frac{T_o + T_i}{2}.$$

The medial surface of the gas volume is not known. We instead use the fuel surface. This gives

$$\bar{T} = \frac{\int_{A_f} \frac{T_o + T_i}{2} \delta \, \mathrm{d}A}{\int_{A_f} \delta \, \mathrm{d}A}$$

where A_f is the fuel surface, T_o is the temperature across the gap, T_i is the temperature on the fuel surface, and δ is the gap distance. This approximation is a good one for the plenum region since the plenum volume can be accurately calculated given our assumptions. The accuracy of the calculation will be lower for the gap volume contribution, but since this volume is small (zero in areas of fuel/cladding contact) it is less important.

Note that since this approach places an appropriately large weight on the gas in the plenum, it is important that the temperature of the fuel adjacent to the plenum be accurate. It may be necessary to place insulating pellets in a model in order to calculate realistic temperatures at the top of the fuel stack.

14 Coolant Channel Model

In the operating conditions of Light Water Reactors, fuel rods are surrounded by flowing water coolant; the flowing coolant carries the thermal energy generated from nuclear fission reaction and transfers the heat into a steam generator or drives a turbine directly. To predict the thermal response of a fuel rod, thermal hydraulic condition of the surrounding coolant needs to be determined. Such condition in modeling the energy transport aspect of the coolant in BISON code is described by a single coolant channel model. This single channel is used mathematically to describe the thermal boundary condition for modeling the fuel rod behavior. This model covers two theoretical aspects, i.e., the local heat transfer from cladding wall into the coolant and the thermal energy deposition in the coolant in steady state and slow operating transient conditions.

Assumptions and limitations of the coolant channel model are summarized below:

1. Closed channel
   The lateral energy, mass, and momentum transfer in the coolant channel within a fuel assembly is neglected. Therefore, the momentum, mass continuity, and the energy equations are only considered in one-dimension, i.e., the axial direction.

2. Homogeneous and equilibrium flow
   For the flow involving both the vapor and liquid phases, the thermal energy transport and relative motions between the two phases are neglected. This essentially assumes the two-phase flow is in a form of one pseudo fluid.

3. Fully developed flow
   In the application of most heat transfer correlations, the entrance effects are neglected. The heat transfer is assumed to happen in a condition that the boundary layer has grown to occupy the entire flow area, and the radial velocity and temperature profiles are well established.

4. Pressure drop neglected
   The pressure drop due to flow induced resistance is not accounted for in the coolant channel model. Instead, coolant pressure as a function of time and axial location can be an input provided by user through a hand calculation or using a computer code.

14.1 Coolant Enthalpy Model

In steady state operation, the enthalpy rise in a coolant channel with incompressible fluid can be derived using energy conservation equation:

$$H(z) = H_{in} + \frac{\int_0^Z q''(z)\pi D_h \mathrm{d}z + \int_0^Z f_c q' \mathrm{d}z}{GA} \tag{14.1}$$

where

H_{in} is the coolant enthalpy at inlet in (J/kg)
$H(z)$ is the coolant enthalpy at axial location z in (J/kg)
z is axial location (m)
q'' is fuel rod surface heat flux (W/m^2)
q' is fuel rod linear heat generation rate (W/m)
f_c is the fraction of heat generated in the coolant by neutron and gamma rays (dimensionless)
D_h is heated diameter (m)
G is coolant mass flux (kg/sec-m^2)
A is flow area of the coolant channel (m^2)

The mass flux, pressure, and coolant temperature at the inlet of coolant channel are provided as input for calculating coolant enthalpy rise. With calculated enthalpy and input coolant pressure, the corresponding thermodynamic condition can be determined using a steam table. The coolant temperature can be obtained and would be used in the convective boundary condition to compute the clad temperature. The thermal-physical properties of water and steam are evaluated at the corresponding bulk coolant temperature and/or at the cladding wall temperature for the use of calculating heat transfer coefficients between the cladding wall and the coolant.

The inlet mass flux, pressure, and coolant temperature can be provided as functions of time in the code input. Allowing the variation of inlet thermal-hydraulic conditions can be used to model a quasi-steady state when the velocity and thermal energy of coolant at a given location are assumed to achieve the equilibrium condition instantaneously.

14.2 Pre-CHF Heat Transfer Correlations

Depending on the flow rate, flow pattern, and cladding wall surface heat flux, the heat transfer from cladding wall outer surface to coolant can be characterized into different heat transfer regimes.

A set of heat transfer correlations to describe the heat transfer condition prior to the point of Critical Heat Flux (CHF) is described follows:

- Dittus-Boelter correlation:
  Under forced flow condition and when the coolant is still in the liquid phase, the heat transfer from the cladding wall to the coolant is in the regime of single phase forced convection, and the heat transfer can be described by Dittus-Boelter equation.

  $$Nu = 0.023 Re^{0.8} Pr^{0.4} \tag{14.2}$$

  The equation is applicable for $0.7 < \mathrm{Pr} < 100$, $\mathrm{Re} > 10{,}000$, and $L/D > 60$. Fluid properties are evaluated at the arithmetic mean bulk temperature [91].

- Jens-Lottes correlation:

  $$\Delta T = 25\left(\frac{q''(z)}{10^6}\right)^{0.25} / e^{P/6.2\times10^6} \tag{14.3}$$

Where, ΔT is the cladding wall super heat = T_W-T_{sat} in (K). q'' is the cladding wall surface heat flux (W/m^2-K)), and P is the coolant pressure (Pa). This correlation is developed based on data at a pressure between 500 psi (3.45 MPa) and 2000 psi (13.79 MPa) in sub-cooled boiling regime. The heat transfer coefficient is given as:

$$h = \frac{[(T_W - T_{sat})e^{P/6.2\times10^6}/25]^4 \times 10^6}{T_W - T_b} \tag{14.4}$$

- Thom correlation:
  A similar correlation is given as follows:

$$\Delta T = 22.7\left(\frac{q''(z)}{10^6}\right)^{0.5} / e^{P/8.7\times10^6} \tag{14.5}$$

The heat transfer coefficient is:

$$h = \frac{[(T_W - T_{sat})e^{P/8.7\times10^6}/22.7]^2 \times 10^6}{T_W - T_b} \tag{14.6}$$

This correlation is for water at a pressure between 750 psi (5.17 MPa) and 2000 psi (13.79 MPa); but much of Thom's data were obtained at relatively low heat fluxes according to Tong [92].

- Shrock-Grossman correlation
  Shrock-Grossman heat transfer correlation is used in the regime of saturated boiling. The heat transfer coefficient is given as:

$$h = \left(a_1 \frac{q''}{Gh_{fg}} + a_2 X_{tt}^{-b}\right) h_l \tag{14.7}$$

$$X_{tt}^{-1} = \left(\frac{x}{1-x}\right)^{0.9} \left(\frac{\rho_f}{\rho_g}\right)^{0.5} \left(\frac{\mu_g}{\mu_f}\right)^{0.1} \tag{14.8}$$

Where,
x is the steam quality
h_{fg} is the latent heat of vaporization (J/kg)
h_l is the heat transfer coefficient in the liquid phase at the same mass flux (J/kg)
G is the mass flux (kg/m^2-sec)
a_1, a_2, and b are constants as follows:
$a_1 = 7400$
$a_2 = 1.11$
$b = 0.66$

- Chen's correlation

An alternative correlation that is used in the saturated boiling regime is Chen's correlation. Chen's correlation consists of a convective term (Fh_c) and a nucleation term (Sh_{NB}):

$$h = Fh_c + Sh_{NB} \tag{14.9}$$

h_c is the modified Dittus-Boelter correlation:

$$h_c = 0.023\left(\frac{G(1-x)D_e}{\mu_f}\right)^{0.8} Pr_f^{0.4}\frac{k_f}{D_e} \tag{14.10}$$

F is a factor to account for the enhanced heat transfer due to the turbulence caused by vapor.

$$F = 1,\ \text{for } \frac{1}{X_{tt}} < 0.1 \tag{14.11}$$

$$F = 2.35\left(0.213 + \frac{1}{X_{tt}}\right)^{0.736},\ \text{for } \frac{1}{X_{tt}} > 0.1 \tag{14.12}$$

The nucleation term is the Forster-Zuber equation:

$$h_{NB} = 0.00122\left[\frac{(k^{0.79}c_p^{0.45}\rho^{0.49})_f}{\sigma^{0.5}\mu_f^{0.29}h_{fg}^{0.25}\rho_g^{0.24}}\right]\Delta T_{sat}^{0.24}\Delta P^{0.75} \tag{14.13}$$

$$\Delta T_{sat} = T_W - T_{sat} \tag{14.14}$$

$$\Delta P = P(T_W) - P(T_{sat}) \tag{14.15}$$

S is a suppression factor:

$$S = \frac{1}{1 + 2.53\times10^{-6}Re^{1.17}} \tag{14.16}$$

Where $Re = Re_l F^{1.25}$; Re_l is the Reynold number for liquid phase only.

14.3 Critical Heat Flux Correlations

The sub-cooled and saturated boiling can enhance the heat transfer; however at a critical condition when the cladding outer surface is enclosed by vapor film, the heat transfer can deteriorate significantly, the corresponding heat flux is the Critical Heat Flux (CHF). The following correlations are implemented in BISON to calculate CHF, which can be used to estimate the thermal margin in a coolant channel.

- EPRI-Columbia correlation

$$\frac{q_{CHF}}{10^6} = \frac{A - x_{in}}{C + (\frac{x - x_{in}}{q''})} \tag{14.17}$$

where
$A = F_a p_1 p_r^{p_2} G^{(p_5+p_7 p_r)}$
$C = F_c F_{AP} p_3 p_r^{p_4} G^{(p_6+p_8 p_r)}$
$p_1 = 0.5328$
$p_2 = 0.1212$
$p_3 = 1.6151$
$p_4 = 1.4066$
$p_5 = -0.3040$
$p_6 = 0.4843$
$p_7 = -0.3285$
$p_8 = -2.0749$
p_r = critical pressure ratio=system pressure/critical pressure
G = local mass velocity (Mlbm/hr-ft^2)
x_{in} = inlet quality
$F_a = G^{0.1}$
$F_c = 1.183 G^{0.1}$
$F_a = F_c = 1$ for no cold wall
q'' =local heat flux (MBtu/hr-ft^2)

F_{AP} is the non-uniform axial heat flux distribution parameter:

$$F_{AP} = 1 + \frac{(Y-1)}{(1+G)} \tag{14.18}$$

Y is Bowring's non-uniform parameter defined as:

$$Y = \frac{\int_0^z q''(z)\mathrm{d}z}{q''(z)z} \tag{14.19}$$

- GE correlation

$$q_{CHF} = 10^6(0.8-x) \text{ for } G \geq 0.5 \times 10^6 \text{ lb}_\text{m}/\text{ft}^2\text{-hr} \tag{14.20}$$

$$q_{CHF} = 10^6(0.84-x) \text{ for } G < 0.5 \times 10^6 \text{ lb}_\text{m}/\text{ft}^2\text{-hr} \tag{14.21}$$

The correlation is applicable for mass fluxes less than 0.75×10^6 lb$_\text{m}$/ft^2-hr.

- Zuber correlation [93]

$$q_{CHF} = 0.131 h_{fg} \rho_g^{0.5} (\sigma g(\rho_f - \rho_g))^{0.5} \tag{14.22}$$

where
q_{CHF} is the critical heat flux (W/m^2)

h_{fg} is the latent heat of vaporization (kJ/kg)
g is the acceleration due to gravity = 9.8 (m/s^2)
ρ_g is the density of vapor at saturation temperature (kg/m^3)
ρ_f is the density of liquid at saturation temperature (kg/m^3)
σ is the surface tension energy at saturation temperature (N/m)

- BIASI correlation
  BIASI correlation is a function of pressure, mass flux, flow quality, and tube diameters. The correlations are provided in following equations. For $G < 300$kg/m^2-s, the Eq. 14.23 is used; for higher mass flux, the Eq. 14.23 or Eq. 14.24 whichever higher is used.

$$q_{chf} = (15.048 \times 10^7)(100D)^{-n}G^{-0.6}H(p_{bar})(1-x) \tag{14.23}$$

$$q_{chf} = (2.764 \times 10^7)(100D)^{-n}G^{-0.6}\left[1.468F(p_{bar})G^{-1/6} - x\right] \tag{14.24}$$

where,
$F(p_{bar}) = 0.7249 + 0.099p_{bar}exp(-0.032p_{bar})$
$H(p_{bar}) = -1.159 + 0.149p_{bar}exp(-0.019p_{bar}) + 9p_{bar}(10+p_{bar}^2)^{-1}$
$p_{bar} = 10P$
P is the pressure (MPa)

$$n = \begin{cases} 0.4 & \text{for} \quad D \geq 0.01\text{m} \\ 0.6 & \text{for} \quad D < 0.01\text{m} \end{cases}$$

The database for the correlation is
D=0.003-0.0375 m
L=0.2-6.0 m
P=0.27-14 MPa
G=100-600 kg/m^2-s
x=$1/(1+\rho_f/\rho_g)$-1

The EPRI correlation is used as the correlation for a Pressurized Water Reactor (PWR) environment. The GE correlation is used as the correlation for a Boiling Water Reactor (BWR) environment. Alternatively, an input temperature at critical heat flux is allowed, which would use the selected heat transfer in the nucleate boiling regime and the input temperature to compute the critical heat flux.

14.4 Post-CHF Heat Transfer Correlation

The post-CHF heat transfer regime is divided into transition boiling and film boiling. The transition boiling heat transfer regime occurs when the cladding wall temperature exceeds the Critical Heat Flux (CHF) temperature, but remains below the minimum film boiling temperature. The heat flux decreases significantly with increasing temperature in this regime. Two heat transfer correlations are implemented for the transition boiling regime. The two correlations are McDonough-Milich-King and modified Condie-Bengtson correlations. The film boiling heat transfer regime occurs when the wall temperature reaches the minimum film boiling temperature. Two correlations are provided for the film boiling region. The correlations are Dougall-Rohsenow and Groenveld correlations. The heat transfer correlations at CHF and in the post-CHF regimes implemented in the BISON code is described as follows:

14.4.1 Transition Boiling

McDonough-Milich-King correlation and modified Condie-Bengtson correlation are implemented for the transition boiling regime.

- McDonough-Milich-King correlation [91] [31]
  The McDonough-Milich-King correlation for forced convection transition boiling is given as follows:

  $$\frac{(q_{CHF} - q_{TB})}{(T_W - T_{CHF})} = 4.15e^{3.97/P} \tag{14.25}$$

  The heat transfer coefficient is:

  $$h_{TB} = \frac{q_{CHF} - 4.15e^{3.97/P}(T_W - T_{CHF})}{(T_W - T_b)} \tag{14.26}$$

  Where,
  q_{CHF} is the critical heat flux (kW/m^2)
  q_{TB} is the transition region heat flux (kW/m^2)
  T_{CHF} is the wall temperature at critical heat flux (K)
  T_b is the bulk temperature of coolant (K)
  T_W is the wall temperature in the transition region (K)
  P is the system pressure (MPa)
  h_{TB} is the transition boiling heat transfer coefficient (kW/m^2-K)

  The data range for this correlation is as follow:
  Pressure: 5.5 - 13.8 MPa
  Mass Flux: 271.246 - 1898.722 kg/m^2-sec
  Channel Geometry: Tube
  Diameter: 0.00386 m
  Length: 0.3048 m
  Fluid: Water

- Modified Condie-Bengtson correlation [31]
  The modified Condie-Bengtson correlation for high flow rate transition boiling is given as

follows:

$$q_{TB} = C_1 e^{-\frac{(T_W - T_{sat})^{1/2}}{2}} (T_W - T_{sat}) \tag{14.27}$$

The heat transfer coefficient is:

$$h_{TB} = C_1 e^{-\frac{(T_W - T_{sat})^{1/2}}{2}} \tag{14.28}$$

$$C_1 = e^{ln(q_{CHF} - q_{FB}) + 0.5(T_{CHF} - T_{sat})^{1/2} - ln(T_{CHF} - T_{sat})} \tag{14.29}$$

where,
q_{CHF} is the critical heat flux (Btu/hr-ft^2)
q_{TB} is the transition heat flux (Btu/hr-ft^2)
$q_{FB} = h_{FB}(T_{CHF} - T_{sat})$ is the film boiling heat flux at T_{CHF} (Btu/hr-ft^2)
T_{CHF} is the wall temperature at critical heat flux (^{o}F)
T_{sat} is the saturation temperature (^{o}F)
T_W is the cladding wall temperature (^{o}F)
h_{TB} is the transition boiling heat transfer coefficient (Btu/hr-ft^2-^{o}F)

At the CHF point, T_W = T_{CHF}, and

$$q_{TB} = q_{CHF} - q_{FB} \tag{14.30}$$

At T_{CHF}, the critical heat flux is equal to the sum of the film boiling component and the transition boiling component to ensure the predicted boiling curve is continuous.

14.4.2 Film Boiling

Two correlations, Dougall-Rohsenow correlation and Groenveld correlation, are provided for modeling the heat transfer in the film boiling region. In the transition from the transition boiling regime to the film boiling regime, the intercept of the selected film boiling correlation and transition boiling correlation was used to determine the minimum film boiling temperature and minimum film boiling heat flux.

- Dougall-Rohsenow correlation [94] [31]
  The Dougall-Rohsenow correlation for forced convection stable film boiling was developed for high flow rate and low quality (x $<$ 0.3) flow. The heat transfer coefficient is given as:

$$h_{FB} = 0.023 \frac{k_g}{D_{hy}} \left[\frac{G D_{hy}}{\mu_g} \left(x + (1-x) \frac{\rho_g}{\rho_l} \right) \right]^{0.8} \left[\frac{C_{pg} \mu_g}{k_g} \right]^{0.4} \tag{14.31}$$

  Where,
  G is the mass flux (kg/m^2-sec)
  D_{hy} is the hydraulic diameter (m)
  k_g is the thermal conductivity of vapor (W/m-K)

μ_g is the viscosity of vapor (kg/m-sec)
ρ_g is the density of vapor (kg/m^3)
ρ_l is the density of liquid (kg/m^3)
C_{pg} is the specific heat of vapor (J/kg-K)
x is the local quality

The vapor properties of the Prandtl number are evaluated at the saturation temperature. The data range for this correlation is as follow:
Pressure: 0.1154 - 0.1634 MPa
Mass Flux: 450.268 - 1109.396 kg/m^2-sec
Heat Flux: 45.426 - 131.862 kW/m^2
Exit Quality: up to 0.4
Fluid: Freon
Geometry: Tubes
Inner Diameter: 0.004572 m, 0.01036 m
Length: 0.381 m

- Groenveld correlation [91] [31]
  The Groenveld correlation for forced convection stable film boiling heat transfer coefficient is:

$$h_{FB} = a\frac{k_g}{D_{hy}}\left[\frac{GD_{hy}}{\mu_g}\left(x+(1-x)\frac{\rho_g}{\rho_l}\right)\right]^b (Pr_{\text{film}})^c Y^d \tag{14.32}$$

Where the parameter Y is given as

$$Y = 1.0 - 0.1\left[(1-x)(\frac{\rho_l}{\rho_g}-1)\right]^{0.4} \quad or \quad Y = 0.1 \tag{14.33}$$

whichever is larger.

Where,
G is the mass flux (kg/m^2-sec)
D_{hy} is the hydraulic diameter (m)
k_g is the thermal conductivity of vapor (W/m-K)
μ_g is the viscosity of vapor (kg/m-sec)
ρ_g is the density of vapor (kg/m^3)
ρ_l is the density of liquid (kg/m^3)
x is the local quality

The coefficients a, b, c and d are given in Table 14.1 below. The Prandtl number of the film is given by

$$Pr_{\text{film}} = \frac{C_{pf}\mu_f}{k_f} \tag{14.34}$$

C_{pf} is the specific heat of vapor at film temperature (J/kg-K)
μ_f is the viscosity of vapor at film temperature (kg/m-sec)
k_f is the thermal conductivity of vapor at film temperature (W/m-K)

The vapor properties of the Prandtl number should be evaluated at the film temperature according to Ref. [1].

$$T_{\text{film}} = \frac{(T_W + T_{sat})}{2} \tag{14.35}$$

where,
T_{sat} is the saturation Temperature (K)
T_W is the cladding wall temperature (K)

Prandtl number is currently evaluated at the saturation temperature in the code.

Table 14.1: Groenveld correlation coefficients a, b, c, d

Parameter	Value
a	0.0522
b	0.688
c	1.26
d	-1.06

The applicable range of data for annuli geometry is shown in the Table 14.2 below.

Table 14.2: Range of data for Groenveld correlation

Parameter	Data Range for Annuli Geometry
Hydraulic Diameter (mm)	1.5 - 6.3
Pressure (MPa)	3.4 - 10
Mass Flux (kg/m^2-sec)	800 - 4100
Heat Flux (kW/m^2)	450 - 2250
Quality	0.1 - 0.9

14.5 Logic to Determine Heat Transfer Regime

The boiling curve in the BISON code depends on the selected pre-CHF, CHF, and post-CHF correlations. The diagrams in Figure 14.1 shows the criteria used in the selection of different heat transfer regimes.

Dittus-Boelter correlation is used for the single phase liquid forced convection and for the single phase vapor forced convection. Thom or Jens-Lottes correlation is used for the sub-cooled boiling regime. Thom, Jens-Lottes, or Chen correlation is used for the forced boiling convection regime. Shrock-Grossman correlation is used for the forced boiling convection and vaporization

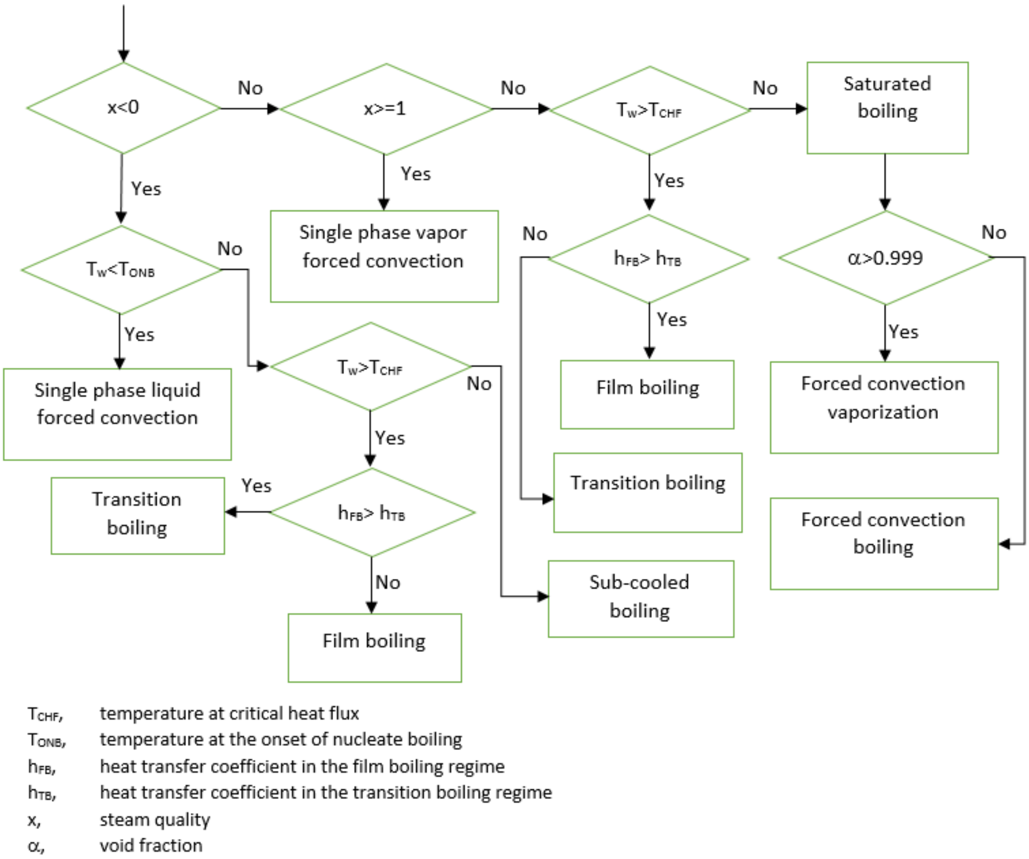
x<0
No
x>=1
No
Tw>TCHF
No
Saturated boiling
Yes
Yes
Yes
Single phase vapor forced convection
No
No
hFB> hTB
No
α>0.999
Tw<TONB
Yes
Yes
Yes
Single phase liquid forced convection
Tw>TCHF
No
Film boiling
Forced convection vaporization
Yes
Transition boiling
Yes
Transition boiling
hFB> hTB
Forced convection boiling
No
Sub-cooled boiling
Film boiling
TCHF, temperature at critical heat flux
TONB, temperature at the onset of nucleate boiling
hFB, heat transfer coefficient in the film boiling regime
hTB, heat transfer coefficient in the transition boiling regime
x, steam quality
α, void fraction

Figure 14.1: Schematic of heat transfer regimes selection criteria

regime. In the transition boiling regime, either the MCDonough-Milich-King ocrrelation or the modified Condie-Bengtson correlation is ued. In the film boiling regime, Dougall-Rohsenow or Groenveld correlation is used. T_{ONB} is the temperate at the onset of nucleate boiling. T_{CHF} is the temperature at the critical heat flux. The selection of different types heat transfer correlations is described in the users manual.

14.6 FLECHT Reflood Heat Transfer Correlation

An alternative approach for modeling the reflooding phase of a LOCA is using the empirical correlations from FLECTH tests [95] [96]. This set of correlation has accounted for the movement of the quench front in the fuel rod.

The generalized FLECHT correlation is used to calculate the cladding surface heat transfer coefficient during the reflood phase of a LOCA. The heat transfer coefficient is a function of flooding rate, cladding temperature at the start of flooding, fuel rod power at the start of flooding, flooding water temperature, vessel pressure, elevation and time [95]. The applicable ranges of these variables are shown in Table 14.3. The FLECHT correlation divides the reflood heat transfer into four time periods and has a different heat transfer correlation for each period. The four time periods are defined as follow: period of radiation only, period I, period II, and period III.

The variables are defined as follow:

V_{in} = flooding rate (in/s)

T_{init} = Peak cladding temperature at start of flooding (^{o}F)

Q'_{max} = fuel rod power at axial peak at start of flooding (kW/ft)

P = reactor vessel pressure (psia)

Z = equivalent FLECHT elevation (ft)

T_{sub} = flood water subcooling at inlet (^{o}F)

t = time after start of flooding as adjusted for variable flooding rate (s)

h = heat transfer coefficient (Btu/(hr-ft^2-^{o}F))

Q'_{maxtq} = radial power shape factor

= 1.0 for a nuclear fuel rod

= 1.1 for electrical rod with radially uniform power

B = flow blockage (%)

Table 14.3: Range of data for Groenveld correlation

Variable	Applicable range of variable in British unit	Applicable range of variable in SI unit
Flooding rate	0.4 - 10 in/s	0.01016 - 0.254 m/s
Reactor vessel pressure	15 - 90 psia	0.1034 - 0.6205 MPa
Inlet coolant subcooling	16 - 189 ^{o}F	264.26 - 360.37 K
Initial cladding temperature	300 - 2200 ^{o}F	420.37 - 1477.59 K
Flow blockage ratio	0 - 75 %	0 - 75 %
Equivalent elevation in FLECHT facility	2 - 10 ft	0.6096 - 3.048 m

14.6.1 Period of Radiation Only

The heat transfer due to radiation is modeled during the time range of t > 0 and t $\leq t_1$. The heat transfer coefficient expression is given as

$$h = h_o + \Delta h[1 - e^{-0.0025t^2}] \tag{14.36}$$

where

$$t_1 = \frac{274e^{-0.0034T_{init}}e^{-0.465V_{in}}e^{-1.25Q'_{max}}}{(1+50^{-0.2(P-30)})} \tag{14.37}$$

$$h_o = 3.67Q'_{max}\left[1 - e^{\left(-\frac{(T_{init}-700)}{435}\right)}\right]F \quad if \quad T_{init} > 700^{o}\text{F} \tag{14.38}$$

$$h_o = 0 \quad if \quad T_{init} \leq 700^{o}\mathrm{F} \tag{14.39}$$

$$F = F_2 + \frac{(1 - F_2)}{(1 + 50^{(Z-7)})} \tag{14.40}$$

$$F_2 = 0.3 + \frac{0.7}{(1 + 50^{(2-V_{in})})} \tag{14.41}$$

$$\Delta h = 0.0397 Q'_{max}(T_{init} - 100) \tag{14.42}$$

14.6.2 Period I

During Period I, the flow develops from the radiation dominated pre-reflood condition to single phase steam flow, to dispersed flow, and finally to unstable film boiling. The time range of Period I is

$$t_1 < t \quad and \quad t_q < t_{q2} \tag{14.43}$$

Where t_q is defined as

$$t_q = \frac{t - t_1}{t_{q6} - t_1} \tag{14.44}$$

$$\begin{aligned} t_{q6} = 98.39[&e^{-0.0107\Delta T_{sub}}(1 - e^{-0.667V_{in}})(1 + 0.5e^{-0.000037P^3} + 1.3e^{-0.111V_{in}^2} \\ &+ 17.3e^{-0.000037P^3}e^{-0.49V_{in}^2})(1.207{Q'_{maxtq}}^{1.5} - 0.667) + \left(\left(\frac{3.28}{V_{in}}\right)^{1.1} - 2.8e^{-V_{in}}\right) \\ &(1 + 0.5e^{-0.000037P^3})](1 + 0.0000588T_{init} - 1.05e^{-0.0025T_{init}}) \\ &\left(1 + \frac{0.5}{(1 + 50^{(2-0.667V_{in})})}\right)\left((1 + \frac{0.32}{(1 + 50^{(5-0.1P)})}\right) \end{aligned} \tag{14.45}$$

t_{q2} is defined as

$$t_{q2} = 0.62[(1 - e^{-0.192Z}) - 0.115Ze^{-0.0368Z^2}] \tag{14.46}$$

The heat transfer coefficient during Period I is calculated as follow

$$\begin{aligned} h = h_1 &\left[1 - e^{\left(-\frac{10(X_2 - X)}{X_2}\right)}\right] + \left[h_{12} - h_1\left(1 - e^{\left(-\frac{10(X_2 - X)}{X_2}\right)}\right)\right] \\ &[1 - e^{-X} - 0.9Xe^{-X^2}]\left[1 - \frac{2.21e^{-0.4V_{in}}ue^{-u}e^{-(0.588Z - 3.824)^2}}{\left(1 + 100^{10(\frac{t_q}{t_{q2}} - 9)}\right)}\right] \end{aligned} \tag{14.47}$$

where

$$h_1 = 3.67Q'_{max}\left(1 - e^{\left(-\frac{T_{init}-700}{435}\right)}\right) + \Delta h(1 - e^{-0.0025t_1^2}) \quad if\ T_{init} > 700^{\mathrm{o}}\mathrm{F} \tag{14.48}$$

$$h_1 = \Delta h(1 - e^{-0.0025t_1^2}) \quad if \quad T_{init} \leq 700^{\mathrm{o}}\mathrm{F} \tag{14.49}$$

$$X_2 = 17.6[1 + 4.37e^{-0.0166\Delta T_{sub}}][1 - e^{-(0.00075+0.0000272(V_{in}-8)^2)f_6}]t_{q2}f_1 \tag{14.50}$$

$$\begin{aligned} h_{12} = 2.644 + 1.092Q'_{max} + [35.7 + (22 - 0.00303Z^{4.1})(1 - e^{-0.0383P} \\ - 0.034Pe^{-0.0011P^2})][1 - e^{-0.2V_{in}}] + 8[1 - e^{-2V_{in}}]\left[1 - e^{\left(-\frac{B}{25}\right)}\right] \end{aligned} \tag{14.51}$$

$$X = 17.6[1 + 4.37e^{-0.0166\Delta T_{sub}}][1 - e^{-(0.0075+0.0000272(V_{in}-8)^2)f_6}]t_q\left(\frac{t - t_1}{t_{q2}(t_{q6} - t_1)}\right)^{f_2} \tag{14.52}$$

$$u = 9\left[\frac{f_1 t_q}{(t_{q2}^{1+f_2 f_3})}\right]^2 \tag{14.53}$$

$$f_1 = 0.436 + 0.455f_5 \tag{14.54}$$

$$f_2 = 0.564 - 0.455f_5 \tag{14.55}$$

$$f_3 = 2.8 - 4.8e^{0.688-1.67V_{in}} \tag{14.56}$$

$$f_4 = 1 - e^{-(0.026P+1.041V_{in}+10.28e^{-3.01Q'_{max}}-0.651)} \tag{14.57}$$

$$f_5 = Q'_{max} + \frac{(1.24 - Q'_{max})}{(1 + 50^{(5-2V_{in})})} \tag{14.58}$$

$$f_6 = 0.5[T_{init} - 1000 + (T_{init}^2 - 2000T_{init} + 1.0001(10^6))^{0.5}] + 350 \tag{14.59}$$

14.6.3 Period II

During this period, the flow pattern has fully developed to quasi-steady state of either unstable film boiling or dispersed boiling, and the heat transfer coefficient reaches a plateau with a rather slow increase. The time range for Period II is

$$t_{q2} < t_q < t_{q3} \tag{14.60}$$

where

$$t_{q3} = 1.55[(1 - e^{-0.205Z}) - 0.154Ze^{-0.0421Z^2} + 0.26e^{-2.77(10^6)T_{init}^2}] \tag{14.61}$$

The heat transfer coefficient during Period II is computed by the equation

$$h = h_2 + b_1[y^2 + b_2(y^2 - b_3y^3) + b_4y^2e^{-6.38y}] + 60e^{-2.77(10^6)T_{init}^2}\left(\frac{y}{y_3}\right)e^{-2.25\left(\frac{y}{y_3}\right)^2} \tag{14.62}$$

$$h_2 = h_{12}[(1 - e^{X_2} - 0.9X_2e^{-X_2^2})] \tag{14.63}$$

$$\begin{aligned} b_1 = {} & [682 - 650(1 - e^{4-Z})][1 - e^{0.95(1-0.0488Z)V_{in}}][1 - e^{-0.0238\Delta T_{sub}}] \\ & \left[0.696 + 0.304e^{-\left(\frac{B}{25}\right)}\right][1 + 0.2(1 - f_4)][1 + e^{-0.8503Z^2+1.0986123Z+2.3025851}] \end{aligned} \tag{14.64}$$

$$y = t_q - t_{q2} \tag{14.65}$$

$$y_3 = t_{q3} - t_{q2} \tag{14.66}$$

$$b_2 = 0.4Z[1 - e^{-2(Z-3.5)}][1.33(1 - e^{-0.0227P}) - 1] - 2.9[1 - e^{-\frac{V_{in}}{2.5}}][1 - e^{-\frac{B}{25}}] \tag{14.67}$$

$$b_3 = 2.55(Z - 3.7)^2e^{3.7-Z} \tag{14.68}$$

$$b_4 = 87.5V_{in}e^{-V_{in}^2}e^{-0.036\Delta T_{sub}} \tag{14.69}$$

$$if \quad Z < 4, \quad b_3 = b_2 = 0 \tag{14.70}$$

14.6.4 Period III

During this period, the flow pattern changes to stable film boiling and the heat transfer coefficient increases rapidly as the quench front approaches. The time range of Period III is

$$t_{q3} < t_q \tag{14.71}$$

t_q is the time of quenching
The heat transfer coefficient during Period III is calculated as follow

$$h = h_3 + C(t_q - t_{q3}) \tag{14.72}$$

$$h_3 = h_2 + b_1[y_3^2 + b_2(y_3^2 - b_3y_3^3) + b_4y_3^2e^{-6.38y_3}] \tag{14.73}$$

$$C = 420[1 - e^{-0.00625b_1}]f_4 \tag{14.74}$$

$$y_3 = t_{q3} - t_{q2} \tag{14.75}$$

14.6.5 Modification for Low Flooding Rates

The heat transfer coefficients for Periods I, II, and III is multiplied by a factor f to best match the test data performed at low flooding rates. The factor f is calculated as follow

$$f = f_7 - f_8 \tag{14.76}$$

Where

$$f_7 = 0.978 + \frac{0.022}{[1 + 30^{(t_{q2}-t_q)}(t_{q6} - t_1)]} \tag{14.77}$$

$$f_8 = f_a + \frac{1 - f_a}{[1 + 50^{(Z-7)}]} \tag{14.78}$$

$$f_a = f_b + \frac{1 - f_b}{[1 + 50^{(2-V_{in})}]} \tag{14.79}$$

$$f_b = 0.3 + 0.7[1 - e^{-1.5t_q}] \tag{14.80}$$

14.7 Properties for Water and Steam

Properties for water and steam consist of thermodynamic properties, transport properties, and other physical properties used in the heat transfer correlations. They are implemented based on a few standards specified by the International Association or Properties for Water and Steam (IAPWS). The thermodynamic properties, or the steam tables, are implemented in the MOOSE module, `water_steam_eos`, using a standard for industry application, IAPWS-IF97 standard [97].

IAPWS-IF97 covers thermodynamic properties for water and steam in following range:

$$273.15\text{ K} < T < 1073.15\text{ K},\ p \leq 100\text{ MPa} \tag{14.81}$$

$$1073.15\text{ K} < T < 2273.15\text{ K},\ p \leq 50\text{ MPa} \tag{14.82}$$

Figure 14.2 shows the five regions defined in IAPWS-IF97. Region 1 represents the liquid phase. Region 2 describes the vapor phase. Region 4 is the saturation curve that separates the liquid phase and the vapor phase. Region 3 describes water properties near the critical point. Region 5 is used for very high temperature condition and is not of interest to any reactor operation; thus region 5 is not included in the BISON coolant channel model.

Ref [97] describes the equations used in the calculation of thermodynamic properties using basic equations which are functions of temperature and/or pressure or temperature and density.

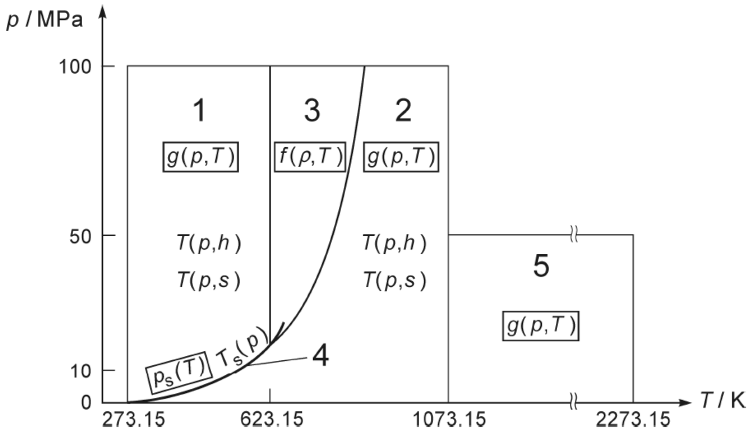
p / MPa
100
50
10
0
1
3
2
g(p,T)
f(ρ,T)
g(p,T)
T(p,h)
T(p,s)
T(p,h)
T(p,s)
5
g(p,T)
p_s(T)
T_s(p)
4
273.15
623.15
1073.15
2273.15
T / K

Figure 14.2: Regions and Equations of IAPWS-IF97 [97]

Viscosity and thermal conductivity of water and steam are functions of density and temperature; these transport properties are implemented based on the information in [98] and [99]. Surface tension of water as a function of temperature is given in [100].

These physical properties are used together with IAPWS-IF97 standard in evaluating properties for water and steam.

15 Cladding Corrosion Model

15.1 Zirconium Alloy at Normal Operating Temperatures

15.1.1 Introduction

Zirconium alloy cladding can have an exothermic reaction with coolant water which converts metal to oxide at the cladding outer surface:

$$\mathrm{Zr} + \mathrm{H_2O} \rightarrow \mathrm{ZrO_2} + 2\mathrm{H_2} + 6.5 \times 10^6 \ \mathrm{J/kgZr} \tag{15.1}$$

Such an oxidation process, which is referred to as water-side corrosion, is a fundamental aspect of LWR fuel performance. The resultant oxide film on the outer surface of cladding can affect both the thermal and mechanical properties of cladding. Because of the lower thermal conductivity of zirconium oxide in comparison with zirconium alloys, the oxidation of the cladding adds to thermal resistance to heat transfer from the fuel to the coolant. Zirconium oxide is a brittle material and can be easily cracked. Thus it is expected that the mechanical strength of cladding is mainly determined by the metallic wall, which is thinned after corrosion. Concurrent to the oxidation process, a fraction of hydrogen can be absorbed into the metal and can diffuse under the influences of both temperature and stress. Due to the low solubility of hydrogen in zirconium and its alloys, hydrogen can precipitate as δ-phase hydrides ($\mathrm{ZrH_{1.66}}$), which are known to further reduce the ductility of irradiated cladding material. In fact, the hydrogen content in the zircaloy cladding has become a limiting parameter for burnup extension of LWR fuel. An oxidation model which can predict the growth of oxide layer as a function of operation conditions and metallurgical variables of cladding materials is essential to the study of LWR fuel performance. In addition, it is also of interest to account for the effects of the oxide layer on the thermal and mechanical properties of cladding.

Low temperature (250 °C/ 523 K to 400 °C/ 673 K) oxidation is calculated considering that cladding oxidation under normal LWR conditions occurs in two stages: a pre-transition oxidation process that follows a cubic time dependence up to a transition oxide thickness, and a post-transition process that follows a linear time dependence. The transition between the two stages typically occurs at 2 micron.

For the pre-transition period, the corrosion rate is given by an Arrhenius equation [101]:

$$\frac{dS^3}{dt} = C_1 \exp\left(\frac{-Q_1}{RT_I}\right), \text{ for } S \leq S_{trans}. \tag{15.2}$$

For the post-transition period, the corrosion rate is given by [101]:

$$\frac{dS}{dt} = C_2 \exp\left(\frac{-Q_2}{RT_I}\right), \text{ for } S > S_{trans} \tag{15.3}$$

where
S is the oxide thickness
T_I is the metal-oxide interface temperature
C_1 is the rate constant for pre-transition oxidation
Q_1 is the activation energy for pre-transition oxidation
C_2 is the rate constant for post-transition oxidation
Q_2 is the activation energy for post-transition oxidation
R is the universal gas constant
S_{trans} is the transition oxide thickness

The metal-oxide interface temperature, T_I, is calculated assuming steady-state heat conduction across the oxide thickness as:

$$T_I = T_{co} + \frac{q''S}{k_{ox}} \tag{15.4}$$

where T_{co} is the outer surface (waterside) oxide temperature and k_{ox} is thermal conductivity of zirconium oxide.

In most BISON simulations, the oxide layer is not meshed independently. Instead, the oxide layer is modeled as a virtual layer within the clad, and the code keeps track of the thickness S, as shown in Figure 15.1. Since the oxide causes a larger temperature jump than would be caused by the same thickness of metal, T_{co} calculated by BISON does not correspond to the true temperature at the coolant-clad interface. Therefore, we must modify the heat transfer coefficient so that the driving force $h(T_{co} - T_b)$ (T_b is the bulk coolant temperature) is correct.

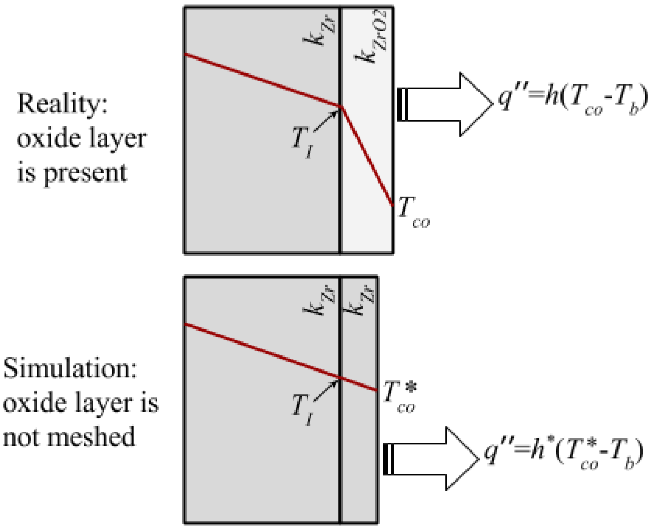

Figure 15.1: Diagram showing how BISON accounts for the temperature jump across the oxide without explicitly meshing the oxide layer. The red lines indicate temperature profiles.

In this approach, zircaloy material is used in the thermal solution while an effective heat transfer coefficient is used to compute a “fictitious” boundary condition to match the true temperature at the metal and oxide interface. We begin with two equivalent statements for heat flux into the coolant

$$q'' = h(T_{co} - T_b) \tag{15.5}$$

$$q'' = h^*(T^*_{co} - T_b) \tag{15.6}$$

where h is the true heat transfer coefficient. The starred values T^*_{co} and h^* are the simulated (fictitious) temperature of the oxide surface (waterside) and corresponding effective heat transfer coefficient, respectively. The temperature at the interface between the oxide and metal must also match:

$$T_I = T_{co} + \frac{q''}{k_{ZrO_2}} S \tag{15.7}$$

$$T_I = T^*_{co} + \frac{q''}{k_{Zr}} \frac{S}{R_{PB}} \tag{15.8}$$

where
T_I is the temperature at the interface of the oxide and metal
k_{Zr} is the thermal conductivity of zirconium alloy
k_{ZrO_2} is the thermal conductivity of zirconium oxide
R_{PB} is the Pilling-Bedworth ratio
These equations can be combined to eliminate T_I and T^*_{co}

$$h^* = \frac{q''}{T_{co} - T_b + q''(\frac{S}{k_{ZrO_2}} - \frac{S}{k_{Zr}R_{PB}})} \tag{15.9}$$

$$= \frac{1}{\frac{1}{h} + S(\frac{1}{k_{ZrO_2}} - \frac{1}{k_{Zr}R_{PB}})} \tag{15.10}$$

$$= \frac{h}{1 + \frac{hS}{k_{Zr}R_{PB}}(\frac{k_{Zr}}{k_{ZrO_2}} - 1)} \tag{15.11}$$

The oxide growth calculation requires T_{co}, which can be calculated directly from T^*_{co} by

$$T_{co} = T^*_{co} + q''S\left(\frac{1}{k_{Zr}R_{PB}} - \frac{1}{k_{ZrO_2}}\right) \tag{15.12}$$

15.1.2 EPRI SLI Model

The EPRI/SLI model is implemented as the default corrosion model for PWR Zry-4 cladding material. This model uses enhancement factors on C_1 and C_2. For the pre-transition period, C_1 is multiplied by two factors, one related to the lithium concentration in the coolant and the other related to the iron concentration in the cladding. These are given as [102]

$$C_1 = C_{10} F_{Li}(1 + F_{Fe}) \tag{15.13}$$

$$F_{Li} = \exp\left(C_{Li}(0.12[Li] - 23[Li]/T)\right) \tag{15.14}$$

$$F_{Fe} = C_{Fe}[Fe] \tag{15.15}$$

where $[Li]$ = lithium concentration [ppm] in the coolant, and $[Fe]$ = fraction of iron particles dissolved (%) for a given initial particle size distribution. The parameters used in above equations are as follows:

$C_{10} = 5.876^{10}\mu\text{m}^3$/day
Q_1=33662.7 cal/mol
C_{Li}=0.65
C_{Fe}=0.02(%)$^{-1}$

The post-transition coefficient C_2, is multiplied by several enhancement coefficients as follows:

$$C_2 = C_{20}F_{Li}F_{Sn}F_{Q/A}(1 + F_H + F_{Fe} + F_\phi]C_{20} = 7.619 \times 10^6\mu\text{m/day} \tag{15.16}$$

The coolant chemistry (LiOH) enhancement factor is given by:

$$F_{Li} = \exp(C_{Li}(0.17[Li] - 20.4[Li]/T_I)) \tag{15.17}$$

The cladding tin content enhancement factor is given by:

$$F_{Sn} = \begin{cases} 1.25(\text{Sn} - 1.38) + 1.0 & \text{for Sn} \leq 1.38 \text{ wt\%} \\ 0.75(\text{Sn} - 1.38) + 1.0 & \text{for Sn} > 1.38 \text{ wt\%} \end{cases} \tag{15.18}$$

where Sn is tin content of cladding in (wt%). The heat flux normalization factor is given by:

$$F_{Q/A} = 1 + 0.0881(Q/A)/100 \tag{15.19}$$

where Q/A (W/cm^2) is the heat flux at cladding outer surface.

The hydrogen redistribution enhancement factor is:

$$F_H = \begin{cases} 0 & \text{for} \quad [H_2] < 400\,\text{ppm} \\ 0.699ln([H_2]/400) & \text{for} \quad 18811.25\,\text{ppm} \geq [H_2] \geq 400\,\text{ppm} \\ 2.691 & \text{for} \quad [H_2] > 18811.25\,\text{ppm} \end{cases} \tag{15.20}$$

where $[H_2]$ = cold side hydrogen content in the cladding metal-oxide interface.

The fast neutron flux enhancement factor is:

$$F_\phi = C_\phi \phi^{Po} \tag{15.21}$$

where ϕ = fast flux (E > 1 MeV, n/cm^2-s), C_ϕ = 1.2 $\times 10^{-4}$ (n/cm^2-s)$^{-0.24}$, and Po = 0.24.

The iron enhancement factor is defined by Eq. 15.15.

Activiation energy in the post-transition period is found to be dependent on hydrogen content [103]:

$$Q_2 = \begin{cases} Q_{2L} & \text{for} \quad [H_2] < 400\,\text{ppm} \\ (Q_{2U} - Q_{2L})F_H/F_{HU} + Q_{2L} & \text{for} \quad 18811.25\,\text{ppm} \geq [H_2] \geq 400\,\text{ppm} \\ Q_{2U} & \text{for} \quad [H_2] > 18811.25\,\text{ppm} \end{cases} \tag{15.22}$$

where F_{HU} = hydrogen enhancement factor at hydride rim ($[H_2]$ = 18811.25 ppm), Q_{2L} = 24825 cal/mol, and Q_{2U} = 9135.6 cal/mol.

15.1.3 Zirconium Oxide Thermal Conductivity

Thermal conductivity of zirconia in the model is a constant value of 1.5 W/m-K for PWR applications [102]. However the reported value of zirconium oxide thermal conductivity varies greatly from different sources.

In the NFIR experimental program, the ZrO_2 thermal conductivity was estimated using cladding elongation measurements during power ramps as a representation of cladding temperature changes [104]. By comparing the cladding elongation of a fuel rod with an external oxide to a reference rod without an external oxide, the thermal impact of the oxide layer was determined. Experiments were performed at oxide layer thicknesses between 30 and 82 μm. In determining the thermal conductivity from the measured data, considerations were made for external crud layers, power increases, power decreases, and oxide layer thickness. The results of the experiments found that the thermal conductivity of ZrO_2 is independent of oxide thickness and temperature in the temperature range between 240°C and 300°C. An NFIR corrosion model was developed with a constant thermal conductivity value of 2.7 W/m-K (which tends to be on the high side of the data). The NFIR model is based on a series of in-pile experiments performed in the Halden test reactor that were designed to determine the thermal conductivity of external oxide layers on fuel rods [104].

The MATPRO-11 Rev. 2 model for Zircaloy oxide thermal conductivity is based on several different data sources of thermal conductivity measurements [25]. These measurements were performed using a variety of oxide morphologies (stabilized oxides, nodular, and black) and oxide formation techniques (steam oxidation and plasma sputtering).

Using thermal diffusivity measurements, the thermal conductivity was determined for the different oxide types as a function of temperature. The MATPRO model used primarily data from tests with black oxide layers to develop the thermal conductivity as a function of temperature [25].

The resultant correlation is

$$k_{ox} = 0.835 + 1.81 \times 10^{-4} T \tag{15.23}$$

where k_{ox} is the oxide thermal conductivity (W/m-K) T is the oxide temperature (K).

The correlation above is applicable to solid Zircaloy oxide found on fuel rods. These other values are typical of other models found in the literature. Further information on the MATPRO Zircaloy oxide model can be found in Reference [25].

Nuclear Electric (NE PLC) use a different correlation starting at a value of 1.5 W/m-K. The value then decreases with oxide thickness according to the following relationship [102]:

$$k_{ox} = \begin{cases} 1.5, & 0\,\mu\text{m} < S \leq 48\,\mu\text{m} \\ 3.48 - 0.0412S, & 48\,\mu\text{m} < S \leq 65\,\mu\text{m} \\ 0.8, & S > 65\,\mu\text{m} \end{cases} \tag{15.24}$$

The CEA Cochise code uses a constant value of 1.6 W/m-K [102].

15.1.4 Numerical Method

Numerical solution of the oxide thickness growth consists of pre-transition and post-transition period.

In the pre-transition period:

$$\Delta S = \sqrt[3]{C_1 \exp\left(\frac{-Q_1}{RT_{co}}\right)\Delta t + S} \tag{15.25}$$

where

S is oxide thickness at previous time step (μm)
C_1 is rate constant for pre-transition oxidation (μm^3/day)
Q_1 is activation energy for pre-transition oxidation (cal/mol)
R is gas constant = 1.987 (cal/mol-K)
T_{co} is cladding outer surface temperature (K)
Δt is time increment (day)
ΔS is oxide thickness increment (μm)

In the post-transition oxidation period, an approximate integral method is used [105] to account for the metal-oxide interface temperature change on the oxygen weight gain:

$$\Delta S = \gamma \Delta W/100 \tag{15.26}$$

$$\Delta W = \frac{RT_{co}^2 k_{ox}}{\gamma Q_2 q''} \ln\left[1 - \frac{\gamma Q_2 q''}{RT_{co}^2 k_{ox}} k_0 \exp\left(-\frac{Q_2}{RT_{co}}\right)\exp\left(\frac{\gamma Q_2 q'' W}{RT_{co}^2 k_{ox}}\right)\right] \tag{15.27}$$

where

T_{co} is cladding outer surface temperature (K)
k_{ox} is thermal conductivity of zirconium oxide (W/cm-K)
ΔW is weight gain (g/cm ^{2})
γ (=0.6789 cm^3/g) is a factor that converts weight gain (g/cm^2) to thickness (cm)
Q_2 is activation energy for post-transition phase
q is heat flux (W/cm^2)
k_0 is rate constant for post-transition phase (g/cm^2-day)
Δt is time increment (day)
R is ideal gas constant = 1.987 (cal/mol-K)
W is weight gain at previous time step (g/cm^2)
S is oxide layer thickness at previous time step (μm)

15.2 Zirconium Alloy at High Temperature

In the high temperature range (e.g., accident situations) the coolant has become steam, and oxidation proceeds much more rapidly than at normal LWR operating temperatures. Under these conditions, the growth of the ZrO_2 scale can be described by a parabolic law:

$$\frac{dS^2}{dt} = A \exp\left(\frac{-Q}{RT_I}\right) \tag{15.28}$$

where

S is the oxide thickness

T_I is the metal-oxide interface temperature
A is the oxidation rate constant
Q is the activation energy
R is the universal gas constant

A model is available in BISON for Zircaloy-4 cladding outer corrosion up to high temperature, which is based on [106, 107, 108]. The model includes correlations for oxide scale growth rate appropriate to the different temperature ranges, following the recommendations in [108]. In particular, the following approach is adopted.

- For metal-oxide interface temperatures from 673 K up to 1800 K, the Cathcart-Pawel correlation [106] is used:
  $A = 2.252 \cdot 10^6\ \mu\text{m}^2/\text{s}$
  $Q/R = 18062$ K
- Above 1900 K, the Prater-Courtright correlation [107] is used:
  $A = 2.98116 \cdot 10^9\ \mu\text{m}^2/\text{s}$
  $Q/R = 28420$ K
- Between 1800 and 1900 K, the following correlation is used, which corresponds to a linear interpolation between the Cathcart-Pawel and Prater-Courtright correlations [108]:
  $A = 4.8253 \cdot 10^{20}\ \mu\text{m}^2/\text{s}$
  $Q/R = 77459$ K

Equation 15.28 is solved numerically by

$$S_i = \sqrt{A \exp\left(\frac{-Q}{RT_I}\right) \Delta t + S_{i-1}^2} \tag{15.29}$$

where
S_i is the oxide thickness at the current time step (μm)
S_{i-1} is the oxide thickness at the previous time step (μm)
Δt is the time increment (s)

For normal operating temperatures below 673 K, the EPRI/KWU/C-E model [105, 109] is used. The formulation is analogous to that described in Section 15.1.1 (Eqs. 15.2 and 15.3), with [105, 109]:

$C_1 = 6.3 \cdot 10^9\ \mu\text{m}^3/\text{day}$
$Q_1/R = 16266$ K
$C_2 = 8.04 \cdot 10^7 + 2.59 \cdot 10^8 \cdot \left(7.46 \cdot 10^{-15} \cdot \phi\right)^{0.25}\ \mu\text{m}^3/\text{day}$
$Q_2/R = 13775$ K

where ϕ is the fast neutron flux in n/cm^2-s.

15.3 Aluminum

According to [110, 111], corrosion of aluminum in ATR follows

$$t_{ox} = 0.7 \cdot 25.4 \cdot 443 \cdot \theta^{0.778} \exp(-4600/T) \qquad (15.30)$$

where

t_{ox} is the oxide thickness (μm)

θ is time (hours)

T is temperature (K)

This corrosion thickness may be used in the coolant channel model.

Bibliography

[1] R. L. Williamson, J. D. Hales, S. R. Novascone, M. R. Tonks, D. R. Gaston, C. J. Permann, D. Andrs, and R. C. Martineau. Multidimensional multiphysics simulation of nuclear fuel behavior. *J. Nucl. Mater.*, 423:149–163, 2012.

[2] J. D. Hales, R. L. Williamson, S. R. Novascone, D. M. Perez, B. W. Spencer, and G. Pastore. Multidimensional multiphysics simulation of TRISO particle fuel. *J. Nucl. Mater.*, 443:531–543, 2013.

[3] Pavel Medvedev. Fuel performance modeling results for representative FCRD irradiation experiments: Projected deformation in the annular AFC-3A U-10Zr fuel pins and comparison to alternative designs. Technical Report INL/EXT-12-27183 Revision 1, Idaho National Laboratory, 2012.

[4] D. Gaston, C. Newman, G. Hansen, and D. Lebrun-Grandié. MOOSE: A parallel computational framework for coupled systems of nonlinear equations. *Nucl. Eng. Design*, 239:1768–1778, 2009.

[5] C. Newman, G. Hansen, and D. Gaston. Three dimensional coupled simulation of thermomechanics, heat, and oxygen diffusion in UO_2 nuclear fuel rods. *J. Nucl. Mater.*, 392:6–15, 2009.

[6] M. M. Rashid. Incremental kinematics for finite element applications. *Internat. J. Numer. Methods Engrg.*, 36:3937–3956, 1993.

[7] Sam Key. Fma-3d theoretical manual. Technical Report Ver 32, FMA Development, LLC, Great Falls, Montanta, 2011.

[8] Fionn Dunne and Nik Petrinic. *Introduction to Computational Plasticity*. Oxford University Press, Oxford, 2005.

[9] Kanthal APMT Material Database. http://kanthal.com/en/products/material-datasheets/tube/kanthal-apmt/.

[10] L. Leibowitz and R.A. Blomquist. Thermal conductivity and thermal expansion of stainless steels D9 and HT9. *International Journal of Thermophysics*, 9(5):873–883, 1988.

[11] N. Yamanouchi, M. Tamura, H. Hayakawa, and T. Kondo. Accumulation of engineering data for practical use of reduced activation ferritic steel: 8%Cr-2%W-0.2%V-0.04%Ta-Fe. *J. Nucl. Mater.*, 191–194:822–826, 1992.

[12] S. Sharafat, R. Amodeo, and N.M. Ghoniem. Materials data base and design equations for the ucla solid breeder blanket. Technical Report UCLA-ENG-8611, PPG-937, UCLA, 1986.

[13] Compiled by: IFR Property Evaluation Working Group. Metallic fuels handbook. Argonne National Laboratory, June 1988.

[14] CINDA Recommended Data Based on CINDAS Evaluation from Available Information. https://cindasdata.com/Applications/TPMD/, June 2014.

[15] G. W. Lehmang. Thermal Properties of Refractory Materials. Technical report, Wright Air Development Division, 1960.

[16] Nicrofer 3033 - alloy 33, Material Data Sheet No. 4041. ThyssenKrupp VDM, 2000.

[17] D. Petti, P. Martin, M. Phelip, and R. Ballinger. Development of improved models and designs for coated-particle gas reactor fuels. Technical Report INL/EXT-05-02615, December 2004.

[18] J. J. Powers and B. D. Wirth. A review of TRISO fuel performance models. *J. Nucl. Mater.*, 405:74–82, 2010.

[19] C. A. Lewinsohn, M. L. Hamilton, G. E. Youngblood, R. H. Jones, F. A. Garner, S. L. Hecht, and A. Kohyama. Irradiation-enhanced creep in SiC: data summary and planned experiments. *J. Nucl. Mater.*, 253:36–46, 1998.

[20] Kenneth C. Mills. *Recommended Values of Thermophysical Properties for Selected Commercial Alloys*. Woodhead Publishing, 2002.

[21] J. K. Fink. Thermophysical properties of uranium dioxide. *J. Nucl Materials*, 279(1):1–18, 2000.

[22] P. G. Lucuta, H. J. Matzke, and I. J. Hastings. A pragmatic approach to modelling thermal conductivity of irradiated UO_2 fuel: review and recommendations. *J. Nucl. Mater.*, 232:166–180, 1996.

[23] D. D. Lanning, C. E. Beyer, and K. J. Geelhood. Frapcon-3 updates, including mixed-oxide fuel properties. Technical Report NUREG/CR-6534, Vol. 4 PNNL-11513, 2005.

[24] A. Marion (NEI) letter dated June 13, 2006 to H. N. Berkow (USNRC/NRR). Safety Evaluation by the Office of Nuclear Reactor Regulation of Electric Power Research Institute (EPRI) Topical Report TR-1002865, Topical Report on Reactivity Initiated Accidents: Bases for RIA Fuel rod Failures and Core Coolability Criteria. http://pbadupws.nrc.gov/docs/ML0616/ML061650107.pdf, 2006.

[25] C. M. Allison, G. A. Berna, R. Chambers, E. W. Coryell, K. L. Davis, D. L. Hagrman, D. T. Hagrman, N. L. Hampton, J. K. Hohorst, R. E. Mason, M. L. McComas, K. A. McNeil, R. L. Miller, C. S. Olsen, G. A. Reymann, and L. J. Siefken.

SCDAP/RELAP5/MOD3.1 code manual, volume IV: MATPRO–A library of materials properties for light-water-reactor accident analysis. Technical Report NUREG/CR-6150, EGG-2720, Idaho National Engineering Laboratory, 1993.

[26] K. Ohira and N. Itagaki. Thermal conductivity measurements of high burnup UO_2 pellet and a benchmark calculation of fuel center temperature. In *Proceedings of the American Nuclear Society Meeting on Light Water Reactor Fuel Performance*, page 541, Portland, Oregon, Mar 2 to Mar 6, 1997.

[27] J. Carbajo, L. Gradyon, S. Popov, and V. Ivanov. A review of the thermophysical properties of mox and uo2 fuels. *J. Nucl. Mater.*, 299:181–198, 2001.

[28] C. Duriez, J.-P. Alessandri, T. Gervais, and Y. Philipponneau. Thermal conductivity of hypostoichiometriclow pu content mixed oxide. *J. Nucl. Mater.*, 277:143–158, 2000.

[29] C. Ronchi, M. Sheindlin, M. Musella, and G.J. Hyland. Thermal conductivity of uranium dioxide up to 2900 k from simultaneous measurement of the heat capacity and thermal diffusivity. *Journal of Applied Physics*, 85:776–789, 1999.

[30] M. Amaya, J. Nakamura, F. Nagase, and T. Fuketa. Thermal conductivity evaluation of high burnup mixed-oxide (mox) fuel pellet. *J. Nucl. Mater.*, 414:303–308, 2011.

[31] Y. Rashid, R. Dunham, and R. Montgomery. Fuel analysis and licensing code: FALCON MOD01. Technical Report EPRI 1011308, Electric Power Research Institute, December 2004.

[32] Eds. M. A. Kramman, H. R. Freeburn. Escore–the epri steady-state core reload evaluator code: General description. Technical Report EPRI NP-5100, Electric Power Research Institute, February 1987.

[33] K. Lassmann and H. Blank. Modelling of fuel rod behavior and recent advances of the TRANSURANUS code. *Nucl. Engrg. Design*, 106:291–313, 1988.

[34] A. T. Mai, W. F. Lyon, R. O. Montgomery, and R. S. Dunham. An evaluation of the MATPRO fuel creep model using the FALCON fuel analysis code. *Trans. Am. Nucl. Soc.*, 102:888–889, 2010.

[35] Y. R. Rashid, H. T. Tang, and E. B. Johansson. Mathematical treatment of hot pressing of reactor fuel. *Nucl. Engrg. Design*, 29:1–6, 1974.

[36] Y. Guerin. Mechanical-behaviour of nuclear fuel under irradiation. *Annales de chimie - science des materiaux*, 10:405–414, 1985.

[37] C. Milet and C. Piconi. Fluage en pile de l'oxyde mixte uo2-puo2. *J. Nucl. Mater.*, 116:196–199, 1983.

[38] J.B. Ainscough, B.W. Oldfield, and J.O. Ware. Isothermal grain growth kinetics in sintered UO_2 pellets. *J. Nucl. Mater.*, 49:117–128, 1973.

[39] M.I. Mendelson. Average grain size in polycrystalline ceramics. *Journal of the American Ceramic Society*, 52:443–446, 1969.

[40] Yeon Soo Kim and G. L. Hofman. AAA Fuels Handbook. Technical report.

[41] D. E. Burkes, C. A. Papesch, A. P. Maddison, T. Hartmann, and F. J. Rice. Thermophysical properties of DU-10 wt.*Journal of Nuclear Materials*, 403:160 – 166, 2010.

[42] H. Shimizu. The properties and irradiation behavior of U_3Si_2. Technical Report NAA-SR-10621, Atomics International, 1965.

[43] J. T. White and A. T. Nelson. Report on performance of advanced ceramic lwr fuel candidates. Technical Report LA-UR 13-23673, Los Alamos National Laboratory, 2013.

[44] J. E. Matos and J. L. Snelgrove. Research reactor core conversion guidebook-Vol 4: Fuels (Appendices I-K). Technical Report IAEA-TECDOC-643, 1992.

[45] J.L Snelgrove M. R. Finlay, G. L. Hofman. Irradiation behaviour of uranium silicide compounds. *Journal of Nuclear Materials*, 325:118–128, 2004.

[46] N. E. Hoppe. Engineering model for zircaloy creep and growth. In *Proceedings of the ANS-ENS International Topical Meeting on LWR Fuel Performance*, pages 157–172, Avignon, France, April 21-24, 1991.

[47] T. A. Hayes and M. Kassner. Creep of zirconium and zirconium alloys. *Metallurgical and Materials Transactions A*, 37A:2389–2396, 2006.

[48] J.H. Moon, P.E. Cantonwine, K.R. Anderson, S. Karthikeyan, and M.J. Mills. Characterization and modeling of creep mechanisms in zircaloy-4. *J. Nucl. Mater.*, 353(3):177 – 189, 2006.

[49] M. Limbäck and T. Andersson. A model for analysis of the effect of final annealing on the in- and out-of-reactor creep behavior of zircaloy cladding. In *Zirconium in the Nuclear Industry: Eleventh International Symposium*, ASTM STP 1295, pages 448–468, 1996.

[50] Y. Matsuo. Thermal creep of zircaloy-4 cladding under internal pressure. *Journal of Nuclear Science and Technology*, 24(2):111–119, February 1987.

[51] P. Van Uffelen, C. Győri, A. Schubert, J. van de Laar, Z. Hózer, and G. Spykman. Extending the application range of a fuel performance code from normal operating to design basis accident conditions. *J. Nucl. Mater.*, 383:137–143, 2008.

[52] Y. R. Rashid, A. J. Zangari, and C. L. Lin. Modeling of PCI Under Steady State and Transient Operating Conditions. In *Proceedings of a technical committee meeting organized by the IAEA: Water Reactor Fuel Element Computer Modelling in Steady State, Transient, and Accident Conditions*, Preston, United Kingdom, September 18-22, 1988.

[53] A.R. Massih. Transformation kinetics of zirconium alloys under non-isothermal conditions. *J. Nucl. Mater.*, 384:330–335, 2009.

[54] A.R. Massih and L.O. Jernkvist. Transformation kinetics of alloys under non-isothermal conditions. *Modelling Simul. Mater. Sci. Eng.*, 17:055002 (15pp), 2009.

[55] A.R. Massih. Evaluation of loss-of-coolant accident simulation tests with the fuel rod analysis code FRAPTRAN-1.4. Technical Report TR11-008V1, Quantum Technologies AB, 2011.

[56] M. C. Billone, Y. Y. Liu, E. E. Gruber, T. H. Hughes, and J. M. Kramer. Status of Fuel Element Modeling Codes for Metallic Fuels. In *Proceedings American Nuclear Society Internaionl Conference on Reliable Fuels for Liquid Metal Reactors*, Tucson, Arizona, September 7–11 1968.

[57] G. K. Miller, D. A. Petti, J. T. Maki, and D. L. Knudsen. PARFUME theory and model basis report. Technical Report INL/EXT-08-14497, Idaho National Laboratory, 2009.

[58] G. Pastore, L. Luzzi, V. Di Marcello, and P. Van Uffelen. Physics-based modelling of fission gas swelling and release in UO_2 applied to integral fuel rod analysis. *Nuclear Engineering and Design*, 256:75–86, 2013.

[59] R.J. White and M.O. Tucker. A new fission-gas release model. *J. Nucl. Mater.*, 118:1–38, 1983.

[60] M.V. Speight. A calculation on the migration of fission gas in material exhibiting precipitation and re-solution of gas atoms under irradiation. *Nuclear Science and Engineering*, 37:180–185, 1969.

[61] Y.-H. Koo, B.-H. Lee, and D.-S. Sohn. COSMOS: a computer code to analyze LWR UO_2 and MOX fuel up to high burnup. *Annals of Nuclear Energy*, 26:47–67, 1999.

[62] S. Kashibe, K. Une, and K. Nogita. Formation and growth of intragranular fission gas bubbles in UO_2 fuels with burnup of 6-83 GWd/t. *J. Nucl. Mater.*, 206:22–34, 1969.

[63] T. Kogai. Modelling of fission gas release and gaseous swelling of light water reactor fuels. *J. Nucl. Mater.*, 244:131–140, 1997.

[64] A.R. Massih and K. Forsberg. Calculation of grain boundary gaseous swelling in UO_2. *J. Nucl. Mater.*, 377:406–408, 2008.

[65] J. Rest. The effect of irradiation-induced gas-atom re-solution on grain-boundary bubble growth. *J. Nucl. Mater.*, 321:305–312, 2003.

[66] R.J. White. The development of grain-face porosity in irradiated oxide fuel. *J. Nucl. Mater.*, 325:61–77, 2004.

[67] D.R. Olander and P. Van Uffelen. On the role of grain boundary diffusion in fission gas release. *J. Nucl. Mater.*, 288:137–147, 2001.

[68] M.S. Veshchunov. Modelling of grain face bubbles coalescence in irradiated UO_2 fuel. *J. Nucl. Mater.*, 374:44–53, 2008.

[69] M.V. Speight and W. Beere. Vacancy potential and void growth on grain boundaries. *Metal Science*, 9:190–191, 1975.

[70] E. Rothwell. The release of Kr^{85} from irradiated uranium dioxide on post-irradiation annealing. *Journal of Nuclear Materials*, 5:241–249, 1962.

[71] K. Une and S. Kashibe. Fission gas release during post irradiation annealing of BWR fuels. *Journal of Nuclear Science and Technology*, 27:1002–1016, 1990.

[72] E. Sartori, J. Killeen, and J. A. Turnbull. International Fuel Performance Experiments (IFPE) Database. OECD-NEA, 2010, available at http://www.oecd-nea.org/science/fuel/ifpelst.html.

[73] G. Ducros, Y . Pontillon, and P.P. Malgouyres. Synthesis of the VERCORS experimental program: separate-effect experiments on fission product release, in support of the PHEBUS-FP programme. *Annals of Nuclear Energy*, 61:75–87, 2013.

[74] G. Pastore, D. Pizzocri, J. D. Hales, S. R. Novascone, D. M. Perez, B. W. Spencer, R.L. Williamson, P. Van Uffelen, and L. Luzzi. Modelling of transient fission gas behaviour in oxide fuel and application to the BISON code. In *Enlarged Halden Programme Group Meeting, Røros, Norway, September 7-12*, 2014.

[75] B.J. Lewis. Fission product release from nuclear fuel by recoil and knockout. *J. Nucl. Mater.*, 148:28–42, 1987.

[76] Y.-H. Koo, B.-H. Lee, and D.-S. Sohn. Analysis of fission gas release and gaseous swelling in UO_2 fuel under the effect of external restraint. *J. Nucl. Mater.*, 280:86–98, 2000.

[77] D. R. Olander. *Fundamental aspects of nuclear reactor fuel elements*. Technical Information Center, Energy Research and Development Administration, 1976.

[78] M. Oguma. Cracking and relocation behavior of nuclear fuel pellets during rise to power. *J. Nucl. Mater.*, 76:35–45, 1983.

[79] K. Forsberg and A. R. Massih. Diffusion theory of fission gas migration in irradiated nuclear fuel UO_2. *J. Nucl Materials*, 135(2-3):140–148, 1985.

[80] J. A. Turnbull, R. White, and C. Wise. The diffusion coefficient for fission gas atoms in UO_2. Technical Report IAEA-TC-659/3.5, 1987.

[81] Alicia Denis and Rosa Piotrkowski. Simulation of isothermal fission gas release. *J. Nucl. Mater.*, 229:149–154, 1996.

[82] H. Wallin. Forsberg-Massih fission gas model in BISON: Calibration using the Risø3 fuel test AN2. Technical Report Anatech, San Diego, CA, 2012.

[83] C. Vitanza, E. Kolstad, and U. Graziani. Fission gas release from UO_2 pellet fuel at high burnup. In *Proceedings of the American Nuclear Society Meeting on Light Water Reactor Fuel Performance*, page 361, Portland, Oregon, Apr 29 to May 3, 1979.

[84] Paul van Uffelen. Modelling isothermal fission gas release. In *Technical and economic limits to fuel burnup extension*, number IAEA-TECDOC-1299, pages 17–30. International Atomic Energy Agency, 2002.

[85] K. Lassmann, C. O'Carroll, J. van de Laar, and C. T. Walker. The radial distribution of plutonium in high burnup UO_2 fuels. *J. Nucl. Materials*, 208:223–231, 1994.

[86] American national standard for decay heat power in light water reactors. Technical Report ANSI/ANS-5.1-1979, American Nuclear Society, 1979.

[87] A. M. Ross and R. L. Stoute. Heat transfer coefficient between UO_2 and Zircaloy-2. Technical Report AECL-1552, Atomic Energy of Canada Limited, 1962.

[88] D. D. Lanning and C. R. Hann. Review of methods applicable to the calculation of gap conductance in zircaloy-clad uo2 fuel rods. Technical Report BWNL-1894, UC-78B, 1975.

[89] K.-T. Kim. UO_2/Zry-4 chemical interaction layers for intact and leak PWR fuel rods. *Journal of Nuclear Materials*, 404:128–137, 2010.

[90] M. Heinstein and T. Laursen. An algorithm for the matrix-free solution of quasistatic frictional contact problems. *Int. J. Numer. Meth. Engrg.*, 44:1205–1226, 1999.

[91] N. E. Todreas and M. S. Kazimi. *Nuclear systems I: thermal hyraulic fundamentals*. Hemisphere Publishing Corporation, New York, N.Y., USA, 1990.

[92] L. S. Tong and J. Weisman. *Thermal analysis of pressurized water reactors*. American Nuclear Society, La Grange Park, Illinois, USA, 1996.

[93] L. S. Tong and Y. S. Tang. *Boiling heat transfer and two-phase flow*. Taylor and Francis, Washington, DC, USA, 1997.

[94] R L Dougall and W M Rohsenow. Film-boiling heat transfer from a horizontal surface. *Journal of Heat Transfer*, 1961.

[95] M E Cunningham, C E Beyer, P G Medvedev, and G A Berna. Fraptran: A computer code for the transient analysis of oxide fuel rods. Technical Report NUREG/CR-6739 Vol.1, Pacific Northwest National Laboratory, 2001.

[96] F F Cadek et al. Pwr flecht final report supplement. Technical Report WCAP-7931, October 1972.

[97] IAPWS. Revised release on the IAPWS industrial formulation 1997 for the thermodynamic properties of water and steam. 2007.

[98] IAPWS. Revised release on the IAPWS formulation 1985 for the thermal conductivity of ordinary water substance. 2008.

[99] IAPWS. Release on the IAPWS formulation 2008 for the viscosity of ordinary water substance. 2008.

[100] IAPWS. IAPWS release on surface tension of ordinary water substance. 1994.

[101] I. G. Ritchie. Waterside corrosion of zirconium alloys in nuclear power plants. Technical Report IAEA TECDOC 996, 1998.

[102] P. M. Gilmore, H. H. Klepfer, and J. M. Sorensen. EPRI PWR fuel cladding corrosion (PFCC) model volume 1: Theory and users manual. Technical Report TR-105387-V1, December 1995.

[103] B. Cheng, P. M. Gilmore, and H. H. Klepfer. PWR zircaloy fuel cladding corrosion performance, mechanisms, and modeling. In *Zirconium in the Nuclear Industry: Eleventh International Symposium*, pages 137–160. ASTM STP 1295, American Society for Testing and Materials, 1996, 1996.

[104] J. Ikeda and E. Kolstad. In-pile determination of thermal conductivity of oxide layer on LWR cladding. Technical Report NFIR III RPX-103-04, February, 1996.

[105] F. Garzarolli, W. Jung, H. Shoenfeld, A. M. Garde, G. W. Parray, and P.G. Smerd. Review of PWR fuel rod waterside corrosion behavior. Technical Report EPRI NP-2789 Project 1250 Final Report, 1982.

[106] J. V. Cathcart, R. E. Pawel, R. A. McKee, R. E. Druschel, G. J. Yurek, J. J. Campbell, and S. H. Jury. Zirconium metal-water oxidation kinetics, IV. reaction rate studies. Technical Report ORNL/NUREG-17, 1977.

[107] J. T. Prater and E. L. Courtright. Zircaloy-4 oxidation at 1300 to 2400 C. Technical Report NUREG/CR-4889, PNL-6166, 1987.

[108] G. Schanz. Recommendations and supporting information on the choice of zirconium oxidation models in severe accident codes. Technical Report FZKA 6827, SAM-COLOSS-P043, 2003.

[109] F. Garzarolli and M. Garzarolli. PWR Zr alloy cladding water side corrosion. Technical Report ANT International, 2012.

[110] J. C. Griess, H. C. Savage, and J. L. English. Effect of heat flux on the corrosion of aluminum by water, part IV, tests relative to the advanced test reactor and correlation with previous results. Technical Report ORNL-3541, Oak Ridge National Laboratory, 1964.

[111] M. L. Griebenow, G. H. Hanson, M. J. Graber, Jr., and D. S. Field. ATR startup fuel-plate cladding corrosion test: Preliminary data and conclusions. In *American Nuclear Society 1971 Winter Meeting Transactions*, volume 14(3), pages 761–762, 1971.